Natural Resources Canada | Ressources naturelles Canada

GEOLOGICAL SURVEY OF CANADA
OPEN FILE 8769

Electrical resistivity surveys, Vars-Winchester esker aquifer, Ontario

G.A. Oldenborger

2021

Canada

GEOLOGICAL SURVEY OF CANADA
OPEN FILE 8769

Electrical resistivity surveys, Vars-Winchester esker aquifer, Ontario

G.A. Oldenborger

2021

Permanent link: https://doi.org/10.4095/328037

This publication is available for free download through GEOSCAN (https://geoscan.nrcan.gc.ca/).

Recommended citation
Oldenborger, G.A., 2021. Electrical resistivity surveys, Vars-Winchester esker aquifer, Ontario; Geological Survey of Canada, Open File 8769, 69 p. https://doi.org/10.4095/328037

Publications in this series have not been edited; they are released as submitted by the author.

SUMMARY

This Open File reports on results of electrical resistivity surveys performed over the Vars-Winchester esker aquifer near Embrun, Ontario as part of the Natural Resources Canada Groundwater Geoscience Program. Electrical resistivity and induced polarization data were acquired within boreholes as 1D logs, along the surface as 2D profiles, and from surface-to-borehole in 3D. The data were processed and inverted to recover 1D, 2D and 3D models of electrical resistivity and chargeability. The resulting models clearly indicate a resistive esker feature thickest at the centre and thinning on the flanks. The 2D profiles show a more resistive esker centre consistent with a gravel core under sand cover that is supported by the 1D and 3D models. The base of the esker is not clearly resolved in the resistivity models due to the weak contrast of the esker/basement contact that is below the depth of investigation of the surface surveys, and subject to high uncertainty in the surface-to-borehole surveys. The resistivity models reveal significant and coherent electrical layering within the conductive Champlain Sea sediments surrounding the esker. Electrical resistivity is observed to decrease with depth below the water table in the marine muds. Above the water table, the unsaturated zone exhibits anomalously low resistivity that may result from accumulation of salt and other potential electrolytes in road- and crop-side ditches. Chargeability is measurable at the site for the given experiments. Vertical structure of apparent chargeability is evident in the 1D borehole logs. The gravels and sands appear most chargeable, but the normalized chargeability suggests dominantly electrolytic conduction with largely uniform surface conduction. No meaningful chargeability models can be recovered for the 2D or 3D surveys, presumably due to the small values of chargeability and high noise levels.

TABLE OF CONTENTS

INTRODUCTION

In glaciated terrain such as Canada, buried eskers may host aquifers that are significant groundwater resources where low-yield bedrock, mud, and diamicton otherwise dominate the hydrogeological setting. Often, these eskers or aquifers will have limited surface expression, and may have complex internal structure that can complicate mapping and resource management. Methods of investigation using water wells and cored boreholes may not capture regional aquifer properties or geometry (e.g., Shaver and Pusc, 1992; Jørgensen and Sandersen, 2009). Geophysical methods can provide additional minimally-invasive and spatially extensive measurements of aquifer characteristics that can be used to extrapolate information away from boreholes.

In particular, electrical resistivity experiments can be applied to interrogate both aquifer structure and aquifer properties due to the dependence of electrical properties on sediment type, texture, porosity, and pore water (Slater, 2007). Electrical resistivity models of the subsurface can be used for qualitative interpretation of aquifer morphology or internal structure, and have been used to map Quaternary aquifer systems (Steuer et al., 2009; Siemon et al., 2009; Oldenborger et al., 2013). Given additional data, electrical properties can be used as part of a more quantitative hydrogeophysical estimation of aquifer properties (Foged et al., 2013; Hoyer et al., 2015; Weller et al., 2015; Maurya et al., 2018).

For this study, electrical resistivity and induced polarization data were collected for a portion of the Vars-Winchester esker aquifer system near Embrun, Ontario as part of the Natural Resources Canada Groundwater Geoscience Program. The experiments were conducted as part of a larger initiative for hydrogeological and geophysical investigation of the aquifer and aquiclude. Surveys were conducted within boreholes as 1D profiles, along the surface as 2D profiles, and from surface-to-borehole in 3D. The data were processed and inverted to recover 1D, 2D and 3D models of electrical resistivity that are used to characterize the aquifer/aquiclude system in terms of electrical properties.

STUDY AREA

The electrical resistivity experiments described in this report were conducted over an approximately 2 km × 4 km area of South Nation River watershed near Embrun, Ontario (Figure 1). The study area represents a small portion of the Vars-Winchester esker aquifer system that has been selected for hydrogeophysical studies by the Geological Survey of Canada (Paradis et al., 2020). The communities of Vars and Limoges both exploit the Vars-Winchester esker aquifer for municipal drinking water, along with many domestic and agricultural users. The aquifer system consists of an esker approximately 40 km in length with a carbonate gravel core

(coarse sand matrix) covered by sand extending a few hundred meters in width (Cummings and Russel, 2007; Pugin et al., 2009; Sauriol, 2016). The esker is covered along most of its length by fine marine muds deposited during inundation by the post-glacial Champlain Sea. The esker erosively overlies a thin till sheet (not everywhere present) and Paleozoic carbonate shale bedrock with a fractured upper surface (Cummings et al., 2011).

The Champlain Sea sediments have high salinity (Torrance, 1983; Crow et al., 2017) and are expected to be highly conductive, despite low connected porosity of the muds. A large component of the conductivity may result from surface conduction (Hyde and Hunter, 1998) that may be manifest as an induced polarization response. In contrast, the esker sands and gravels are relatively fresh and are expected to be electrically resistive, despite a higher connected porosity. Geophysical logs for the study area are presented by Crow et al. (2020) that generally confirm these assumptions while providing evidence of additional internal complexity for the sedimentary units.

METHODS

Low-frequency or direct-current (DC) electrical resistivity surveys are a well-established geophysical method that involves galvanic injection of a known electrical current into the subsurface, and measurement of the resulting potential distribution via surface and/or borehole electrodes (Daily et al., 2005). Measurements typically consist of the transfer resistance, which is the voltage to current ratio $R = V/I$, and some measure of the polarization of the ground such as the time-domain chargeability M, or a frequency-domain equivalent. Using modern multi-electrode and multi-channel instruments, measurements from many current and potential electrode combinations are used to construct a model of the subsurface electrical properties that satisfies the observed measurements. Typically, this is achieved via some form of iterative optimization or inversion (e.g., LaBrecque et al., 1996; Li and Oldenburg, 2000; Loke et al., 2014).

Electrical resistivity and induced polarization data were collected in October 2018 within boreholes as 1D logs, as 2D profiles along the surface, and from surface-to-borehole in 3D (Figure 1). The borehole-only data were collected from below the water table to depths of 36–38 m in four fully-screened boreholes, three of which represent a cross section perpendicular to the esker (Crow et al., 2020; Paradis et al., 2020). The 2D surface data were collected along roadsides both cross- and along-strike to the esker as guided by seismic reflection data (Pugin et al., 2009; Pugin et al., 2020). The 3D surface-to-borehole data were collected using a combination of borehole electrodes below the water table and electrodes extending in two directions away from the borehole at surface. An additional high resolution 2D profile was

collected in October 2019 across a northern tributary of the Castor River along Route 300 (Figure 1) to better understand esker recharge dynamics.

All data were collected using a 64-electrode DAS-1 resistivity meter (Multi-Phase Technologies) with 30 cm stainless steel spike electrodes at surface, and 10 cm stainless steel cylindrical electrodes down hole. Data were collected in the time-domain using a 0.25 Hz 50% duty cycle square wave with a 20 ms delay after voltage switch off followed by 16 logarithmic-spaced windows over 917 ms. Data were stacked over 3.5 waveforms. Measurements were performed using four multi-core cables with 16 electrodes each, but current injection and potential measurements were not limited to separate cables.

Surface data were collected with 64 electrodes using a multi-gradient array with dipole lengths of $a = 1, 2, 3, 4, 5$ and separation integers of $s = 16, 16, 8, 8, 8$. Electrode spacing was 5 m, except for the stream crossing profile that used an electrode spacing of 2 m. To increase along-line data density, the current dipole was circulated to use every electrode for current injection regardless of dipole length (as opposed to using only those electrodes defined by a particular dipole length). To provide enhanced horizontal resolution in the near surface, the multi-gradient array was augmented with a circulated dipole-dipole array limited to a single dipole length of $a = 1$ and dipole separations of $n = 1$–6. The combined surface measurement sequence consists of 2111 measurements: 1760 multi-gradient and 351 dipole-dipole.

Borehole data were collected with 32 electrodes at 1 m spacing below the water table using a circulated dipole-dipole array with dipole lengths of $a = 1$–4 and separations of $n = 1$–6. Circulation ensures that downhole measurement spacing is equal to the electrode spacing, regardless of dipole length. The borehole-only measurement sequence consists of 438 measurements. For borehole-to-surface surveys, the borehole-only sequence was augmented with both 64-electrode multi-gradient and dipole-dipole arrays equivalent to those used on the surface, where the first 32 electrodes were below the water table at 1 m spacing, and the last 32 electrodes were arranged on the surface extending away from the borehole at 1 m spacing. The borehole-to-surface surveys were repeated for two directions away from the borehole, either opposite or perpendicular. The combined surface-to-borehole measurement sequence consists of 4660 measurements, although there are some repeated measurements within the borehole.

Data Processing

Processing of electrical resistivity data is performed to remove noisy and spurious measurements that may impede reconstruction of a suitable electrical property model, or result in features of the model that are not geologically meaningful (inversion artifacts). Low current and low measured voltage, along with poor repeatability of voltage after stacking are the most obvious indicators of

low signal-to-noise ratios. However, resistivity data are often highly repeatable and spurious data can also result from, or be associated with high electrode-to-ground contact resistance, high naturally occurring spontaneous potential, and high chargeability, that may not be manifest as low voltage, or high stacking error (Zonge and Hughes, 1985; LaBrecque and Daily, 2008; Oldenborger and LeBlanc, 2018). As such, data processing must account for multiple sources or error, and may be iterative.

Data processing was similar for surface, borehole, and surface-to-borehole data and followed a multi-step procedure described in general by Oldenborger and LeBlanc (2018) and detailed in Appendix A. Problem electrodes or quadrupoles associated with survey logistics and execution were identified from the field notes and any associated data were removed. The remaining data were first filtered for injected current and measured voltage ($|I| \geq 0.05$ mA and $|V| \geq 0.5$ mV) with filter values chosen based on experience and the data. The transfer resistance was computed as $R = V/I$ and then filtered for repeatability over the stacked waveforms ($\Delta R \leq 3\%$) with the filter value chosen based on the data and the desired level of accuracy in the final model.

Time-domain chargeability M was calculated from the measured voltage decays using the time-normalized integral formulation and all 16 data windows (Appendix A). Chargeability may be normalized by resistivity (scaled by conductivity) to yield the normalized chargeability M_n, which is proportional to the quadrature conductivity and may be more indicative of surface conduction (Lesmes and Frye, 2001; Slater and Lesmes, 2002; Revil et al., 2017). Voltage decays and chargeability are not as repeatable as resistance measurements. The chargeability data (but not the associated resistance data) were filtered for $\Delta M \leq 30\%$ where the threshold was chosen to retain most of the continuous error distribution (e.g., Slater and Glaser, 2003).

Systematic noise resulting from high contact resistance R_c and spontaneous potential V_{SP} may not be captured by the preceding filter conditions. High contact resistance typically occurred for a small number of measurements associated with gravel pullouts along the roadside, for which establishing electrical contact was difficult. Filtering for $R_c \leq 5000\ \Omega$ effectively removes these data, where the filter value was chosen based on the data and noise associated with a simple circuit analog (LaBrecque and Daily, 2008). The acquisition sequences were ordered to avoid battery effects (when a recently energized electrode is used for potential measurement) and the DAS-1 employs low-frequency noise compensation, such that measurements are relatively insensitive to spontaneous potential. Nevertheless, experimental field tests showed correlation between s_V and V_{SP}. Accordingly, the data were filtered for $V_{SP} \leq 500$ mV where the filter value was chosen based on measurements with observed battery effects from non-ordered sequences.

Correlation has also been demonstrated between increased measurement error and chargeability (LaBrecque and Daily, 2008; Oldenborger and LeBlanc, 2018). Since reasonable chargeabilities

in environmental settings are likely small (Slater and Lesmes, 2002), but need not be positive (Nabighian and Elliot, 1976; Dahlin and Loke, 2015), the data (resistance and chargeability) were filtered for $|M| \leq 100$ mV/V. Surface-to-borehole data require additional filtering due to large geometric factors κ and unconventional quadrupole geometries with unstable sensitivity. Accordingly, surface-to-borehole data were further filtered for $|\kappa| \leq 8000$ m and $|V| \geq 3$ mV.

Resistivity data retention after filtering for I, V, ΔR, R_c, V_{SP}, M, and κ is approximately 98% for surface data and 99% for surface-to-borehole data. Chargeability data retention is approximately 84% for surface data and 96% for surface-to-borehole data. Summaries of the data and processing flow for the Rt. 300 surface acquisition and the BH1 surface-to-borehole acquisition (Figure 1) are given in Appendices B and C, respectively. The order of the filters is not important. Removal of a single filter condition is often compensated for by a subsequent filter (low voltage may be accompanied by high chargeability, for example) but the filters are most effective in combination (Oldenborger and LeBlanc, 2018). Data rejection for both resistivity and chargeability was mostly localized to line positions with sources of cultural noise such as pullouts, culverts, and buried infrastructure.

Data Inversion

Surface resistivity and induced polarization data were inverted using the 2D least-squares regularized inversion of Loke et al. (2014). Resistance data were weighted by the individual measurement errors ΔR and chargeability data were weighted by the individual measurement errors ΔM. Logarithmic transformation was applied to the resistance data. Least-squares norms were used on both the data and the model with 2:1 horizontal-to-vertical smoothness given that some degree of layering can be expected. No bounds were placed on the recovered model values. The model cell sizes were set at 2.5 m horizontal by 1.25 m vertical at surface, with a 1.06 times layer-to-layer increase for a cell thickness of approximately 3 m at 30 m depth (total number of cells depends on profile length). The regularization parameter was cooled from 0.20 to 0.04 and convergence was determined using a target RMS misfit of 3%. The target RMS misfit is equivalent to the maximum filtered measurement error (not the mean) and reflects the fact the true data noise (and thus the expected misfit) is likely higher than that estimated during data processing. Target misfit was typically achieved after 2–3 iterations. The diagonals of the resolution matrix normalized by both cell area and maximum resolution are used to define an approximate region of reliability as $\mathbf{R}_{ii} > 0.003$ for the recovered models (e.g., Oldenborger and LeBlanc, 2015).

No reference model was employed for surface surveys, but bedrock was prescribed as a ‘fixed’ region across the entire bottom of the model at depths based on borehole lithological records (Paradis et al., 2020). However, the lithological logs can have as much as 2 m error (the length of

the drill rod) and the true resistivity of the bedrock is not well known. As such, the damping factor for the fixed regions was set to 1.5 times that of the regular smoothness constraint for the remaining parts of the model, which gives the inversion routine significant influence over the recovered resistivity. Bedrock resistivity was set at 50 Ωm (20 mS/m) based on the borehole apparent resistivity logs (Appendix C), which yields nearly equivalent data misfit as a completely free model.

Borehole-only data were isolated as apparent resistivity and apparent chargeability logs. These data were not inverted, but were converted to apparent resistivity using a wholespace geometric factor with image sources to account for the earth surface (Figures C16 and C17). Borehole-only data can be inverted using axial or vertical 2D assumptions, but quantitative use of the results will be limited (LaBrecque et al., 2006; Maurer et al., 2009). Instead, the borehole data were inverted as part of the surface-to-borehole data sets. These combined data could be inverted using a cross-borehole-type 2D algorithm. However, tests using such an algorithm showed poor models and strong oscillatory artifacts associated with the borehole, which is a truly 3D feature. Accordingly, the surface-to-borehole data were inverted using the 3D least-squares regularized inversion of Li and Oldenburg (2000). Again, resistance and chargeability data were weighted by the individual measurement errors ΔR and ΔM. Regularization length scales were set at 10 m in the lateral directions and 2 m in the vertical direction. Stronger horizontal-to-vertical regularization was required for the 3D data to suppress vertical borehole artifacts. Furthermore, initial tests confirmed the importance of the borehole in that convergence of the 3D inversions required explicit meshing of the fluid—filled borehole in 3D (using a network of small-scale model cells to represent the borehole).

The 2017 South Nation boreholes were drilled with a 14.2 cm diameter bore and cased with 11.5 cm outer diameter slotted PVC (Paradis et al., 2020). In the model mesh, the boreholes are represented in horizontal cross section by 4 square cells with dimensions of 10 cm × 10 cm such that the effective borehole diameter is approximately 20 cm. This slightly enlarged borehole can compensate for void space around the casing (Crow et al., 2020) that will otherwise bias near-hole inversion results. Away from the borehole, the inversion cell sizes were increased by 1.5 times until reaching 1 m, the surface electrode spacing. Vertical cell size is constant at 1 m, the borehole electrode spacing. This results in a cell size ratio of 10:1 within the borehole. Trials with a vertical cell size of 0.5 m exhibit similar convergence behaviour, but with increased vertical oscillation in the recovered model, indicating that the 10:1 ratio does not hamper the numerical solution, but instead helps dampen the inversion near the borehole electrodes which are known points of instability. The models are comprised of greater than 130,000 cells (depending on borehole depth). The regularization parameter and convergence were determined using the discrepancy principle (that data misfit should match data noise) and the observed

measurement errors for resistivity data, and generalized cross-validation for the chargeability data.

Trials with a default reference model of the best-fitting halfspace exhibit significant model variation in the radial direction and some borehole effects not entirely ameliorated by meshing of the hole alone. This noise could be partially suppressed with stronger damping. However, a modified reference model provides a solution that better represents the strong contrasts inherent to the borehole. The 3D inversions utilize a reference model with a conductive borehole and a resistive background. Borehole resistivity was set equal to the measured borehole water resistivity of 7 Ωm (0.14 S/m) below the water table, although the water resistivity may vary downhole (Crow et al., 2020). Above the water table, borehole resistivity was set equal to 10^8 Ωm for air. Outside of the borehole, the reference resistivity was set using the independent apparent resistivity log for each borehole obtained from the borehole-only data and the apparent resistivity transform (Figure C17). Although the apparent resistivity transform is only correct for homogeneous ground, it is well-suited for single near-hole measurements.

RESULTS

Borehole Logs

The 1D apparent resistivity and apparent chargeability logs for the 1D borehole surveys are shown in Figures 2–5. The illustrated logs result from geometric transform (not inversion) of borehole-only dipole-dipole data with a 3 m quadrupole length ($a = 1$, $n = 1$) and an approximately 40 cm radius of median signal strength (e.g., Edwards, 1977). Apparent resistivity variations match well with lithological contacts. The Champlain sea sediments consistently exhibit resistivities below 20 Ωm. The sands and gravels are more variable both along the Rt. 300 profile, and at BH4 on St. Pierre to the north. The sands exhibit resistivities of approximately 40–60 Ωm along Rt. 300 and up to 180 Ωm at BH4, whereas the gravels exhibit resistivities of approximately 80–180 Ωm. Some degree of vertical heterogeneity of electrical resistivity exists in all of the sedimentary units. Only a few of the log measurements extend into bedrock, but these data suggest a resistivity for the shale of 40–60 Ωm.

Borehole apparent chargeability is measurable and appears to be influenced somewhat by lithology with higher chargeability in the sand and gravel (up to 6 mV/V). However, some of this variation in chargeability is influenced by the resistivity itself. The normalized chargeability, which is independent from resistivity, is more uniform and lithological control is not as strong. Some variability of normalized chargeability with depth (such as for BH4) suggests a change in polarization properties, but the magnitude of normalized chargeability is generally smaller than encountered for field measurements in similar glacial deposits (McLachlan et al., 2020). Small

values of normalized chargeability indicate that electrolytic conduction is largely dominant over surface conduction. BH3, logged as exclusively clay silt, exhibits the highest normalized chargeability which suggests there may be some correspondence between normalized chargeability and clay content for the aquiclude (e.g., Slater and Lesmes, 2002). BH4 exhibits an increase in normalized chargeability at depth, consistent with increase clay content in a basal diamicton that is not logged in the other boreholes.

Surface Surveys

The recovered 2D electrical resistivity models for the surface profiles are shown in Figures 6–9. The esker is visible as an electrically resistive anomaly on all of the deep profiles with a resistivity of approximately 40–200 Ωm. On Rt. 300, the survey crosses the esker nearly along strike and the esker shape is apparent as thickest at the centre and thinning towards the flanks (Figure 6). However, neither the silt-sand nor sand-gravel contacts in BH1 and BH2 lie on the same resistivity isosurface, illustrating the ambiguity and uncertainty in resistivity models, and the loss of resolution at depth for surface surveys. On Rt. 200, only the eastern edge of the esker is covered by the survey (Figure 7). No on-profile borehole information is available, but the resistivity layering is consistent with nearby BH4. On St. Pierre, the survey crosses the esker oblique to strike and the esker is present in most of the profile (Figure 8). Observed esker resistivities on the St. Pierre profile are higher than those encountered for the other profiles, and this observation is consistent with the log from BH4 (Figure 5).

There is cultural noise on all profiles. On Rt. 300, the dominant noise sources are underground utilities at approximate line positions of 170 m and 305 m, and a bridge embankment over a double culvert from line positions 465–475 m that result in localized inversion artifacts that do not greatly affect the fidelity of the model (Figure 6). In contrast, noise on St. Pierre from underground utilities at approximate line positions of 120 m and 265 m is so severe as to contaminate the recovered model for its entire depth. The presented model (Figure 8) results from the removal of all data with electrode locations within these noisy regions. The inversion cannot span the data gaps sufficiently, and they are manifest as the breaks in resistivity extending to depth that render the recovered resistivity model more uncertain than its counterparts.

The variable resistivity of the esker and the weak contrast with bedrock (50 Ωm) make it difficult to resolve the bottom of the esker, which is near the limit of the depth of investigation of the surveys. However, the esker is largely distinct from the conductive Champlain Sea marine muds that exhibit a recovered resistivity of approximately 5–60 Ωm. The 2D profiles accentuate a variable resistivity layering within the Champlain Sea sediments with an upper resistive unit (20–60 Ωm) and a lower conductive unit (5–20 Ωm) evident for Rt. 300 and Rt. 200.

Layering of the resistivity models in the very near surface agrees well with the measured water table depth of 4.1 m during acquisition. However, in all of the roadside profiles, the unsaturated zone appears as a relatively conductive layer, which is counter to that expected for reduced water content in similar material. In contrast, the off-road stream crossing profile (Figure 9) clearly exhibits the typical resistive unsaturated zone over a moderately conductive saturated zone (note the lesser modelled depth for the stream crossing profile due to smaller electrode spacing and shorter profile length). Roadside surveys were all conducted in roadside ditches adjacent to active farmland (except near the culvert crossing on Rt. 300), whereas the stream crossing profile was conducted away from the road and active farmland. It is hypothesized that the resistivity reversal observed for the roadside profiles results from an accumulation of road salt and other electrolytes (fertilizer) that concentrate in the unsaturated zone, but are diluted below the water table.

The stream crossing model also exhibits a conductive region directly below the stream (Figure 9), which is consistent with the measured stream water resistivity of 7 Ωm (0.14 S/m). If the stream were losing, or recharging the aquifer, it might be reasonable to expect the conductive anomaly to extend to depth. However, the opposite is observed. The conductive stream anomaly is thinnest below the stream, which is consistent with fresher water being sourced from below (a gaining stream). However, the anomalies are weak and the section is subject to significant uncertainty such that additional (seasonal) data are needed to support this hypothesis.

There is a small but measurable amount of apparent chargeability in the surface data (Figures A6, A11, and A13). However, recovered chargeability models are mostly homogeneous and below 2 mV/V (not shown) with any structure or larger values limited to locations of underground utilities and gravel pullouts (for which the data are correlated with high measurement error and contact resistance). There is some indication of 2–4 mV/V chargeability in the upper mud layer on Rt. 300 and Rt. 200, and there is some indication of approximately 10 mV/V chargeability of in the esker core.

However, normalized chargeabilities for these regions are small and equivalent ($M_n \approx 0.08$ mS/m) suggesting that there is no distinct change in polarization properties. The magnitude of normalized chargeability is similar to that of the borehole logs (Figures 2–5), but the logs exhibit some variability with depth, perhaps due to higher resolution. Further, although the measured and recovered values of M and M_n are subject to the choice of integration window, the surface surveys support the conclusion of dominantly electrolytic conduction. Surface conduction may still be present, but it is significantly smaller than the electrolytic conduction. Otherwise, the recovered 2D chargeability models are considered uninformative with regards to aquifer structure or properties.

Surface-to-Borehole Surveys

The recovered 3D electrical resistivity models for the surface-to-borehole surveys are shown in Figures 10–13. Again, variations in recovered model resistivity match well with lithological contacts. Consistent with the borehole logs, the esker sands and gravels are imaged as relatively homogeneous resistive layers of approximately 50–200 Ωm, often with a highly resistive layer above bedrock. This basal resistive layer is present in BH3 (Figure 12) where there is no corresponding observation in the borehole record, but muddy sand and diamicton layers above bedrock are interpreted from the downhole geophysical logs (Crow et al., 2020).

In contrast, the Champlain sea sediments are imaged as conductive regions with both horizontal and vertical structure. Apparent layering of the silts is most evident in BH2 and BH3 (Figures 11 and 12) with an upper resistivity of approximately 20–50 Ωm and a lower resistivity of approximately 8–20 Ωm in BH2 and 3–20 Ωm in BH3. Above the water table, the higher resolution 3D models also exhibit layering and heterogeneity in the vadose zone. For example, with the exception of BH3, the data require a resistive upper-most layer over a conductive layer that increases in resistivity at the water table, although this may also result from the borehole surveys being mostly out of the roadside ditches.

Due to the localized nature of the surface-to-borehole surveys, there is little information in the resistivity models regarding the large-scale continuous structure of the esker. Although the 3D models offer a higher-resolution picture than the surface models, the recovered models appear one-dimensional in nature. This results from a combination of resolution and the imposed log reference model. In some areas, the 3D inversion models depart significantly from the log reference model, suggestive of real heterogeneity. In particular, there is significant influence of the borehole in the recovered models. Explicit meshing of the borehole and its expression in the reference model should ameliorate much of the short-circuit effect of the fluid-filled boreholes. The smooth nature of the recovered model will necessarily extend the borehole effect, but the observed borehole effects (more prominent in the sands and gravels) may also indicate near-borehole void space that is generally manifest as a near-hole conductive annulus. In other areas, particularly where features are asymmetric at the borehole or symmetric at some distance from the borehole, inversion artifacts should be considered.

The average sensitivity and the volume of investigation (Oldenburg and Li, 1999) are illustrated in Figures 14 and 15 for BH1 and BH4. Although the sensitivity and volume of investigation (VOI) are both influenced by the final recovered model, they can be interpreted generally for surveys with the same experimental geometry to provide a limit on the region of model reliability as illustrated in Figures 10–13. Both the sensitivity and VOI indicate a loss of resolution away from the hole and the surface electrodes, such that there is a general region of

reliability somewhat like a 3D "T" shape that does not extend more than 10 m away from the electrodes. However, the VOI reveals additional near-electrode regions of uncertainty that occur despite high sensitivity, and result from strong non-uniqueness in the inversion (Oldenborger et al., 2007). For the surface-to-borehole experiments, non-uniqueness results in "shadow zones" over large parts of the model domain that can contribute to uncertainty and inversion artifacts. Shadow zones complicate interpretation of the resistivity models with the region of reliability and could possibly be suppressed by the acquisition of more (offline) data and/or a change in survey design.

As with the surface data, there is a small but measurable amount of apparent chargeability in the surface-to-borehole data (Figures B6, B12, and B15). However, despite lithological control evident in the 1D logs, the recovered 3D chargeability models are mostly homogeneous and below 0.2% (not shown). The secondary voltage data cannot be fit to better than 50% RMS error with spurious areas of recovered chargeability up to 10% attributed to noise.

DISCUSSION

Analyzing the results of electrical resistivity surveys allows for interpretation of the subsurface features in the existing geological context. The Vars-Winchester esker is evident as a resistive anomaly extending approximately 400–500 m in width, that can be traced over at least 4 km across the survey area. The esker is well discriminated from the conductive Champlain Sea sediments that surround it, and the contrast should allow for effect mapping of esker occurrence across the greater watershed. Bedrock is not reliably imaged by the surface surveys, and is only represented by a few borehole measurements in the surface-to-borehole surveys.

The electrical property models can be further used to characterize the individual components of the esker aquifer system. All of the resistivity models exhibit a more resistive esker centre consistent with a gravel core under sand cover. There is some uncertainty and overlap in the electrical resistivity attributed to the identified sedimentary units due to experimental noise and resolution loss associated with inversion. This is particularly true for the surface models that exhibit overlap in resistivity values between the upper muds and the outer regions of the esker. This may be real variability of electrical properties, but the higher-resolution borehole-based models show less variability of resistivity within sedimentary units, and better discrimination between them. Direct comparison between the 1D, 3D and 3D models is hampered by the fundamental differences in model resolution that arise from the different experimental geometries.

Also due to limitations in resolution associated with electrical surveys, it is difficult to distinguish whether observed variations in electrical properties are abrupt or transitional. The

observed decrease in resistivity with depth in the Champlain Sea sediments may arise from stratification of the muds, or a gradational change in texture or pore water salinity; the borehole logs and 3D models suggest the former. Similarly, electrical resistivity of the bedrock is not well-characterized and any interpretation about its hydrogeological properties (competent or fractured) is difficult.

Non-zero chargeability is measurable at the site for all of the surveys, but meaningful chargeability models could only be recovered for the 1D logs despite intensive data processing. It is hypothesized that small chargeability values and significant noise associated with larger dipole separation (not used for the logs) precluded fitting the data with any reasonable chargeability model. Limiting the data to $M > 0$ did not improve results. Chargeability data can be critical for understanding the role of surface conduction and predicting hydraulic properties. Better data could most likely be obtained by performing current injection and potential measurements on separate cables.

CONCLUSION

Electrical resistivity and induced polarization surveys were performed over a portion of the Vars-Winchester esker aquifer system near Embrun, Ontario. Data were acquired within boreholes as 1D logs, along the surface as 2D profiles, and from surface-to-borehole in 3D. The data were processed and inverted to recover 1D, 2D and 3D models of electrical resistivity and chargeability. The different resistivity models are largely self consistent and reveal a resistive esker aquifer that can be mapped both across and along strike. The esker is encased by conductive Champlain Sea marine muds. Both the esker aquifer and the mud aquiclude have coherent internal structure visible in the resistivity models that may be indicative of variable hydrogeological properties. Meaningful chargeability models were only recovered as 1D apparent chargeability logs and show small but measurable chargeability with generally uniform levels of normalized chargeability or surface conduction. The most significant discrepancies in the models result from disparate levels of resolution between the surface and borehole surveys. The borehole surveys provide more detailed measurements of electrical properties, while the surface models allow for extrapolation of results for aquifer mapping at a lower level of detail and accuracy. The 3D surveys suffer from significant uncertainty associated with non-uniqueness.

ACKNOWLEDGEMENTS

This work is part of the Natural Resources Canada Groundwater Geoscience Program. Field data acquisition assistance by K. Brewer, T. Cartwright, B. Dietiker, and M. Griffiths. Land access provided by A. Brisson, R. Bordeau, and the South Nation Conservation Authority. Internal review by B. Dietiker. Raw data and models are available from the author.

REFERENCES

Crow, H., Alpay, S., Hinton, M., Knight, R., Oldenborger, G., Percival, J.B., Pugin, A. J.-M., Pelchat P., 2017. Geophysical, geotechnical, geochemical, and mineralogical data sets collected in Champlain Sea sediments in the Municipality of Pontiac, Quebec. Geological Survey of Canada, Open File 7881.

Crow, H.L., Pugin, A.J.-M., Dietiker, B., Paradis, D., Brewer, K., Cartwright, T., Griffiths, M., Russell, H.A.J., 2019. Lithological and hydrogeological properties from a downhole geophysical dataset in the Vars-Winchester esker, Ontario. Geological Survey of Canada, Open File 8536, 147–158.

Cummings, D.I., Gorrell, G., Guilbault, J.-P., Hunter, J.A., Logan, C., Ponomarenko1, D., Pugin, A.J.-M., Pullan, S.E., Russell, H.A.J., Sharpe, D.R., 2011. Sequence stratigraphy of a glaciated basin fill with a focus on esker sedimentation. GSA Bulletin 123, 1478–1496.

Cummings, D.I., Russell, H.A.J., 2007. The Vars-Winchester esker aquifer, South Nation River watershed, Ontario. Geological Survey of Canada, Open File 5624.

Dahlin, T., Loke, M.H., 2015. Negative apparent chargeability in time-domain induced polarisation data. Journal of Applied Geophysics 123, 322–332.

Daily, W., Ramirez, A., Binley, A., LaBrecque, D., 2005. Electrical resistance tomography—Theory and practice, in: Near-Surface Geophysics, Investigations in Geophysics. Society of Exploration Geophysicists, 525–550.

Edwards, L.S., 1977. A modified pseudosection for resistivity and IP. Geophysics,42,1020–1036.

Florsch, N., Llubes, M., Téreygeol, F., Ghorbani, A., Roblet, P., 2011. Quantification of slag heap volumes and masses through the use of induced polarization, Journal of Archaeological Science 38, 438–451.

Foged, N., Auken, E., Christiansen, A.V., Sørensen, K.I., 2013. Test-site calibration and validation of airborne and ground-based TEM systems. Geophysics 78, E95–E106.

Høyer, A.-S., Jørgensen, F., Sandersen, P.B.E., Viezzoli, A., Møller, I., 2015. 3D geological modelling of a complex buried-valley network delineated from borehole and AEM data. Journal of Applied Geophysics 122, 94–102.

Hyde, C.S.B., Hunter, J.A., 1998. Formation electrical conductivity-porewater salinity relationships in Quaternary sediments from two Canadian sites, Symposium on the Application of Geophysics to Environmental and Engineering Problems, 499–510.

Jørgensen, F., Sandersen, P.B.E., 2009. Buried Valley mapping in Denmark: evaluating mapping method constraints and the importance of data density. Z. Dtsch. Ges. Geowiss. 160, 211–223.

LaBrecque, D., Daily, W., 2008. Assessment of measurement errors for galvanic-resistivity electrodes of different composition. Geophysics 73, F55–F64.

LaBrecque, D.J., Miletto, M., Daily, W., Ramirez, A., Owen, E., 1996. The effects of noise on Occam's inversion of resistivity tomography data. Geophysics 61, 538–548.

LaBrecque, D.J., Oldenborger, G.A., Sharpe, R., Knoll, M.D., 2006. Axi-symmetric inversion of electrical resistivity tomography data to monitor the movement of fluids injected in wells. Symposium on the Application of Geophysics to Environmental and Engineering Problems, 1505–1513.

Lesmes, D.P., Frye, K.M., 2001. Influence of pore fluid chemistry on the complex conductivity and induced polarization responses of Berea sandstone. Journal of Geophysical Research 106, 4079–4090.

Li, Y., Oldenburg, D.W., 2000. 3-D inversion of induced polarization data. Geophysics 65, 1931–1945.

Loke, M.H., Dahlin, T., Rucker, D.F., 2014. Smoothness-constrained time-lapse inversion of data from 3D resistivity surveys. Near Surface Geophysics 12, 5–24.

Maurer, H., Friedel, S., Jaeggi, D., 2009. Characterization of a coastal aquifer using seismic and geoelectric borehole methods. Near Surface Geophysics 7, 353–366.

Maurya, P.K., Balbarini, N., Møller, I., Rønde, V., Christiansen, A.V., Bjerg, P.L., Auken, E., Fiandaca, G., 2018. Subsurface imaging of water electrical conductivity, hydraulic permeability and lithology at contaminated sites by induced polarization, Geophysical Journal International 213, 770–785.

McLachlan, P., Chambers, J., Uhlemann, S., Binley, A., 2020. Electrical resistivity and induced polarization imaging of riverbed sediments: Observations from laboratory, field and synthetic experiments, Journal of Applied Geophysics, in press, 104173.

Nabighian, M.N., Elliot, C.L., 1976. Negative induced–polarization effects from layered media. Geophysics 41, 1236–1255.

Oldenborger, G.A., Routh, P.S., Knoll, M.D., 2007. Model reliability for 3D electrical resistivity tomography: Application of the volume of investigation index to a time-lapse monitoring experiment. Geophysics 72, F167–F175.

Oldenborger, G.A., LeBlanc, A.-M., 2015. Geophysical characterization of permafrost terrain at Iqaluit International Airport, Nunavut. Journal of Applied Geophysics 123, 36–49.

Oldenborger, G.A., LeBlanc, A.-M., 2018. Monitoring changes in unfrozen water content with electrical resistivity surveys in cold continuous permafrost. Geophysical Journal International 215, 965–977.

Oldenborger, G.A., Pugin, A.J.-M., Pullan, S.E., 2013. Airborne time-domain electromagnetics, electrical resistivity and seismic reflection for regional three-dimensional mapping and characterization of the Spiritwood valley aquifer, Manitoba, Canada. Near Surface Geophysics 11, 63–74.

Oldenburg, D.W., Li, Y., 1999. Estimating depth of investigation in DC resistivity and IP surveys. Geophysics 64, 403–416.

Paradis, D., Pugin, A., Crow, H., Oldenborger, G., Russell, H., Melaney, M., 2019. Hydro-geophysics for the characterization of hydraulic properties of a buried esker system: An overview. Geological Survey of Canada, Open File 8536, 131–138.

Pugin, A.J.-M., Pullan, S.E., Hunter, J.A., Oldenborger, G.A., 2009. Hydrogeological prospecting using P- and S-wave landstreamer seismic reflection methods. Near Surface Geophysics 7, 315–327.

Pugin, A.J.-M., Crow, H.L., Brewer, K., Cartwright, T., Dietiker, B., Griffiths, M., Paradis, D., 2019. High-resolution seismic reflection profiles for groundwater studies on the Vars-Winchester esker, southern Ontario. Geological Survey of Canada, Open File 8536, 139–146.

Revil, A., Coperey, A., Shao, Z., Florsch, N., Fabricius, I.L., Deng, Y., Delsman, J.R., Pauw, P.S., Karaoulis, M., de Louw, P.G.B., van Baaren, E.S., Dabekaussen, W., Menkovic, A., Gunnink, J.L., 2017. Complex conductivity of soils. Water Resources Research 53, 7121–7147.

Sauriol, J., 2016. Provenance of buried esker groundwater: the case of Vars-Winchester esker aquifer, Eastern Ontario, Canada. Hydrogeology Journal 24, 123–139.

Shaver, R.B., Pusc, S.W., 1992. Hydraulic barriers in Pleistocene buried-valley aquifers. Ground Water 30, 21–28.

Sie, D., Little, J., 1976. Groundwater

Siemon, B., Christiansen, A.V., Auken, E., 2009. A review of helicopter-borne electromagnetic methods for groundwater exploration. Near Surface Geophysics 7, 629–646.

Slater, L., 2007. Near surface electrical characterization of hydraulic conductivity: From petrophysical properties to aquifer geometries—A review. Surveys in Geophysics 28, 169–197.

Slater, L.D., Glaser, D.R., 2003. Controls on induced polarization in sandy unconsolidated sediments and application to aquifer characterization. Geophysics 68, 1547–1558.

Slater, L.D., Lesmes, D., 2002. IP interpretation in environmental investigation. Geophysics 67, 77–88.

Steuer, A., Siemon, B., Auken, E., 2009. A comparison of helicopter-borne electromagnetics in frequency- and time-domain at the Cuxhaven valley in Northern Germany. Journal of Applied Geophysics 67, 194–205.

Torrance, J.K., 1983. Towards a general model of quick clay development. Sedimentology 30, 547–555.

Weller, A., Slater, L., Binley, A., Nordsiek, S., Xu, S., 2015. Permeability prediction based on induced polarization: Insights from measurements on sandstone and unconsolidated samples spanning a wide permeability range. Geophysics 80, D161–D173.

Zonge, K., Hughes, L., 1985. Effect of electrode contact resistance on electric field measurements, SEG Expanded Abstracts, 231–234.

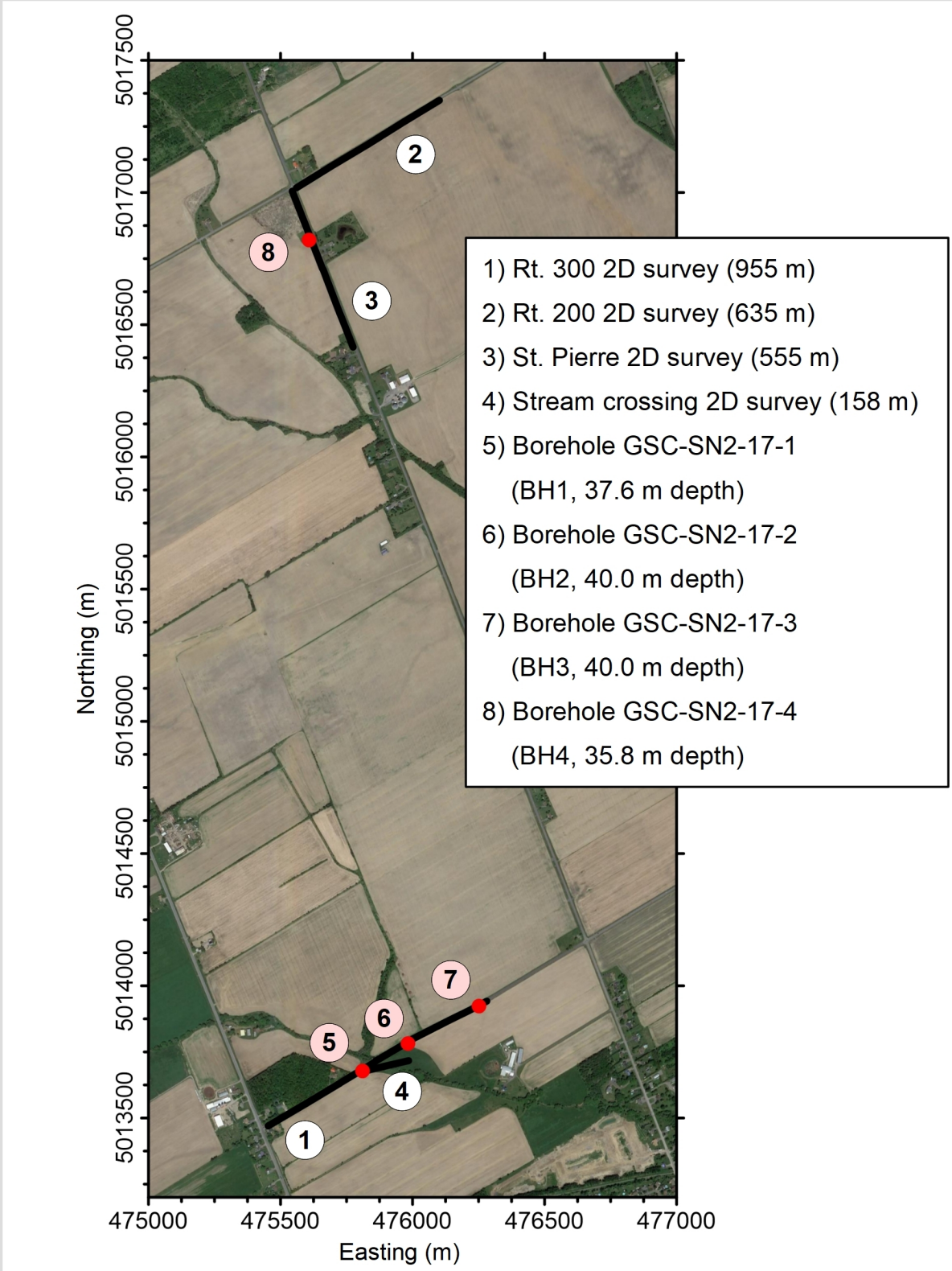

Figure 1. Study area showing locations of electrical resistivity surveys and boreholes. Map image: 1 June 2018, © 2020 Google.

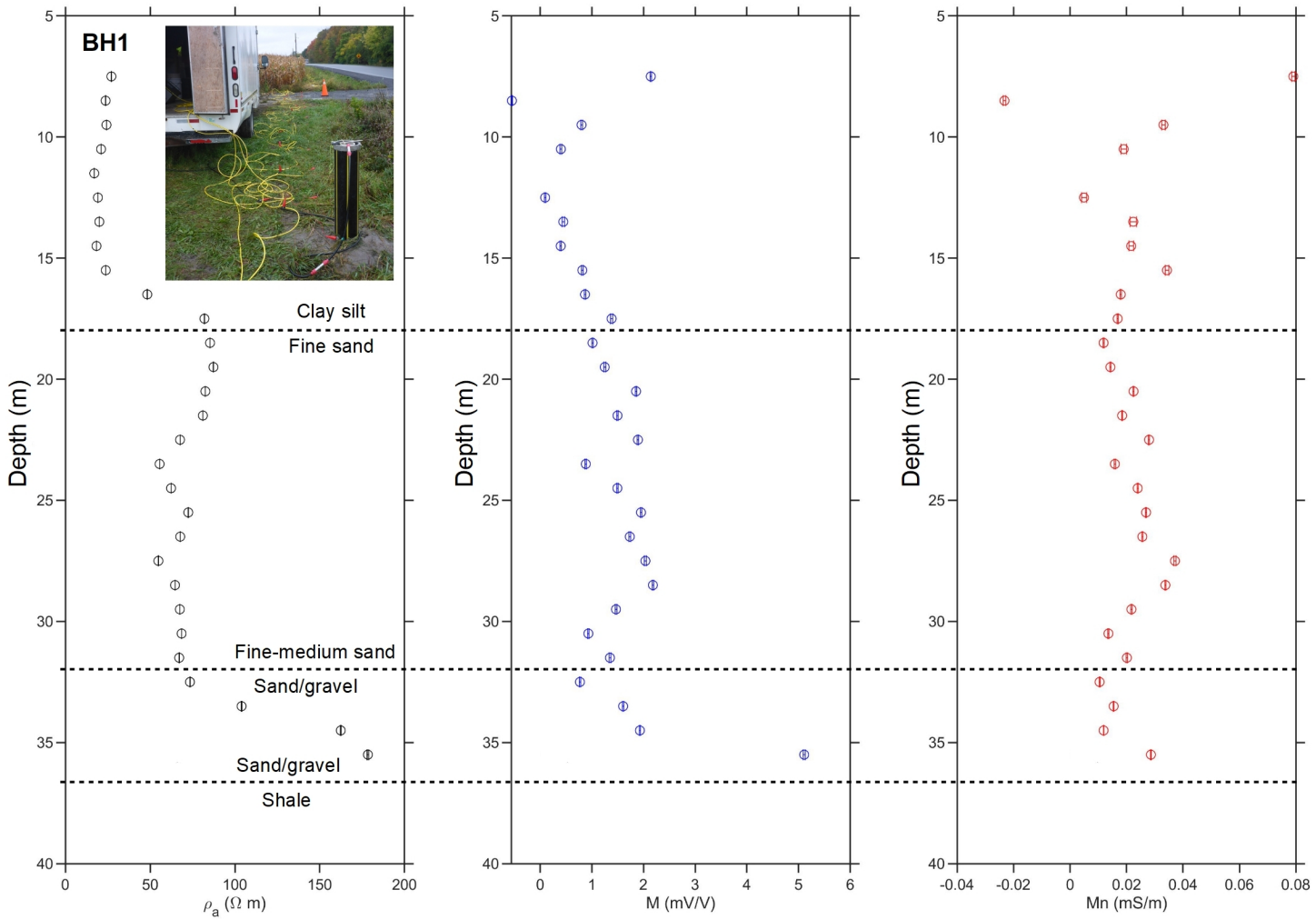

Figure 2. Apparent resistivity, apparent chargeability and normalized apparent chargeability logs for borehole-only measurements from BH1. Data are plotted in depth from surface (69.1 m elevation) at the midpoint of a 3 m quadrupole. Major lithological contacts from the drill logs are shown. Photograph of BH1 with electrode layout by G.A. Oldenborger. NRCan photo 2020-891

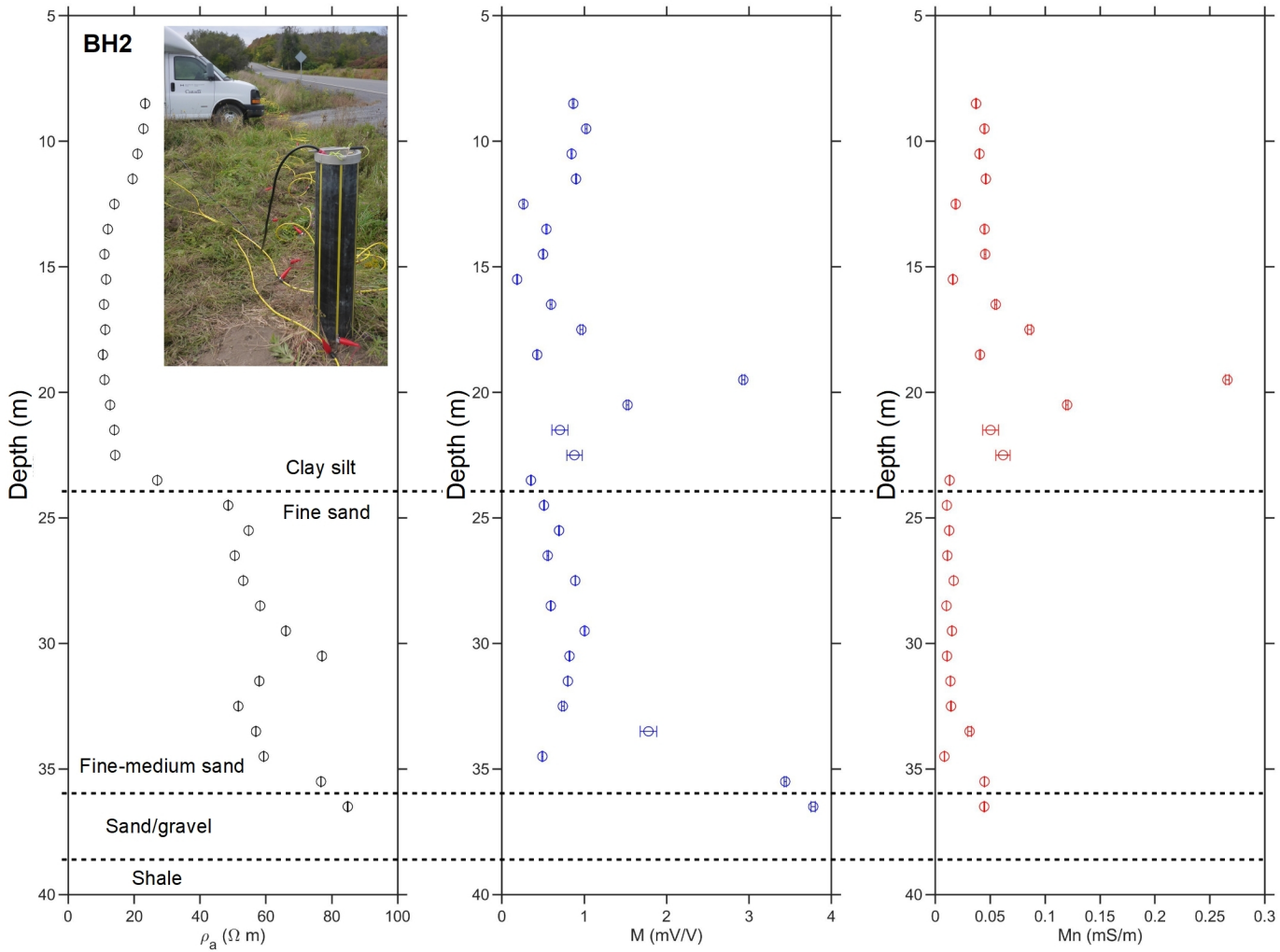

Figure 3. Apparent resistivity, apparent chargeability and normalized apparent chargeability logs for borehole-only measurements from BH2. Data are plotted in depth from surface (70.0 m elevation) at the midpoint of a 3 m quadrupole. Major lithological contacts from the drill logs are shown. Photograph of BH2 with electrode layout by G.A. Oldenborger. NRCan photo 2020-892

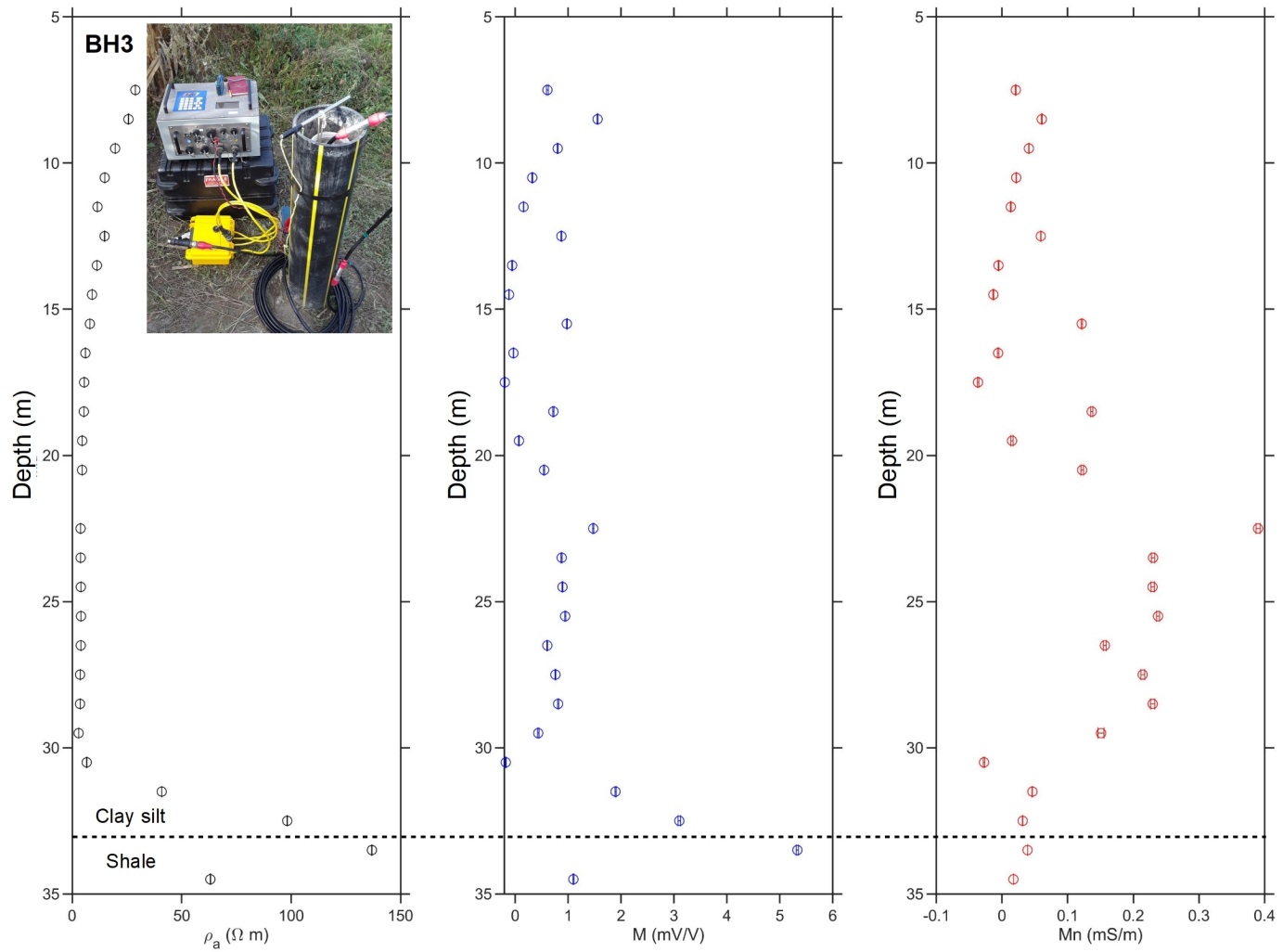

Figure 4. Apparent resistivity, apparent chargeability and normalized apparent chargeability logs for borehole-only measurements from BH3. Data are plotted in depth from surface (69.8 m elevation) at the midpoint of a 3 m quadrupole. Major lithological contacts from the drill logs are shown. Photograph of BH3 with instrumentation by G.A. Oldenborger. NRCan photo 2020-893

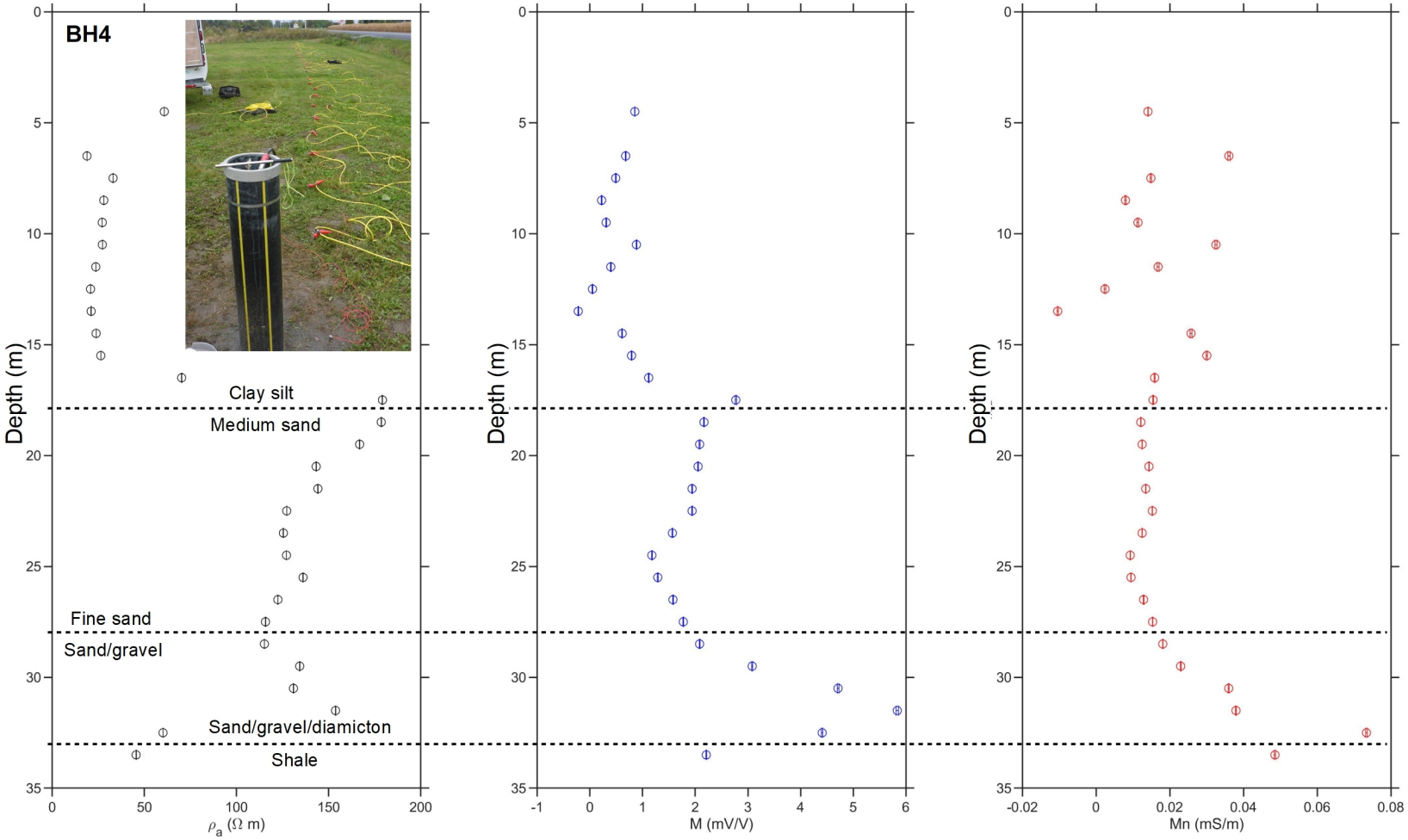

Figure 5. Apparent resistivity, apparent chargeability and normalized apparent chargeability logs for borehole-only measurements from BH4. Data are plotted in depth from surface (72.3 m elevation) at the midpoint of a 3 m quadrupole. Major lithological contacts from the drill logs are shown. Photograph of BH4 with electrode layout by G.A. Oldenborger. NRCan photo 2020-894

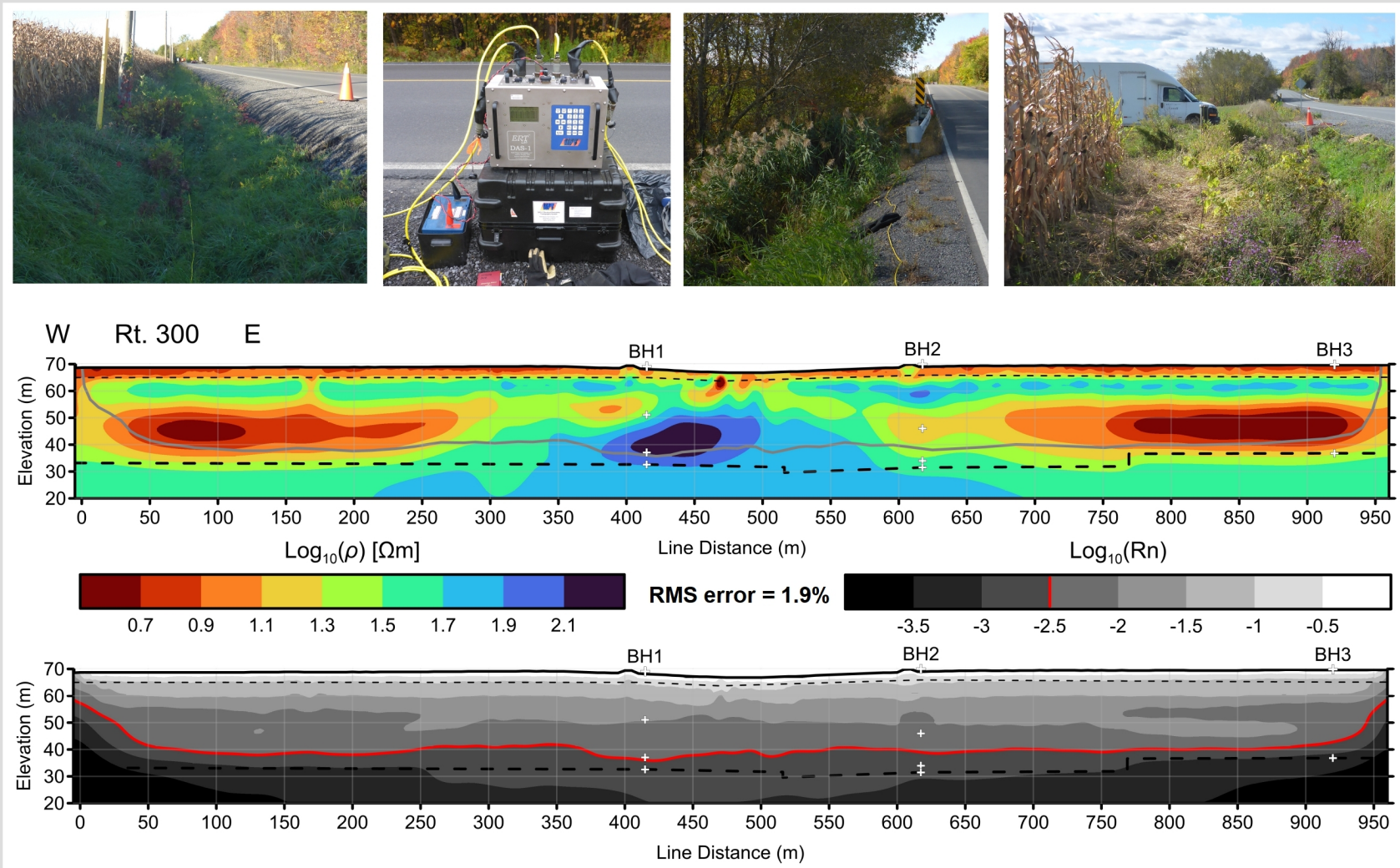

Figure 6. Electrical resistivity model and normalized resolution for the Rt. 300 surface survey. Location and major lithological contacts for the 2017 boreholes are shown. The upper dashed line is the water table at the time of acquisition. The lower dashed line is the bedrock surface used to constrain the inversion. The solid grey line indicates the approximate limit of model reliability. Photographs of survey location and instrumentation by G.A. Oldenborger. NRCan photos 2020-895, 2020-896, 2020-897, 2020-898

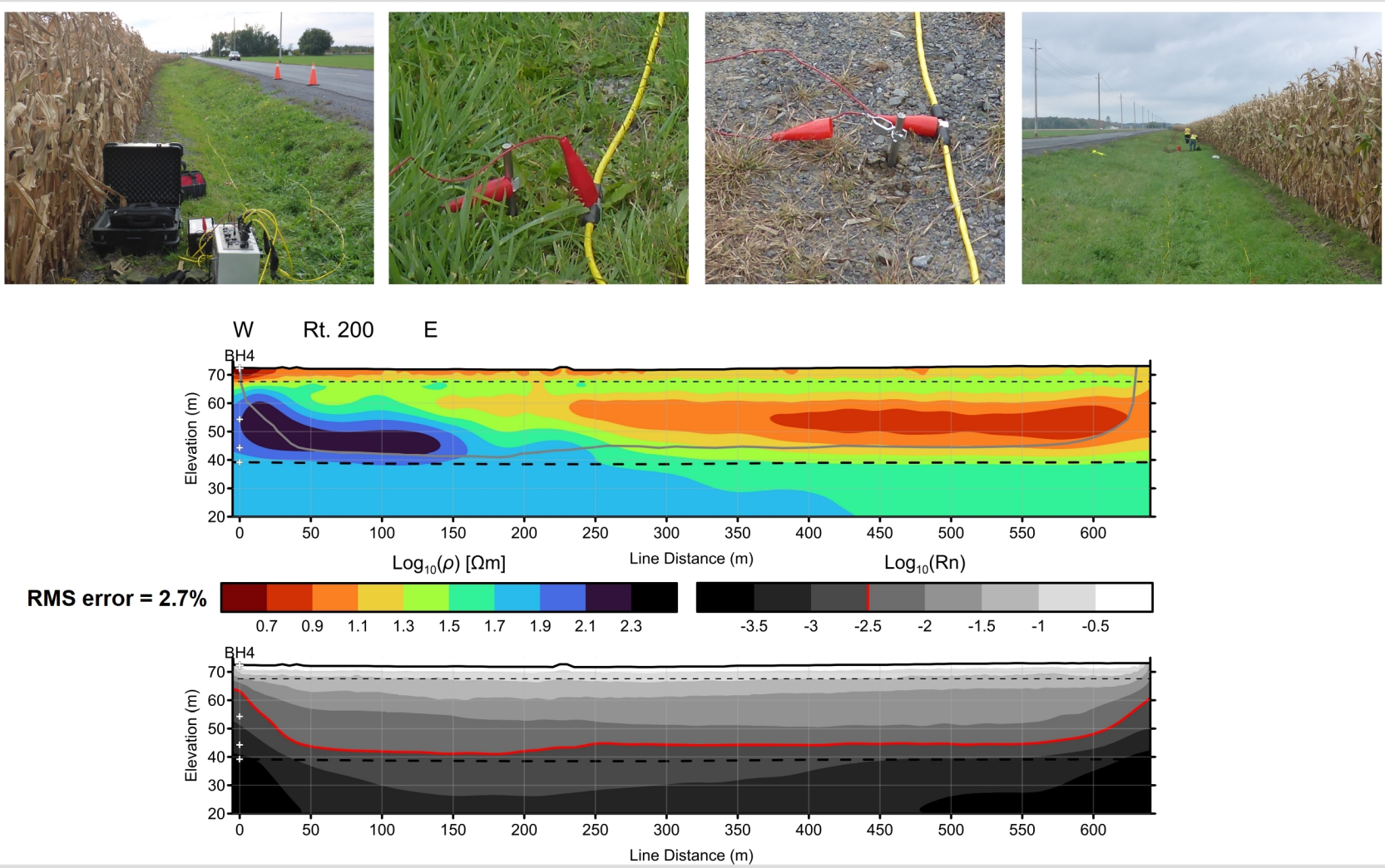

Figure 7. Electrical resistivity model and normalized resolution for the Rt. 200 surface survey. The major lithological contacts for BH4 are projected onto the survey line from approximately 200 m south. The upper dashed line is the water table from BH4 at the time of acquisition. The lower dashed line is the bedrock surface from BH4 used to constrain the inversion. The solid grey line indicates the approximate limit of model reliability. Photographs of survey location and conditions by G.A. Oldenborger. NRCan photos 2020-899, 2020-900, 2020-901, 2020-902

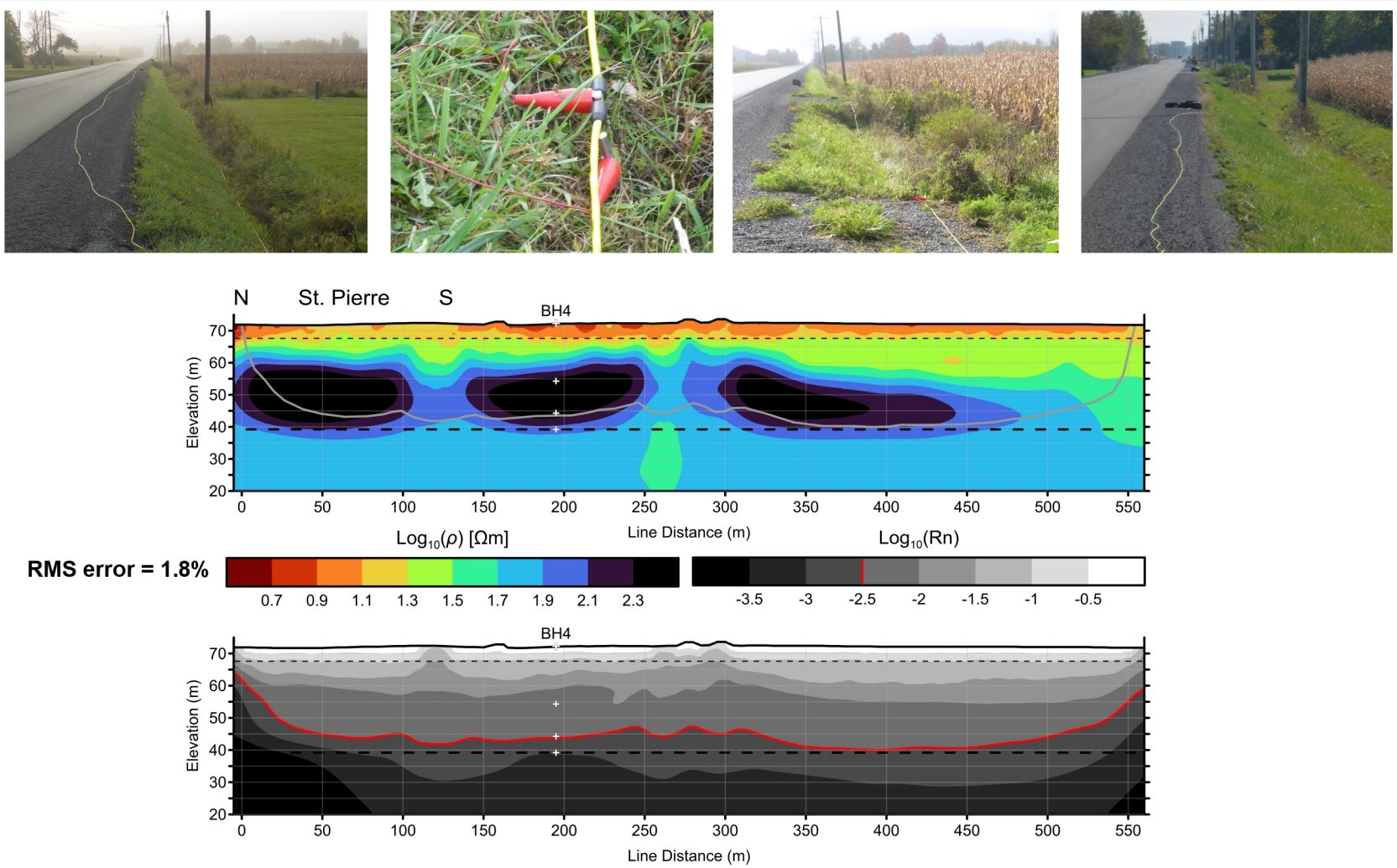

Figure 8. Electrical resistivity model and normalized resolution for the St. Pierre surface survey. The major lithological contacts for BH4 are projected onto the survey line from approximately 20 m west. The upper dashed line is the water table from BH4 at the time of acquisition. The lower dashed line is the bedrock surface from BH4 used to constrain the inversion. The solid grey line indicates the approximate limit of model reliability. Photographs of survey location and conditions by G.A. Oldenborger. NRCan photos 2020-903, 2020-904, 2020-905, 2020-906

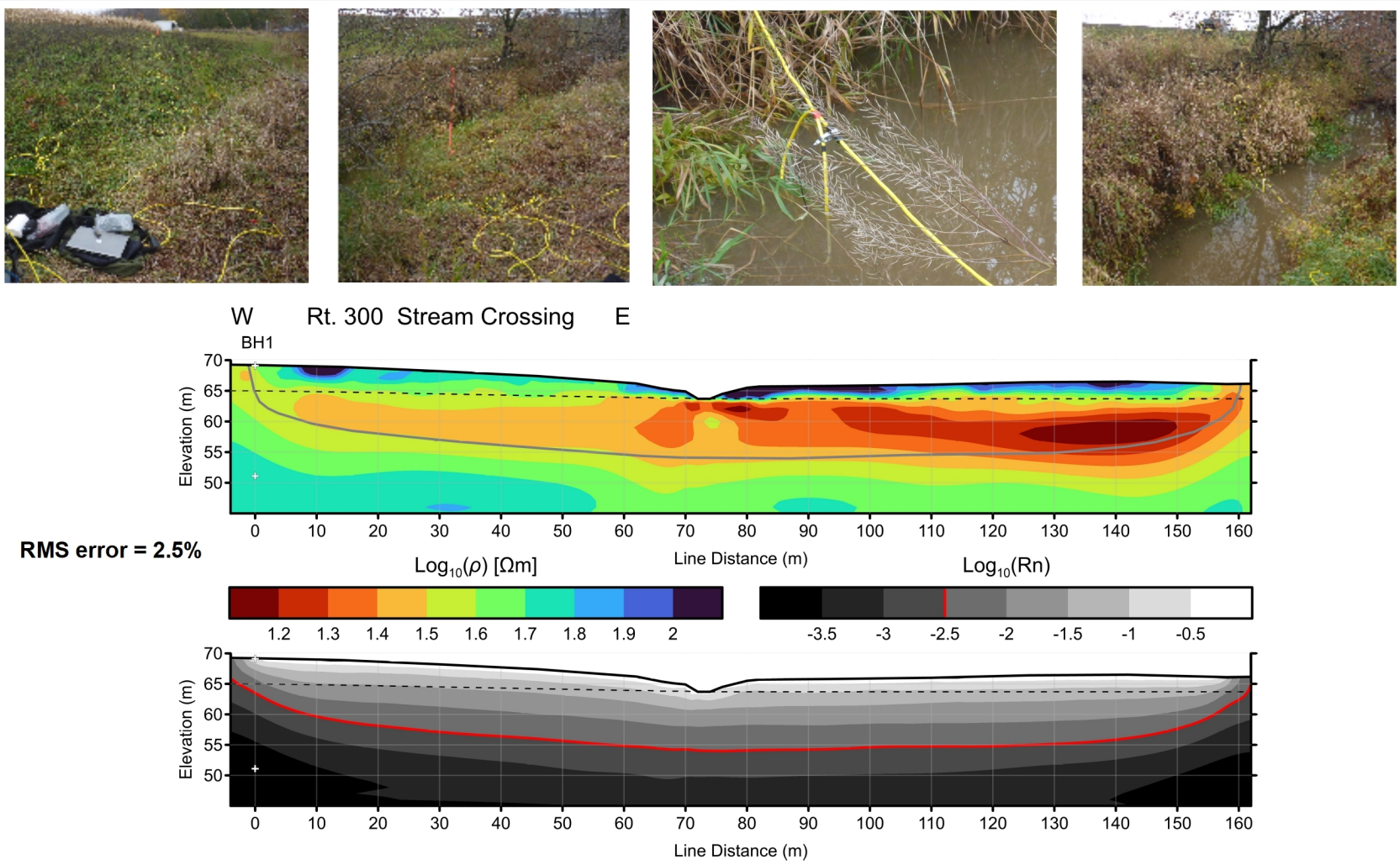

Figure 9. Electrical resistivity model and normalized resolution for the Rt. 300 stream crossing survey. The location and major lithological contacts for BH1 are projected onto the survey line from approximately 20 m west. The upper dashed line is the water table projected from BH1 at the time of acquisition and interpolated to the stream water elevation. The solid grey line indicates the approximate limit of model reliability. Photographs of survey location and conditions by G.A. Oldenborger. NRCan photos 2020-907, 2020-908, 2020-909, 2020-910

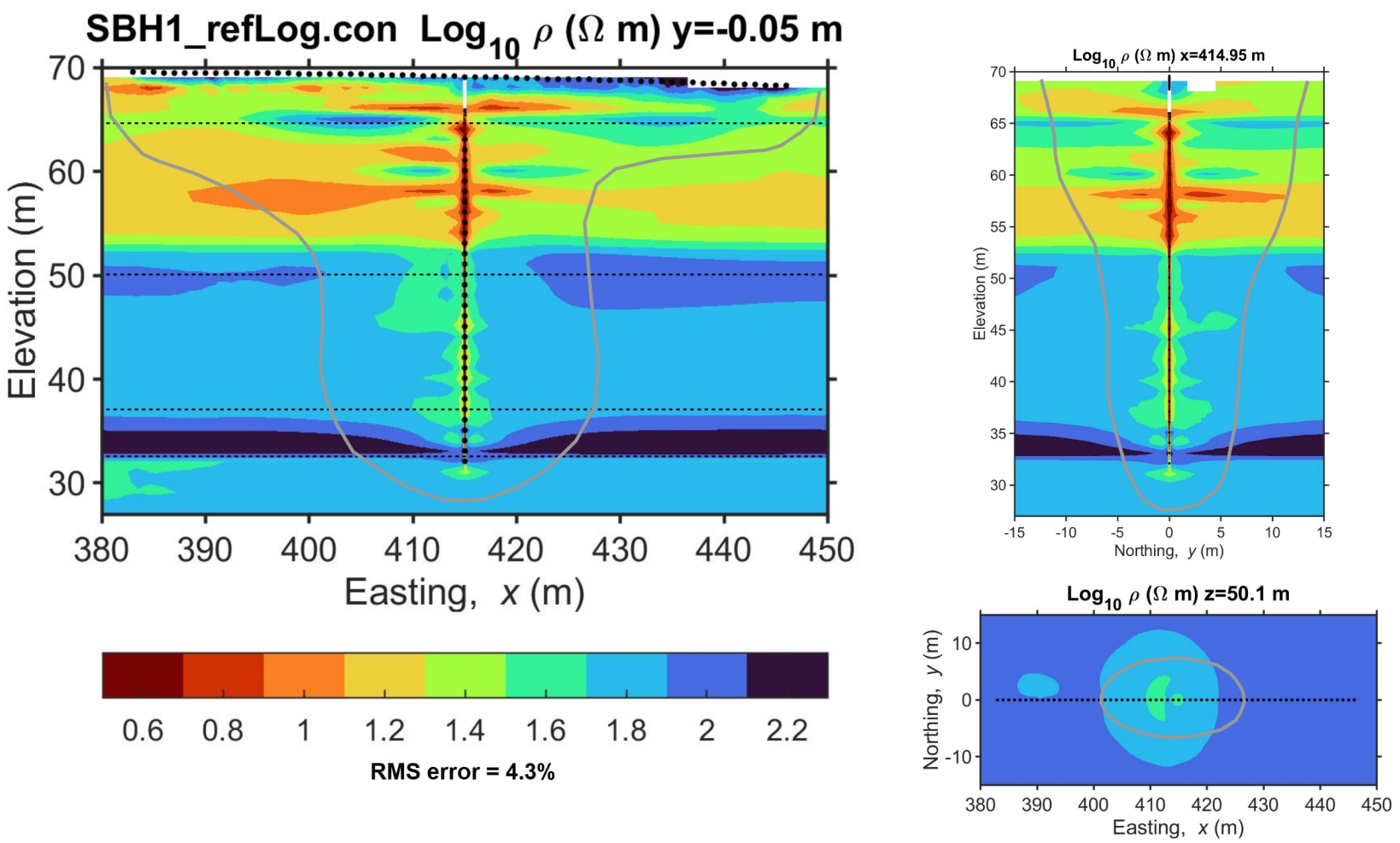

Figure 10. Electrical resistivity model for the BH1 surface-to-borehole survey. Locations of electrodes and major lithological contacts for the borehole are shown. The upper dashed line is the water table at the time of acquisition. The solid grey line indicates the approximate limit of model reliability.

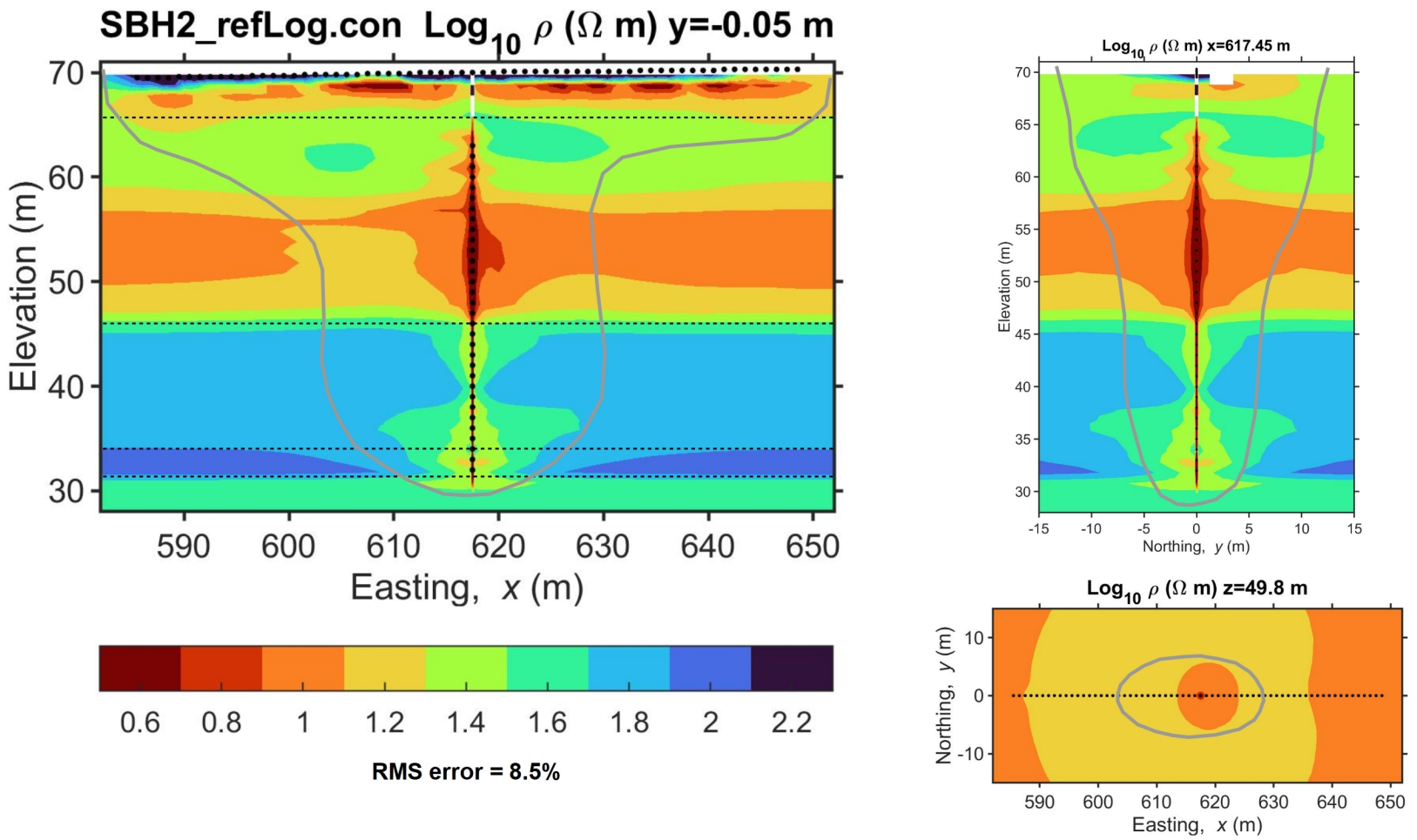

Figure 11. Electrical resistivity model for the BH2 surface-to-borehole survey. Locations of electrodes and major lithological contacts for the borehole are shown. The upper dashed line is the water table at the time of acquisition. The solid grey line indicates the approximate limit of model reliability.

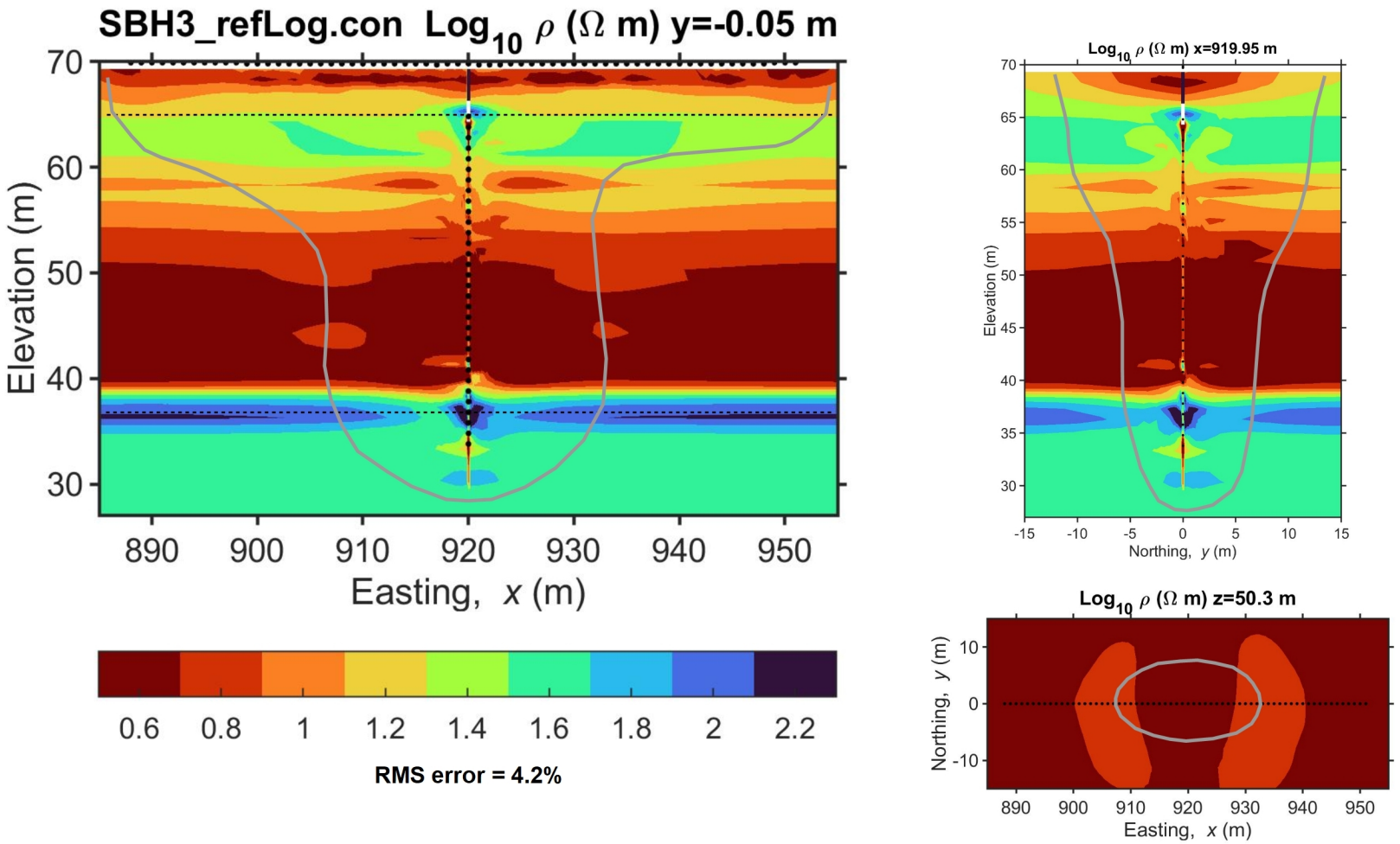

Figure 12. Electrical resistivity model for the BH3 surface-to-borehole survey. Locations of electrodes and major lithological contacts for the borehole are shown. The upper dashed line is the water table at the time of acquisition. The solid grey line indicates the approximate limit of model reliability.

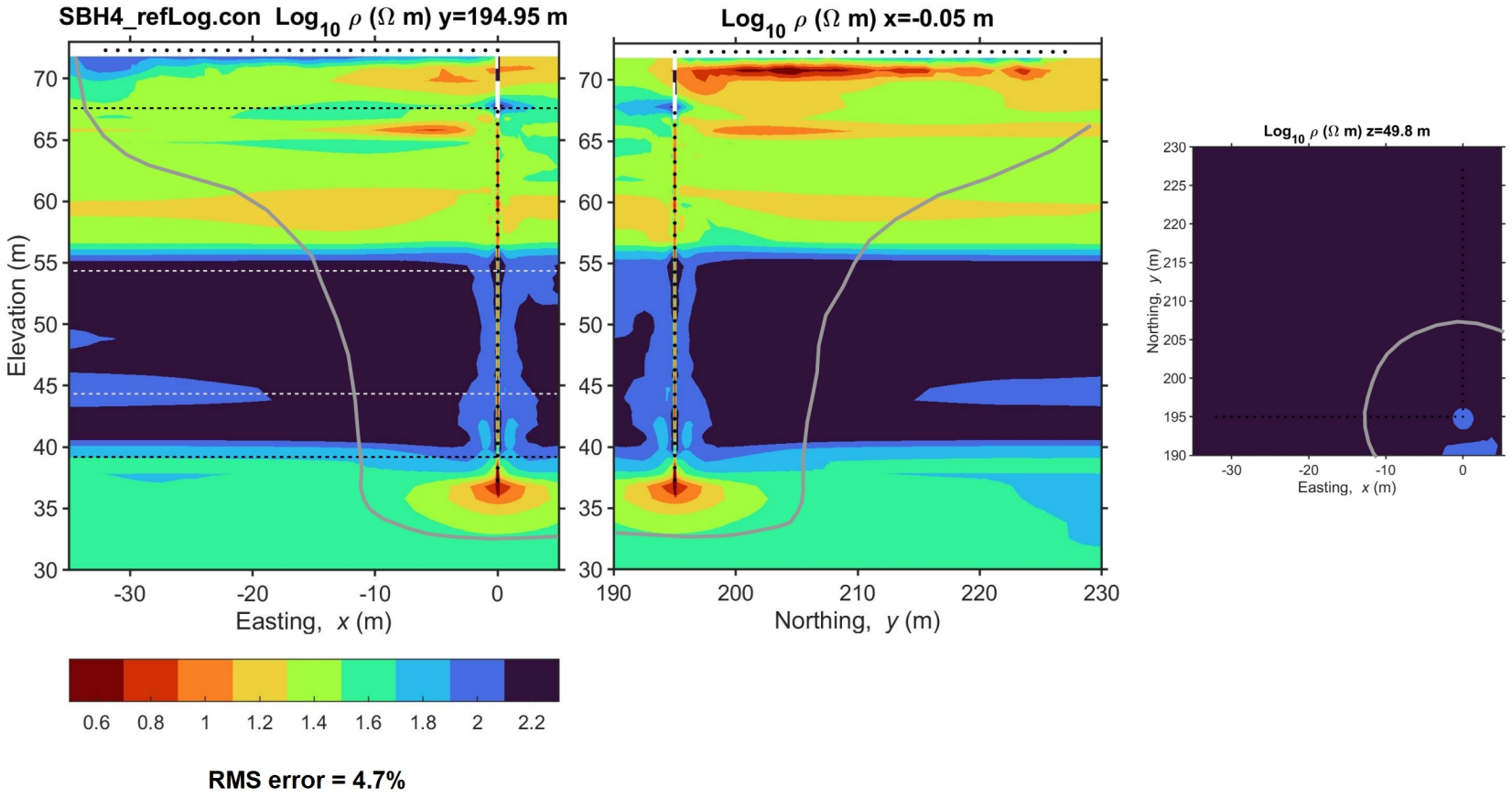

Figure 13. Electrical resistivity model for the BH4 surface-to-borehole survey. Locations of electrodes and major lithological contacts for the borehole are shown. The upper dashed line is the water table at the time of acquisition. The solid grey line indicates the approximate limit of model reliability.

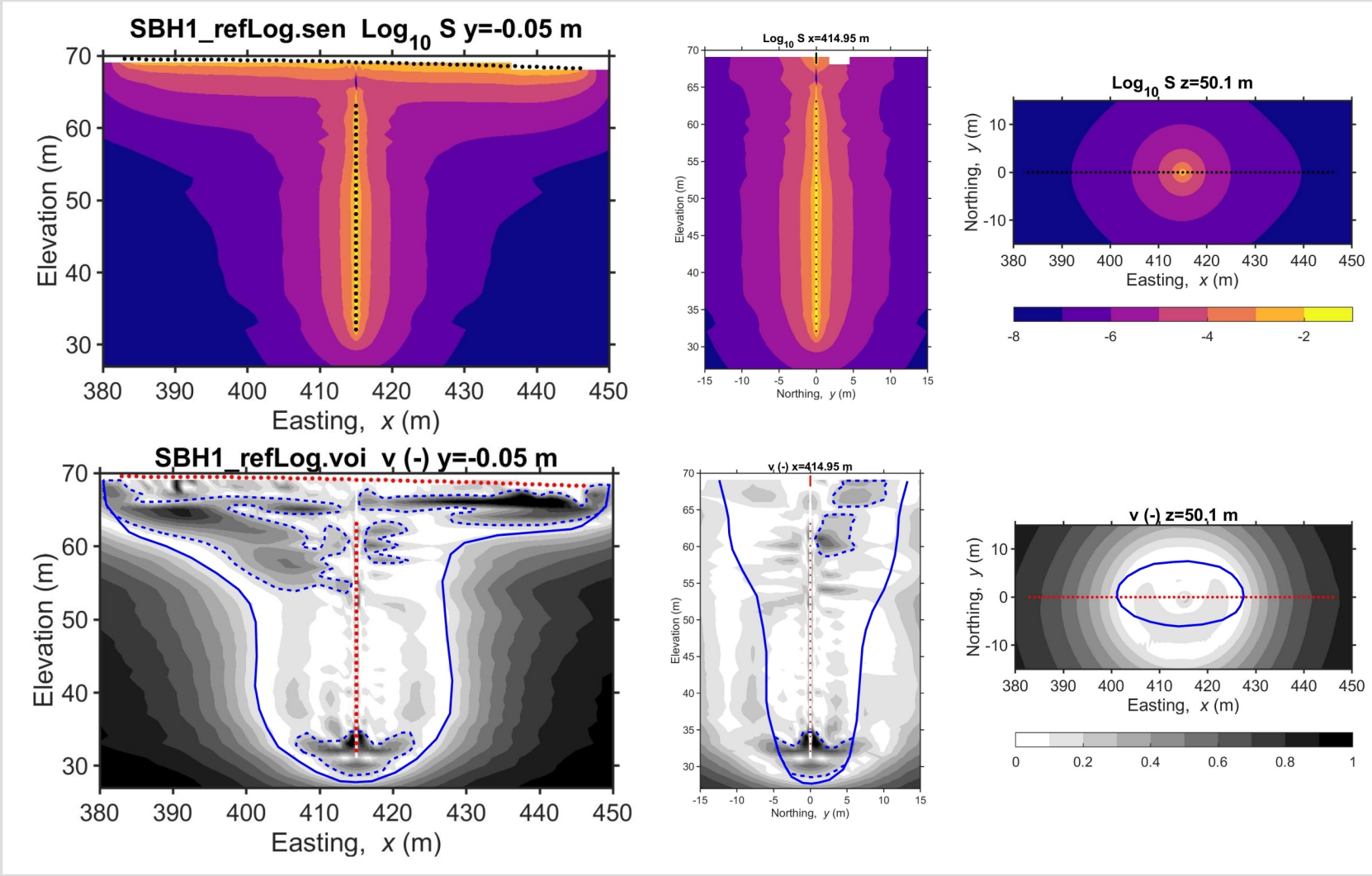

Figure 14. Average absolute sensitivity and volume of investigation for the BH1 surface-to-borehole survey. The solid blue contours indicate the interpreted limit of reliability for the model due to loss of sensitivity. The dashed blue contours indicate regions of unreliability resulting from model non-uniqueness.

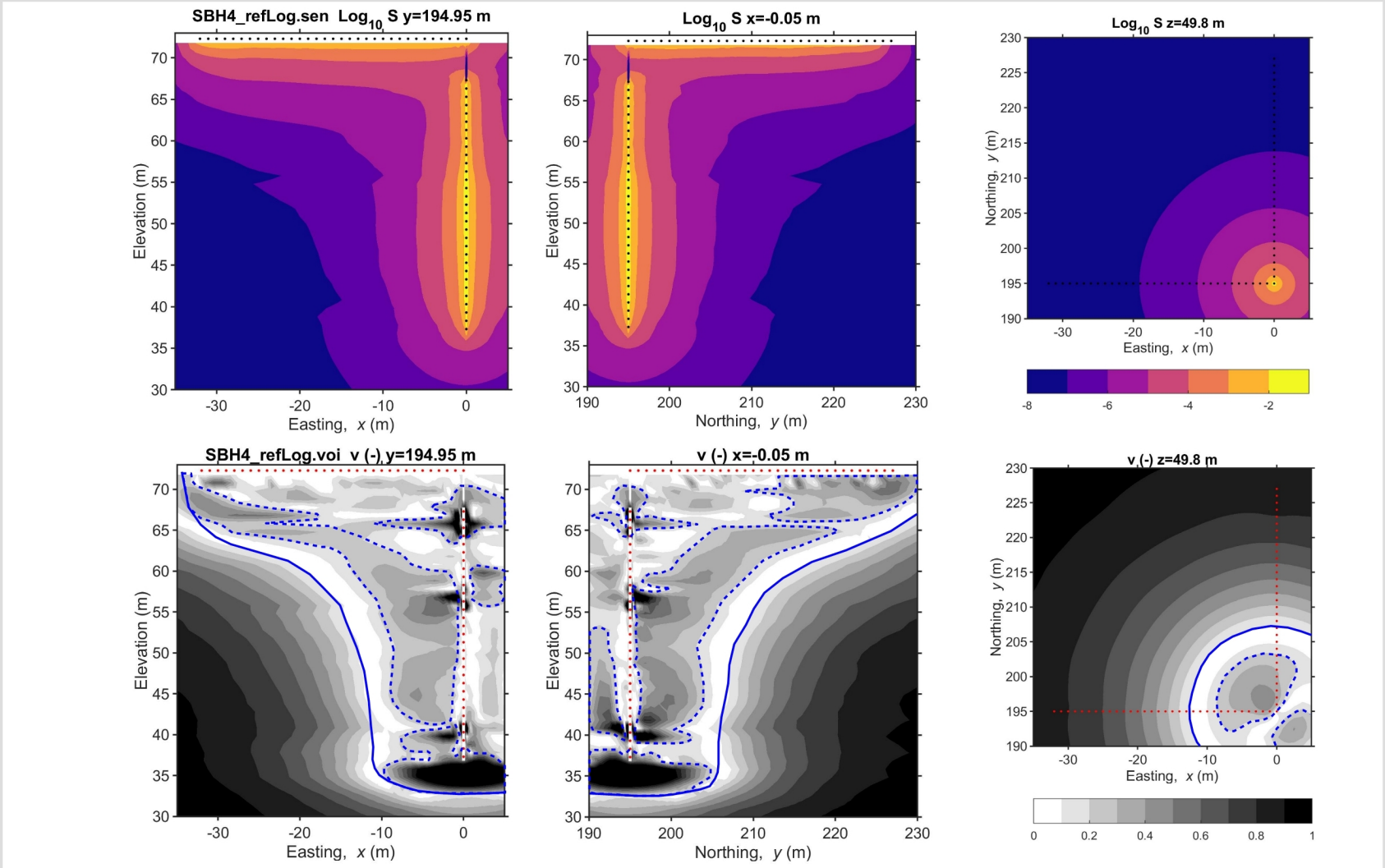

Figure 15. Average absolute sensitivity and volume of investigation for the BH4 surface-to-borehole survey. The solid blue contours indicate the interpreted limit of reliability for the model due to loss of sensitivity. The dashed blue contours indicate regions of unreliability resulting from model non-uniqueness.

APPENDIX A

Data processing follows a multi-step filtering protocol. Data were first filtered for injected current I and measured voltage V. Given the specified instrument measurement range and 24-bit AD conversion, instrument resolution is approximately 0.15 μA and 1.2 μV, but practical low-current and low-voltage limits were set as $|I| \geq 0.05$ mA and $|V| \geq 0.5$ mV (true zero-current or zero-voltage data are rare, usually indicate measurement failure, and are removed as problem quadrupoles). The data were then filtered based on repeatability as quantified by the standard deviation of the measured voltage s_V over the stacked waveforms. Resistivity data are highly repeatable, and measurements of $s_V \approx 0$ are routine despite systematic noise (e.g., LaBrecque and Daily, 2008). To better reflect this reality, the measurement error ΔV was estimated as

$$\Delta V = \max\left\{ s_V + r_V,\ p|V| \right\} \tag{A1}$$

where r_V is a constant bias or noise floor equivalent to the instrument resolution, and p is the limiting precision of the measurement. Although instrument resolution is 1.2 μV, examination of field data revealed an effective resolution of approximately 2.4 μV. Similarly, although specified instrument precision is 0.05% typical, examination of field data revealed an effective limiting precision of 0.03–0.04%. The values of $r_V = 2$ μV and $p = 0.04\%$ were used to compute ΔV, which was then used to compute the measurement error on the transfer resistance $R = V/I$. The data were subsequently filtered for $\Delta R \leq 3\%$. Measurement error on the current was considered negligible.

Time-domain chargeability was calculated from the measured voltage decays using the time-normalized integral formulation

$$M = \frac{1}{V_0 W} \int_{t_1}^{t_2} V(t)\,\mathrm{d}t \tag{A2}$$

where $W = t_2 - t_1$ defines the integration interval, and V_0 is the primary voltage before switch off (the measured DC voltage). In practice, sampling of the voltage decay is windowed, with the individual partial chargeabilities defined as

$$m_i = \frac{1}{V_0 w_i} \int_i V(t)\,\mathrm{d}t \approx V_i / V_0 \tag{A3}$$

where w_i is the window width and $W = \Sigma w_i$. Partial chargeability reported by most instruments is measured as the average off-time voltage for the window V_i normalized by the primary voltage, which is equivalent to the exact integral formulation (A3) only for linear decay (or short windows, or slow decays). Partial chargeability is only negative if the primary and decay window voltages are of opposite sign. The chargeability was approximated from the partial chargeabilities as

$$M \approx \frac{1}{W} \sum m_i w_i = \frac{1}{V_0 W} \sum V_i w_i. \tag{A4}$$

Chargeability is unitless (mV/V) and the measured value is dependent on the integration interval, the windows, and the delay after switch off. All 16 measurement windows were used to calculate *M*. Trials with different integration intervals showed that calculation of *M* (and the distribution of *M*) is relatively robust with respect to the choice of *W*. A longer integration interval generally results in reduced chargeability and smaller relative error, but changes in *M* with *W* are approximately linear. This observation is consistent with the findings that time-domain chargeability (A2) is proportional to the complex conductivity phase (Lesmes and Frye, 2001) or to the electrical chargeability of a Debye or Cole-Cole model (Florsh et al., 2011).

Since chargeability involves normalization by the primary voltage, it can lead to instability for experimental geometries that involve naturally small potentials, or zero crossings, such as general 3D or surface-to-borehole arrangements. Filtering out near-zero voltage and high chargeability improves stability, but the induced polarization data are more rigorously defined as the secondary voltage after switch off V_s normalized by the current (Li and Oldenburg, 1990). To avoid inductive noise, there is usually some delay between switch off and initiation of voltage decay measurements, such that measuring the true secondary potential can be difficult. The first window voltage $V_s \approx V_1$ is perhaps most representative, but it is very sensitive to measurement noise and sign reversals. Instead, the window-weighted time-average voltage $V_s \approx MV_0$ was used as the induced polarization datum for the surface-to-borehole surveys, which codifies an explicit relationship between the secondary voltage and the chargeability. The data herein exhibit a linear relationship between the two measures of secondary voltage, but the average measure is far more stable and exhibits similar relative error statistics to the total chargeability, such that filters on chargeability can be used as a proxy for secondary voltage.

The measurement error for total chargeability ΔM or secondary potential ΔV_s was computed based on equation (A4) with quadrature error propagation of the measurement error of the individual window voltages (including resolution and precision). Voltage decays are not nearly as repeatable as resistance measurements, and summation compounds the measurement error, such that relative chargeability errors are larger than for resistance. The chargeability data (but not the associated resistance data) were filtered for $\Delta M \leq 30\%$ where the threshold was chosen to retain most of the continuous error distribution (e.g., Slater and Glaser, 2003). Furthermore, although decay voltage and chargeability can be negative, decay reversals are an indication of noise. The data were filtered to remove chargeabilities (but not the associated transfer resistance) associated with decay reversals exhibiting a window-to-window sign reversal amplitude greater than some threshold. The threshold was chosen as 4 mV/V based on trial and error removal of large oscillations at early time, but not minor oscillations at late time. If required, the stricter condition of time-averaged positivity of chargeability can be enforced with $M > 0$ for both *M* and V_s.

APPENDIX B

Example data and data processing steps for the **Rt. 300** surface acquisition (Figure 1). Figures show the measured data, the measurement errors, and the results of filtering discussed in the report. See the full report and Appendix A for details.

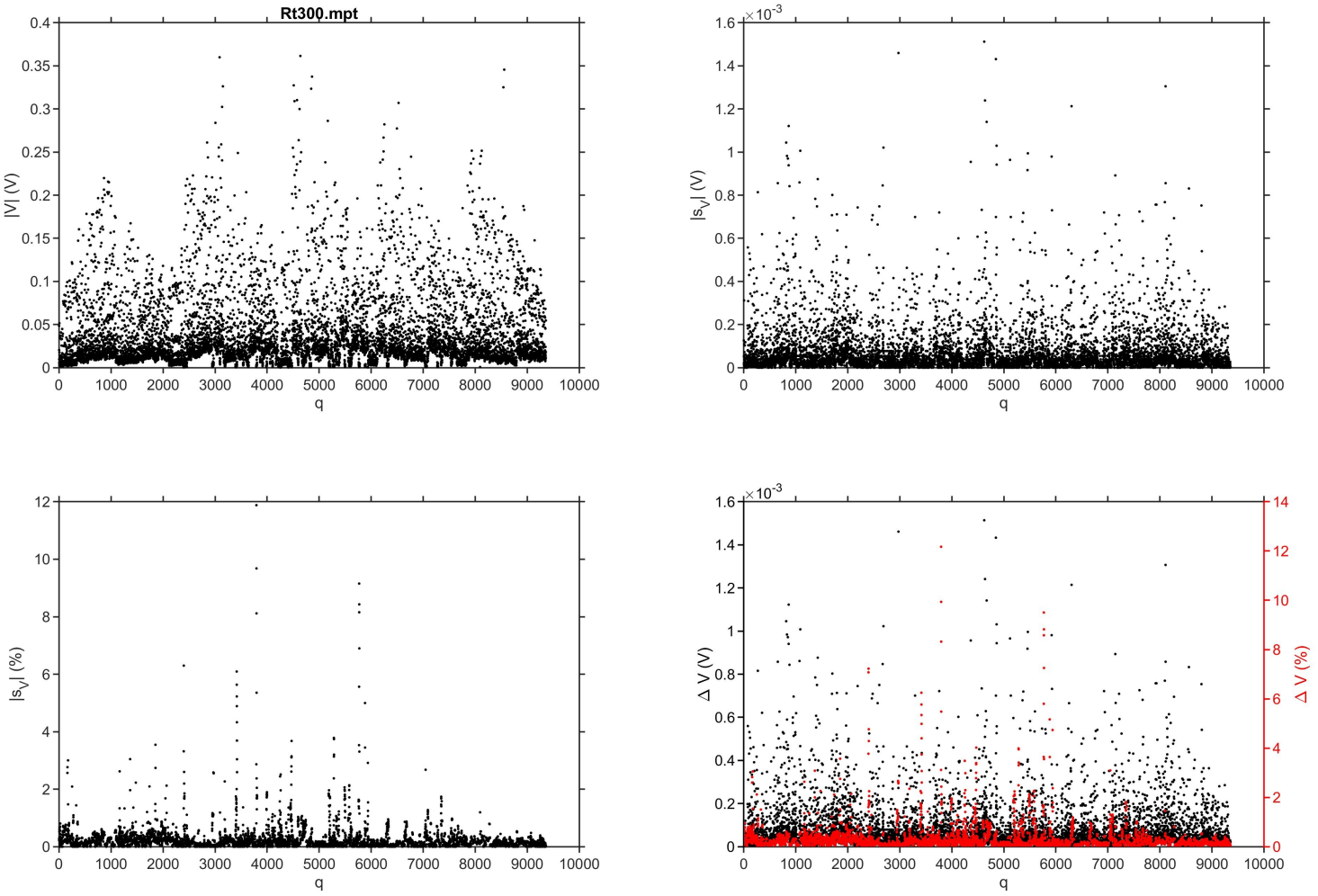

Figure B1. Voltage measurements and measurement error for each quadrupole measurement *q*.

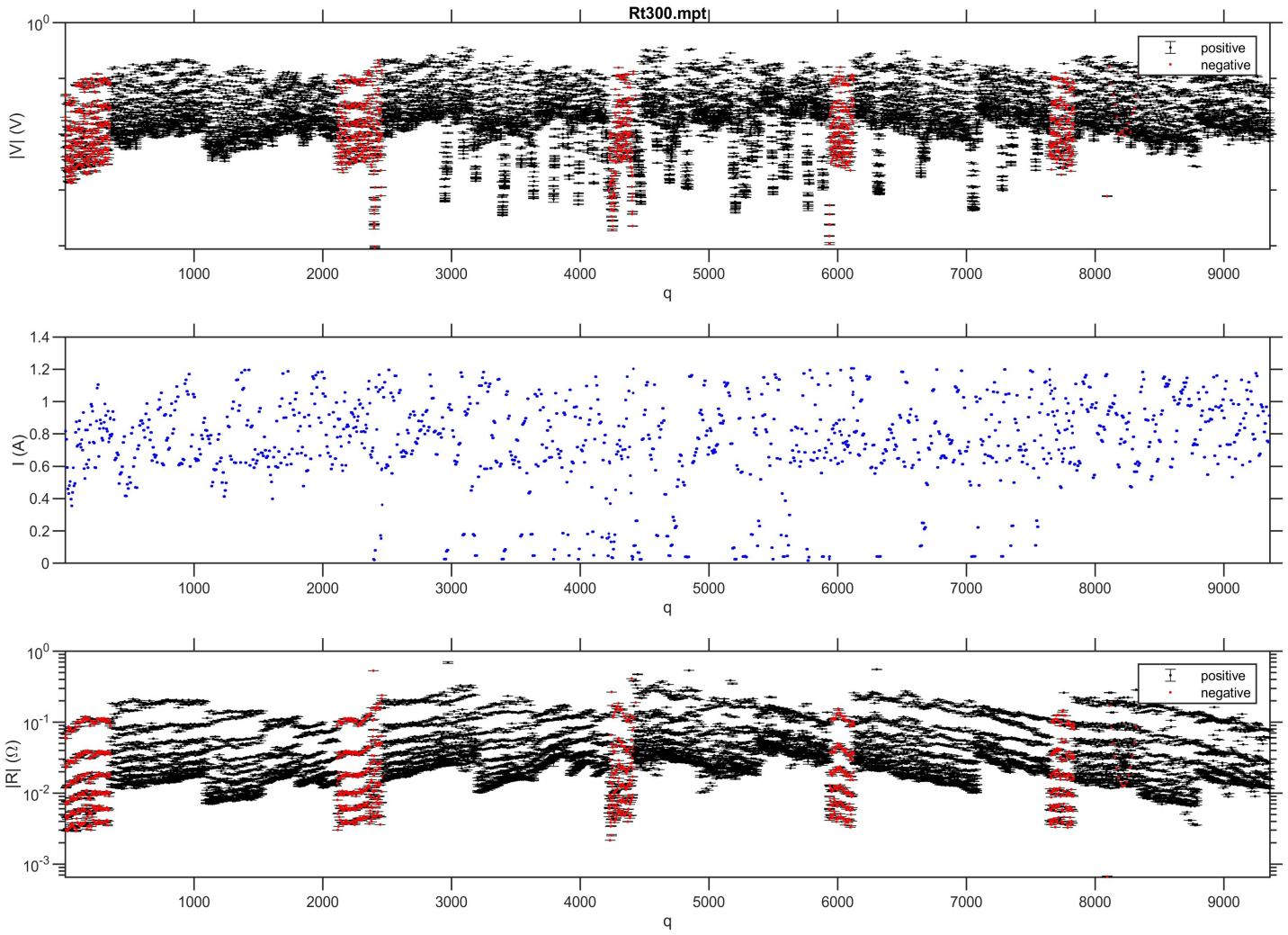

Figure B2. Voltage, current, and transfer resistance for each quadrupole measurement *q*. Negative values are depicted in red on the logarithmic scales.

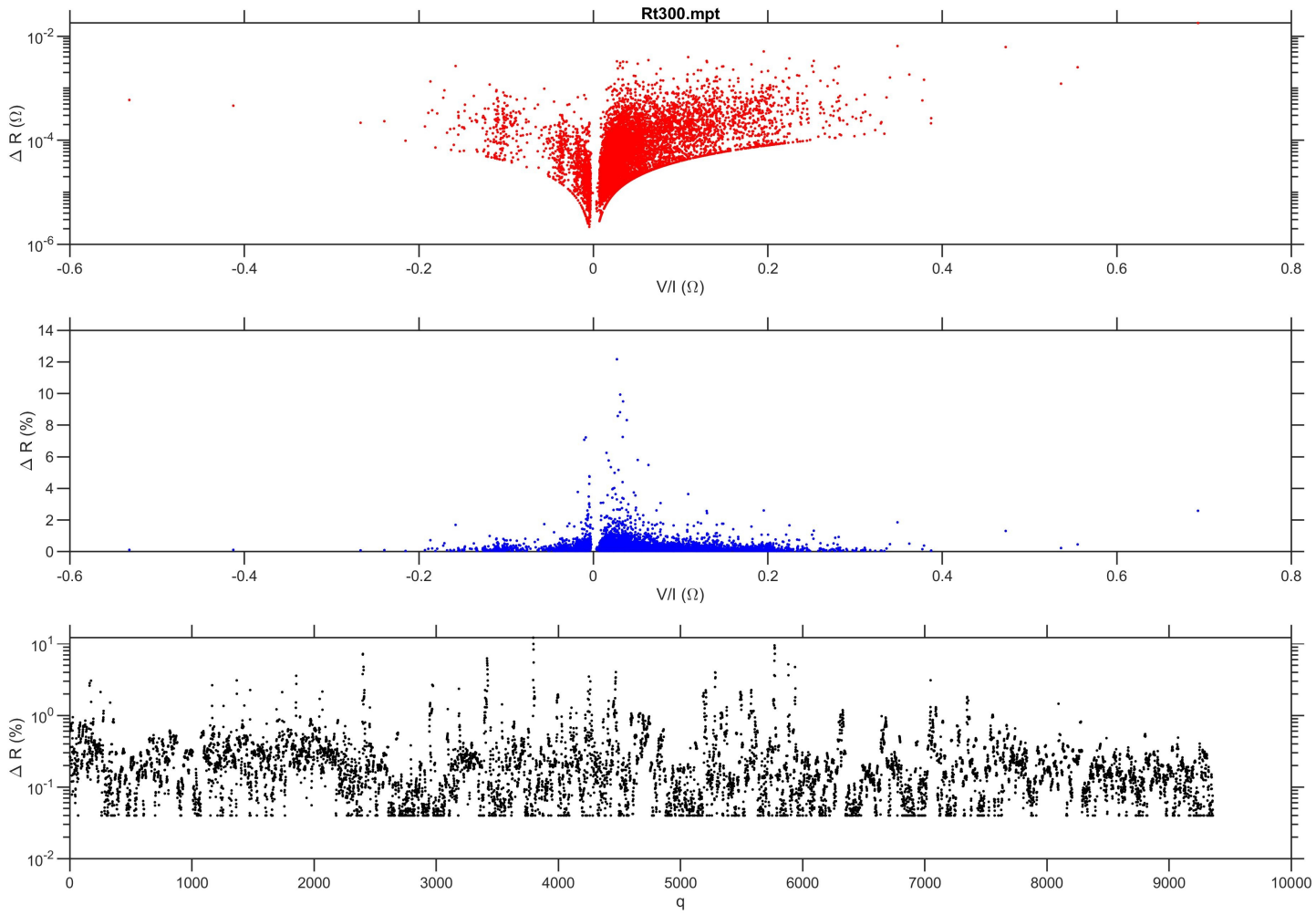

Figure B3. Transfer resistance measurement error as a function of transfer resistance, and for each quadrupole measurement *q*.

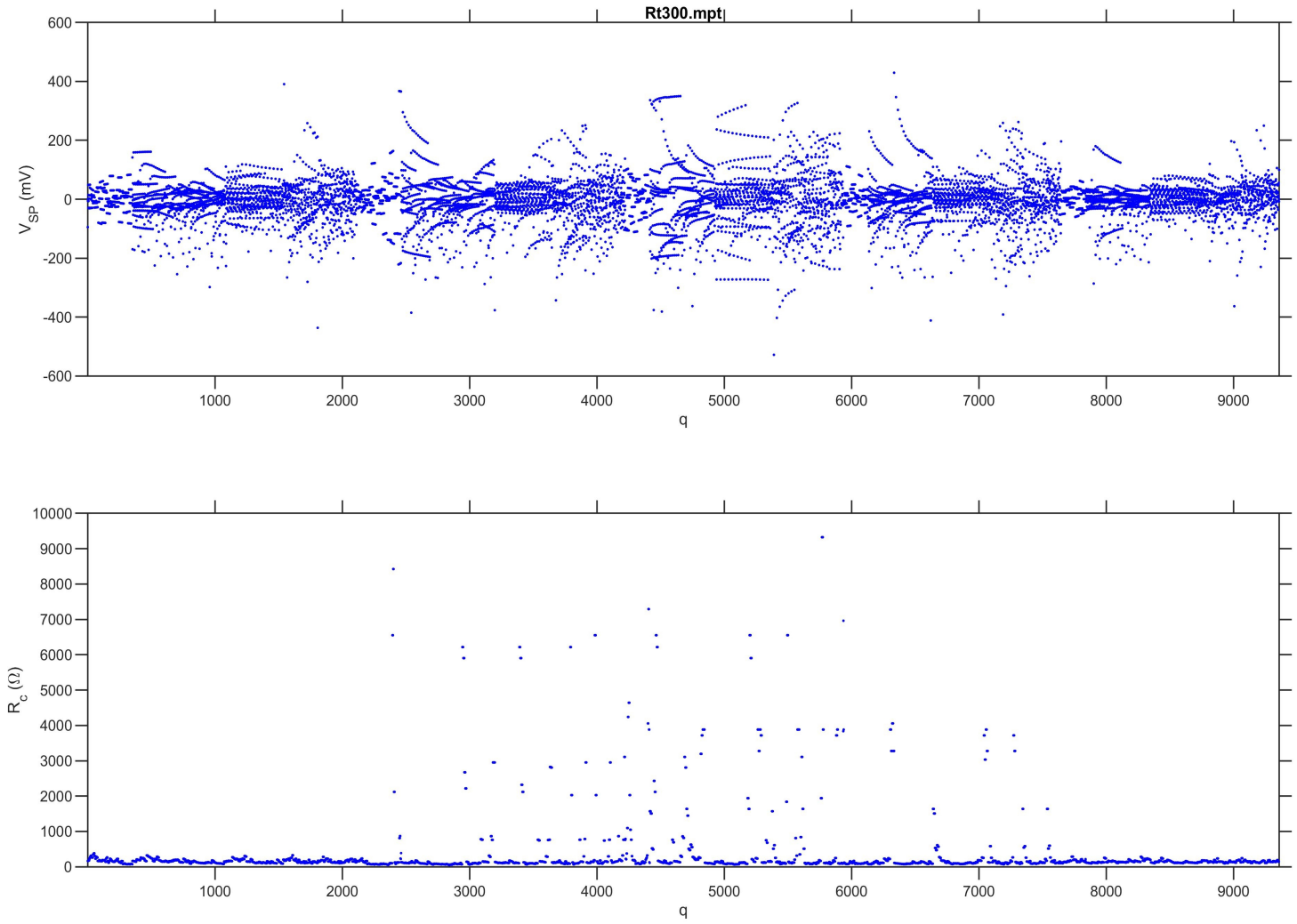

Figure B4. Spontaneous potential and contact resistance for each quadrupole measurement *q*.

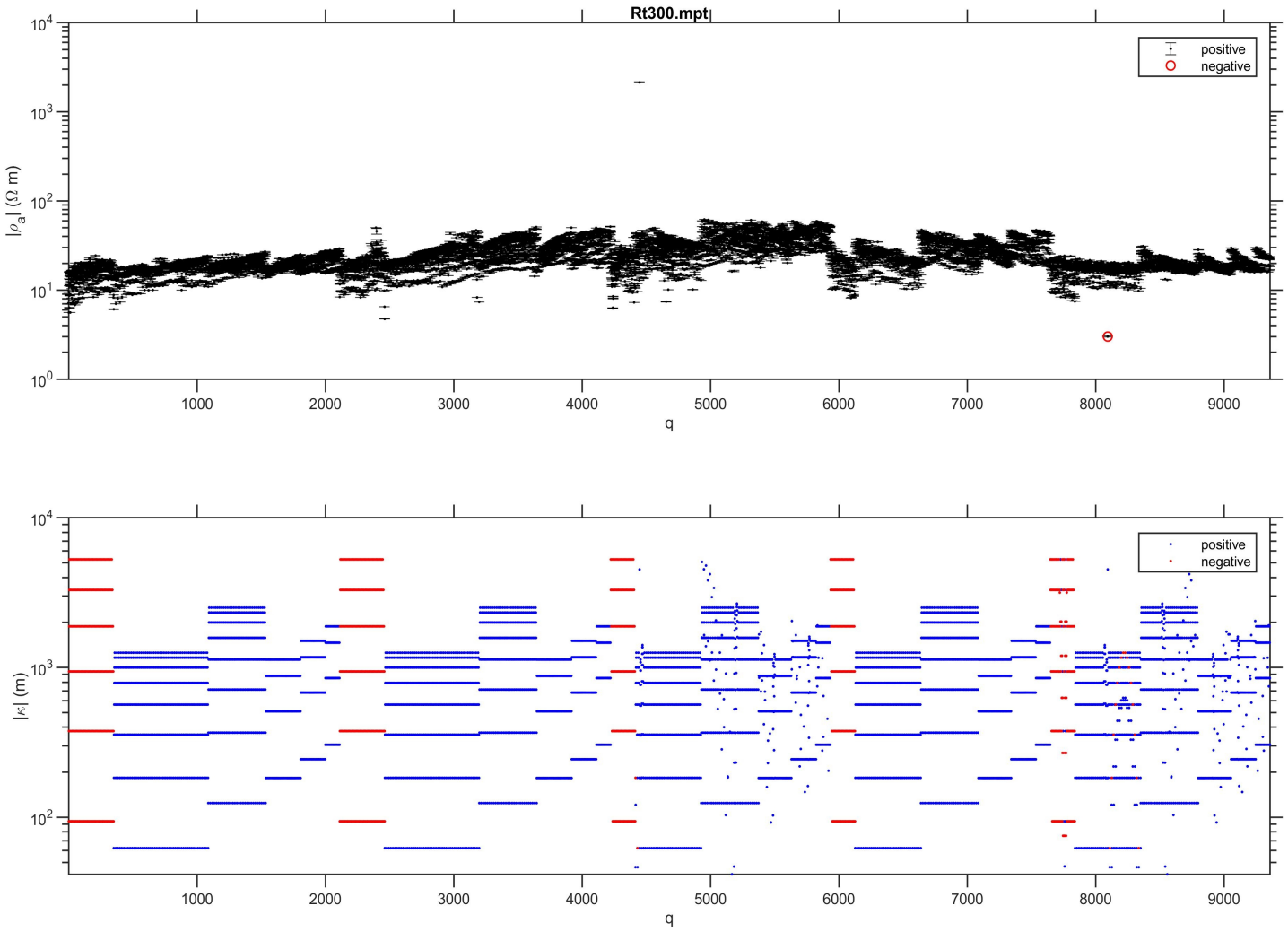

Figure B5. Apparent resistivity and geometric factor for each quadrupole measurement q. Negative values are depicted in red on the logarithmic scales.

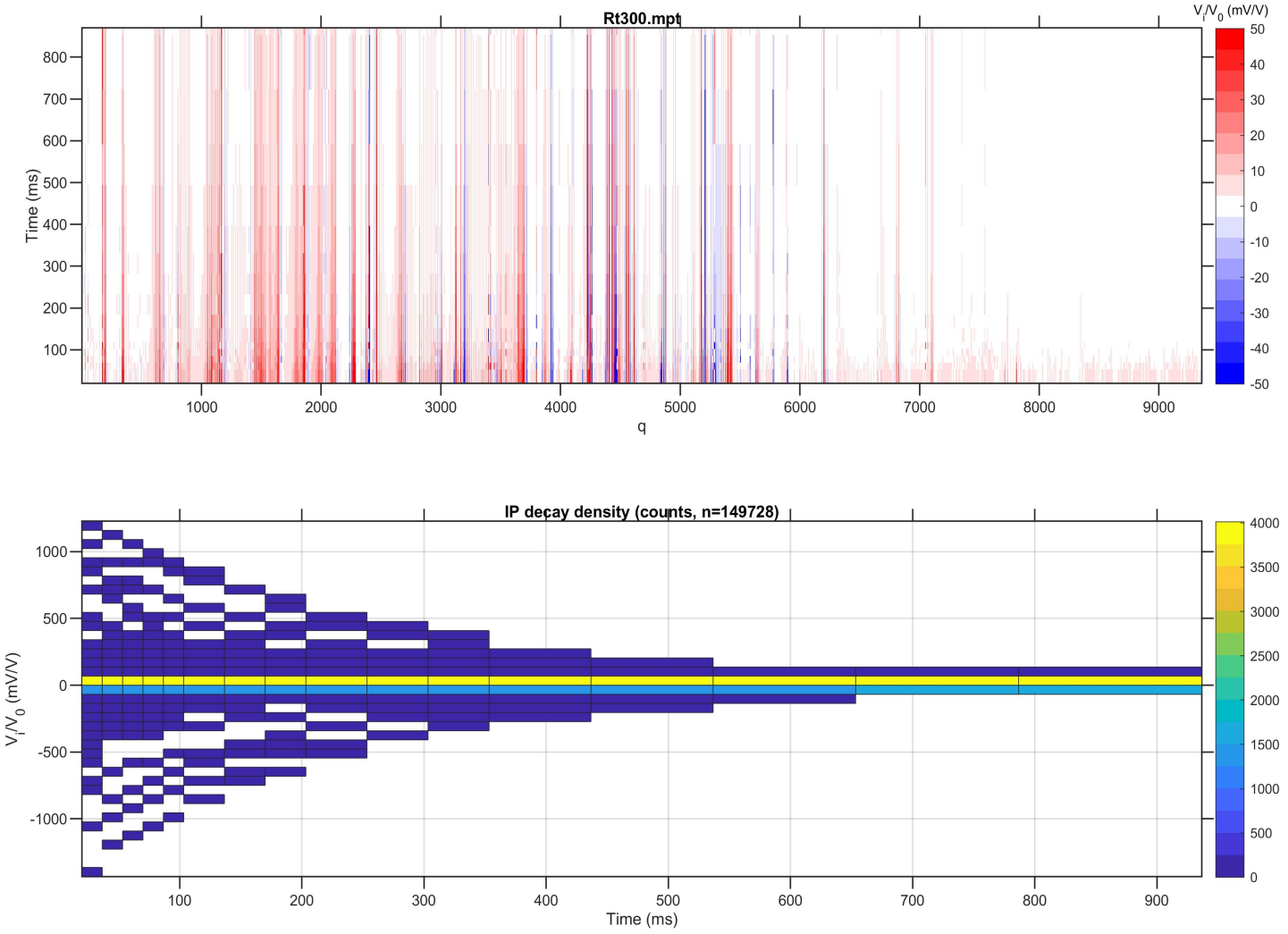

Figure B6. Voltage decays for each quadrupole measurement *q*, and decay distribution density as a function of time.

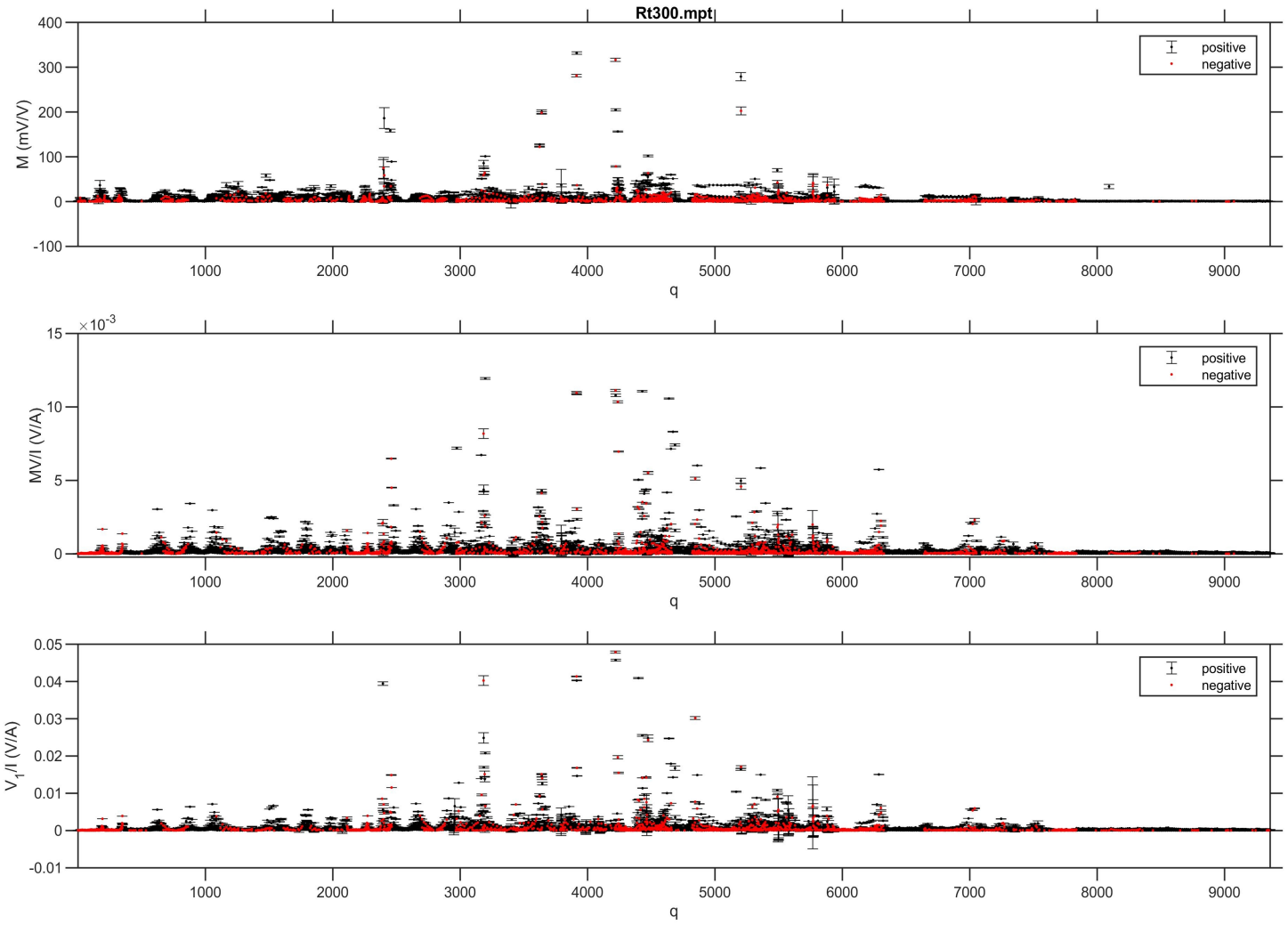

Figure B7. Chargeability and secondary voltage measured as the time-average voltage and the first window voltage (normalized by current) for each quadrupole measurement *q*. Negative values are depicted in red.

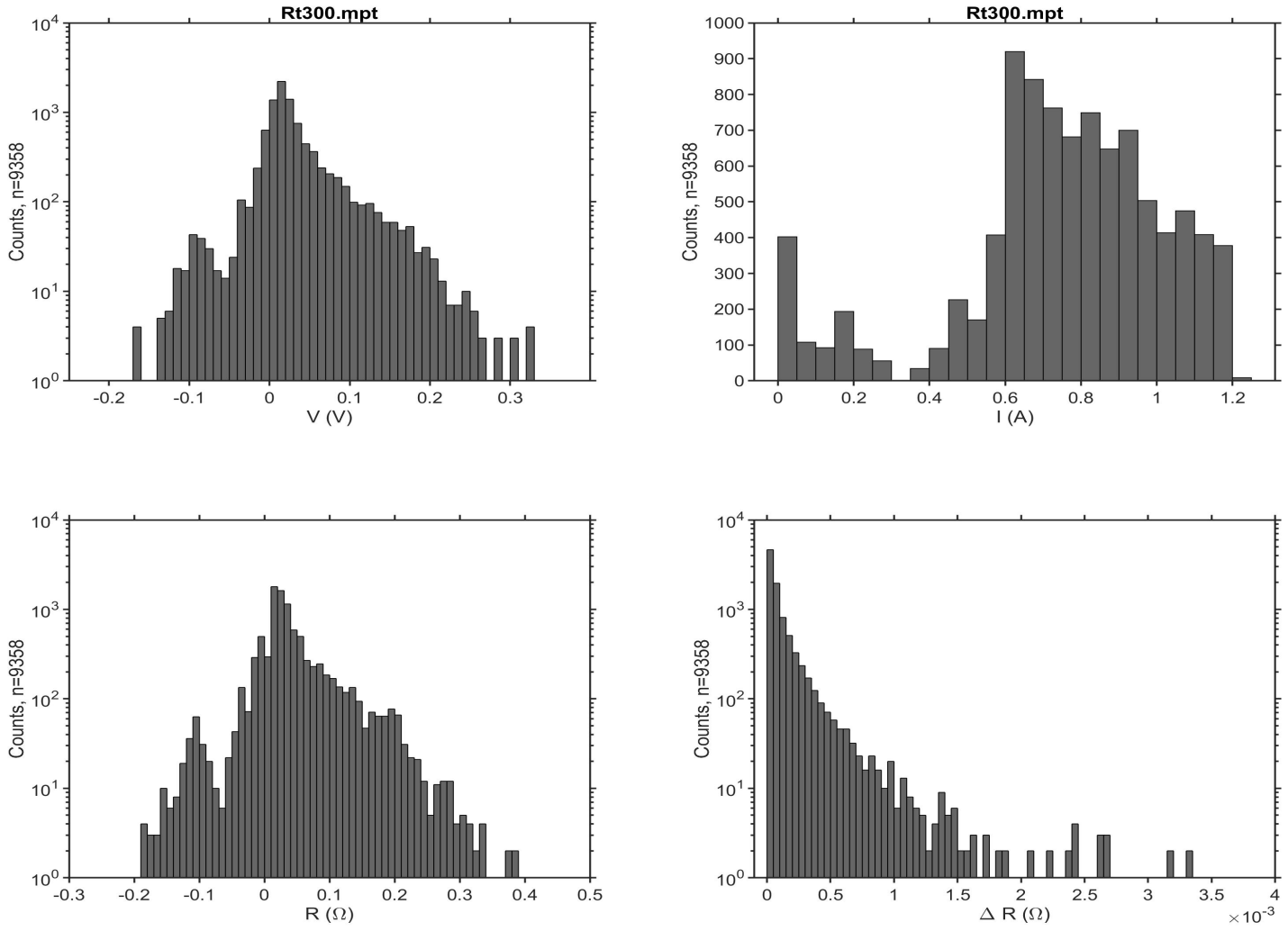

Figure B8. Distributions of voltage, current, and transfer resistance. Note the logarithmic scales required to depict outliers.

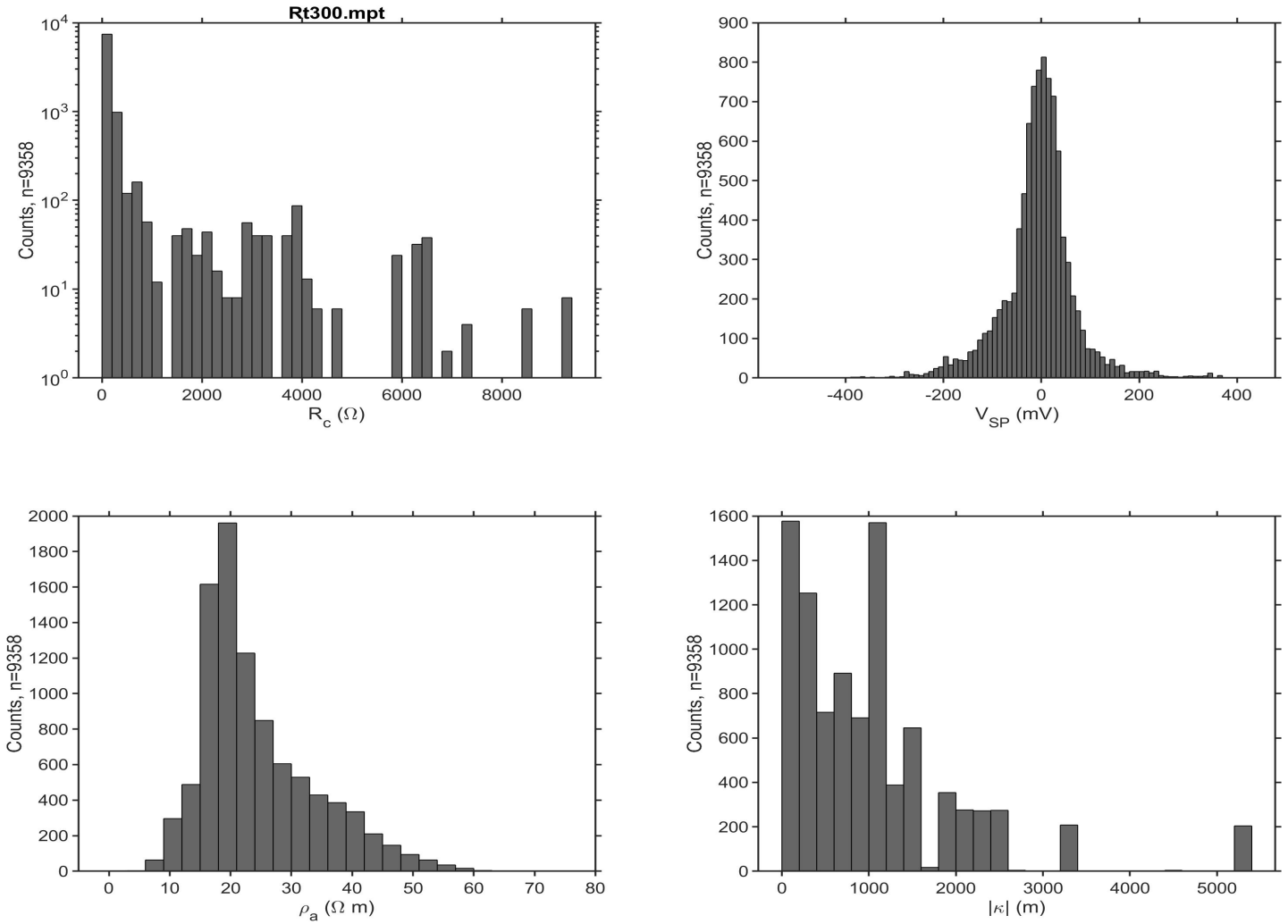

Figure B9. Distributions of contact resistance, spontaneous potential, apparent resistivity, and geometric factor. Note the logarithmic scales required to depict outliers.

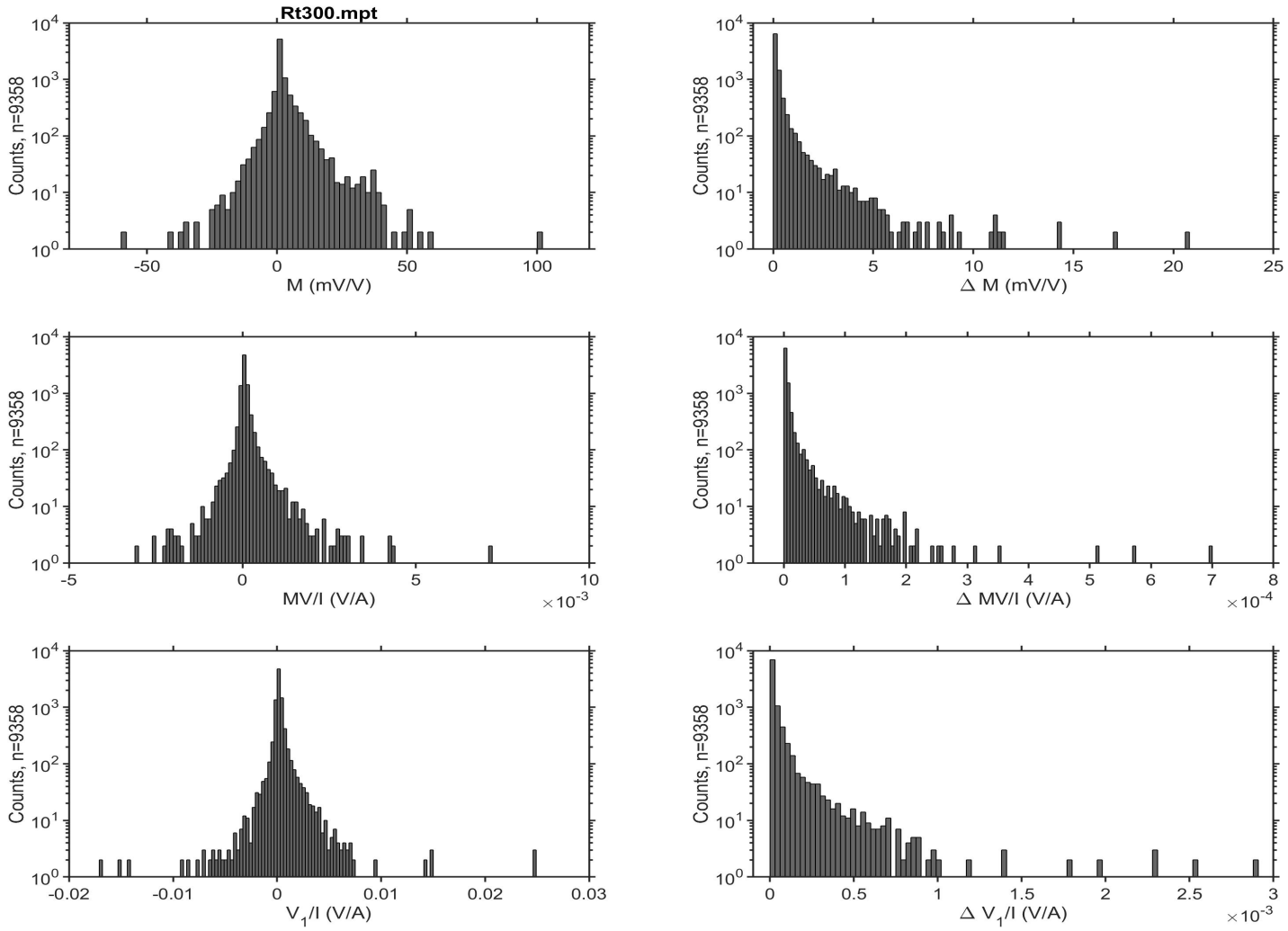

Figure B10. Distributions of chargeability, time-average voltage, and first window voltage. Note the logarithmic scales required to depict outliers.

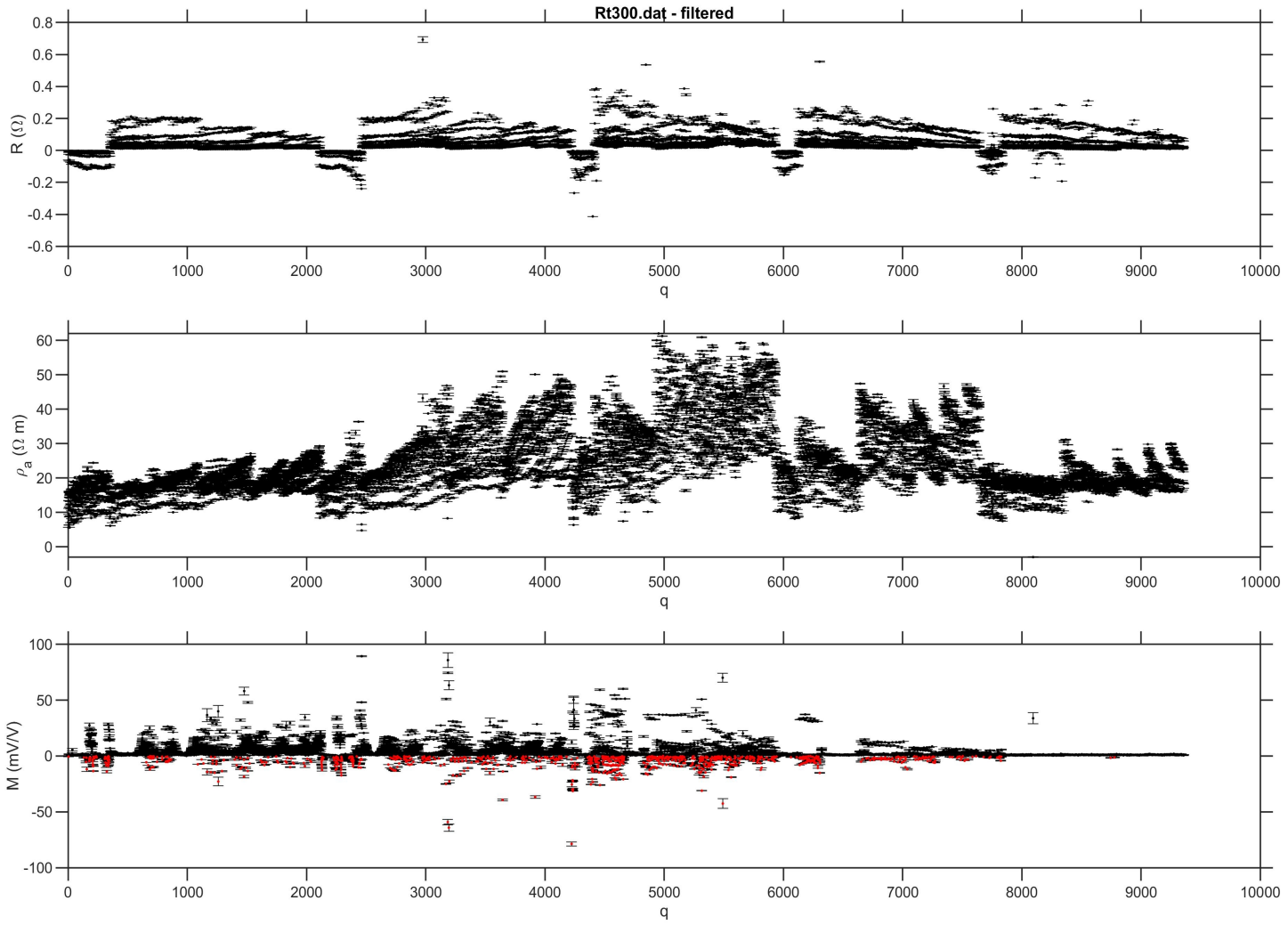

Figure B11. Filtered transfer resistance, apparent resistivity, and chargeability for each quadrupole measurement *q*. Negative chargeabilities are depicted in red.

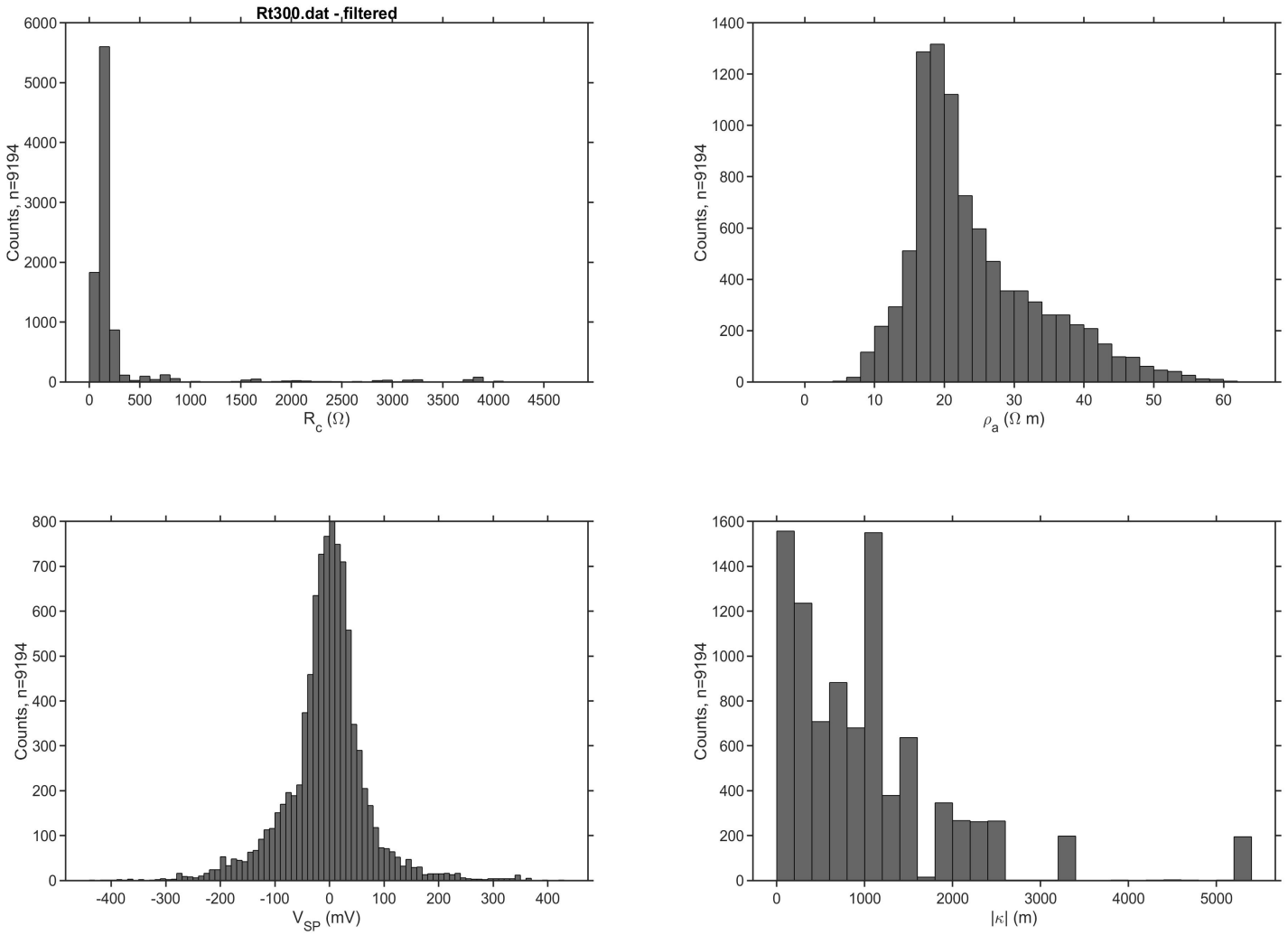

Figure B12. Filtered distributions of contact resistance, spontaneous potential, apparent resistivity, and geometric factor.

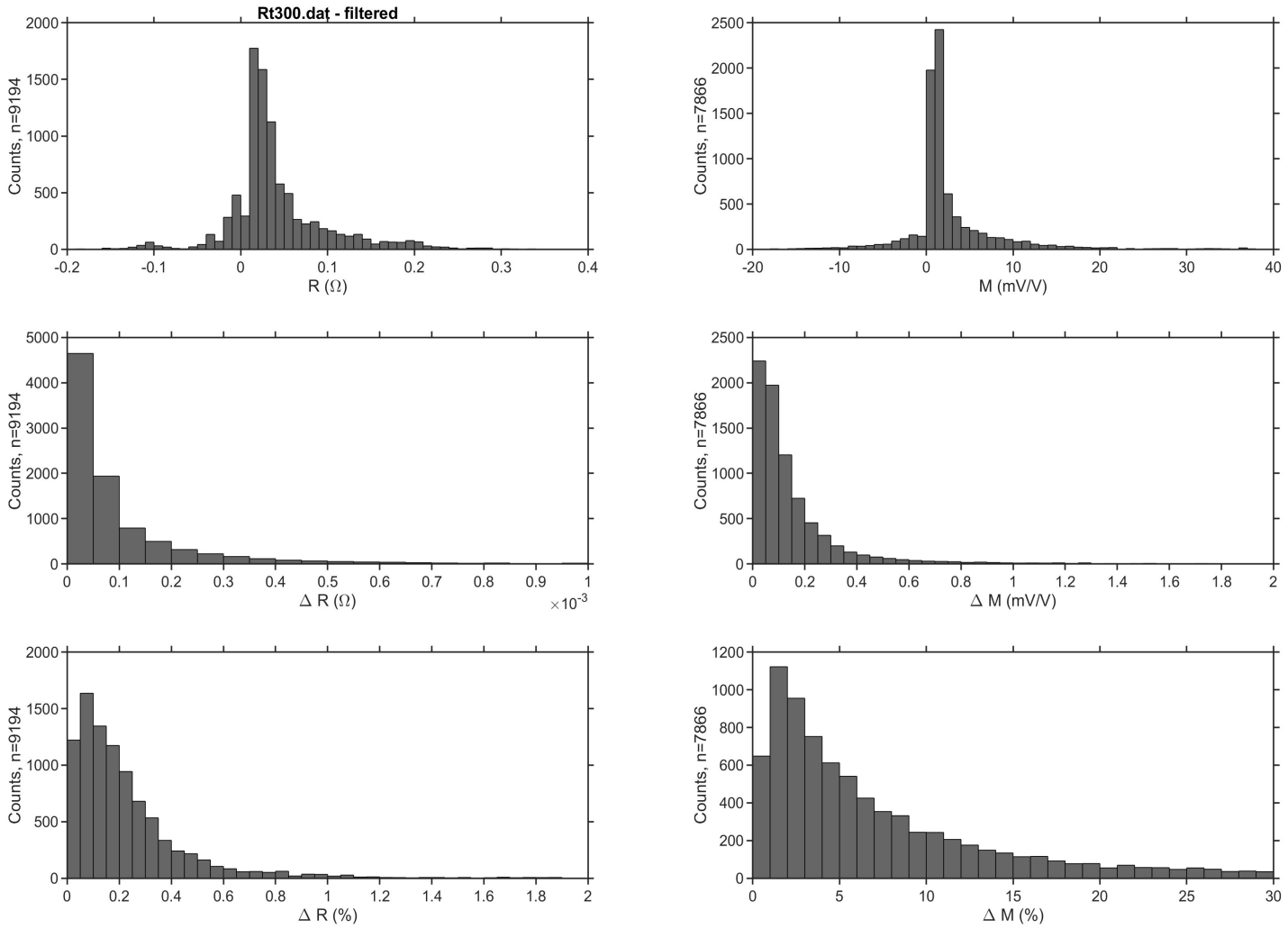

Figure B13. Filtered distributions of transfer resistance and chargeability.

APPENDIX C

Example data and data processing steps for the **GSC-SN2-17-1** surface-to-borehole acquisition (Figure 1). Figures show the measured data, the measurement errors, the results of filtering, and the apparent resistivity logs. See the full report and Appendix A for details.

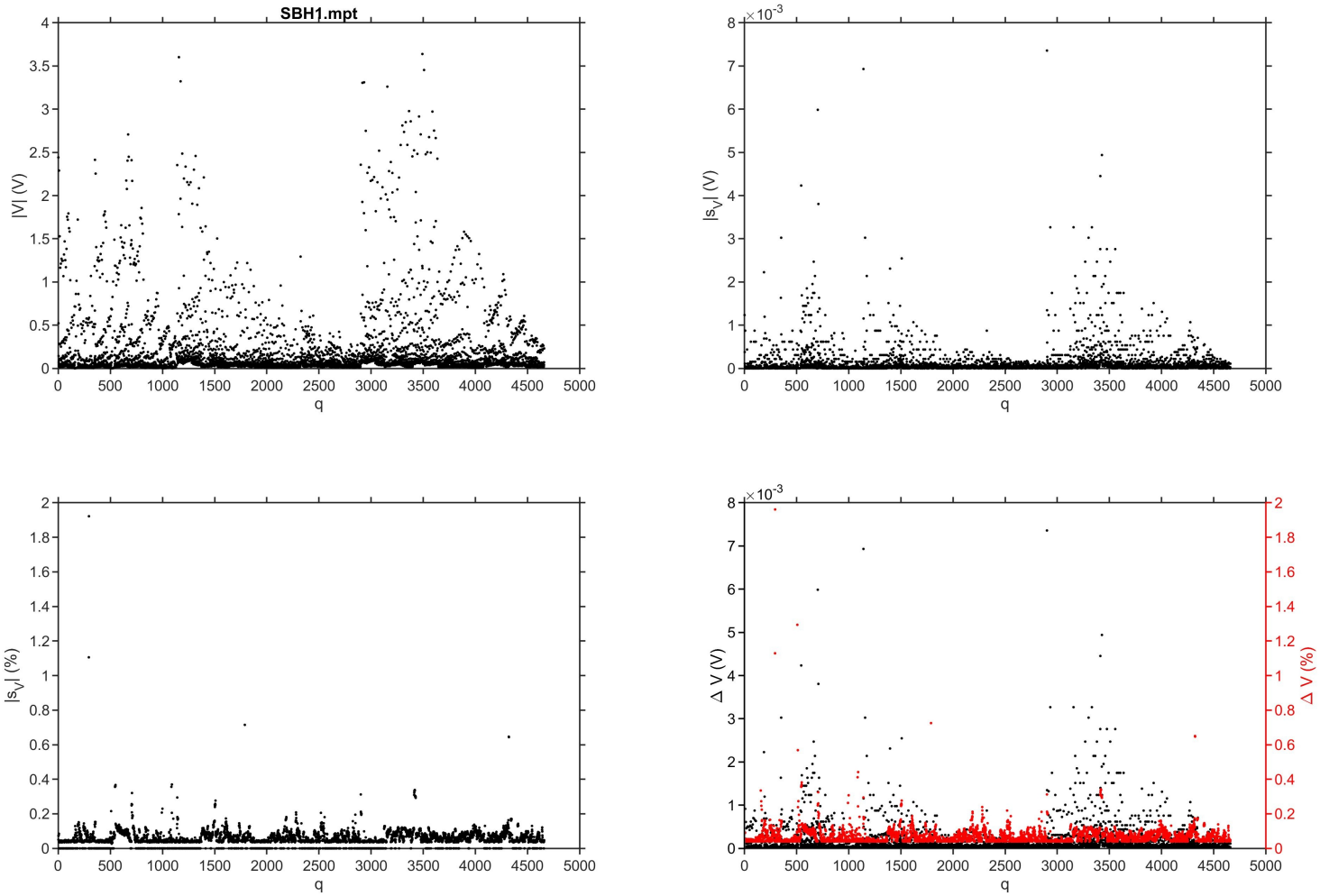

Figure C1. Voltage measurements and measurement error for each quadrupole measurement *q*.

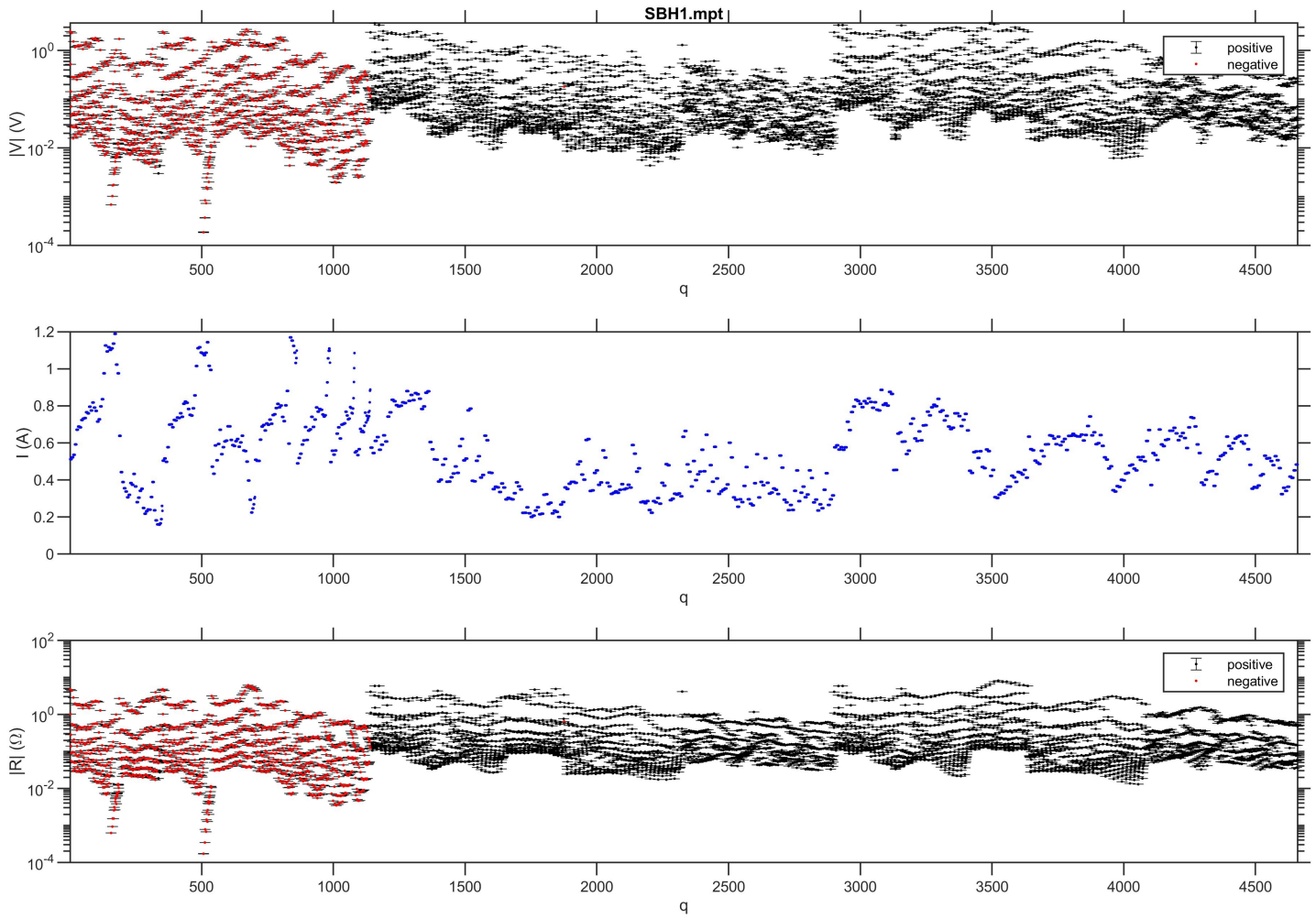

Figure C2. Voltage, current, and transfer resistance for each quadrupole measurement *q*. Negative values are depicted in red on the logarithmic scales.

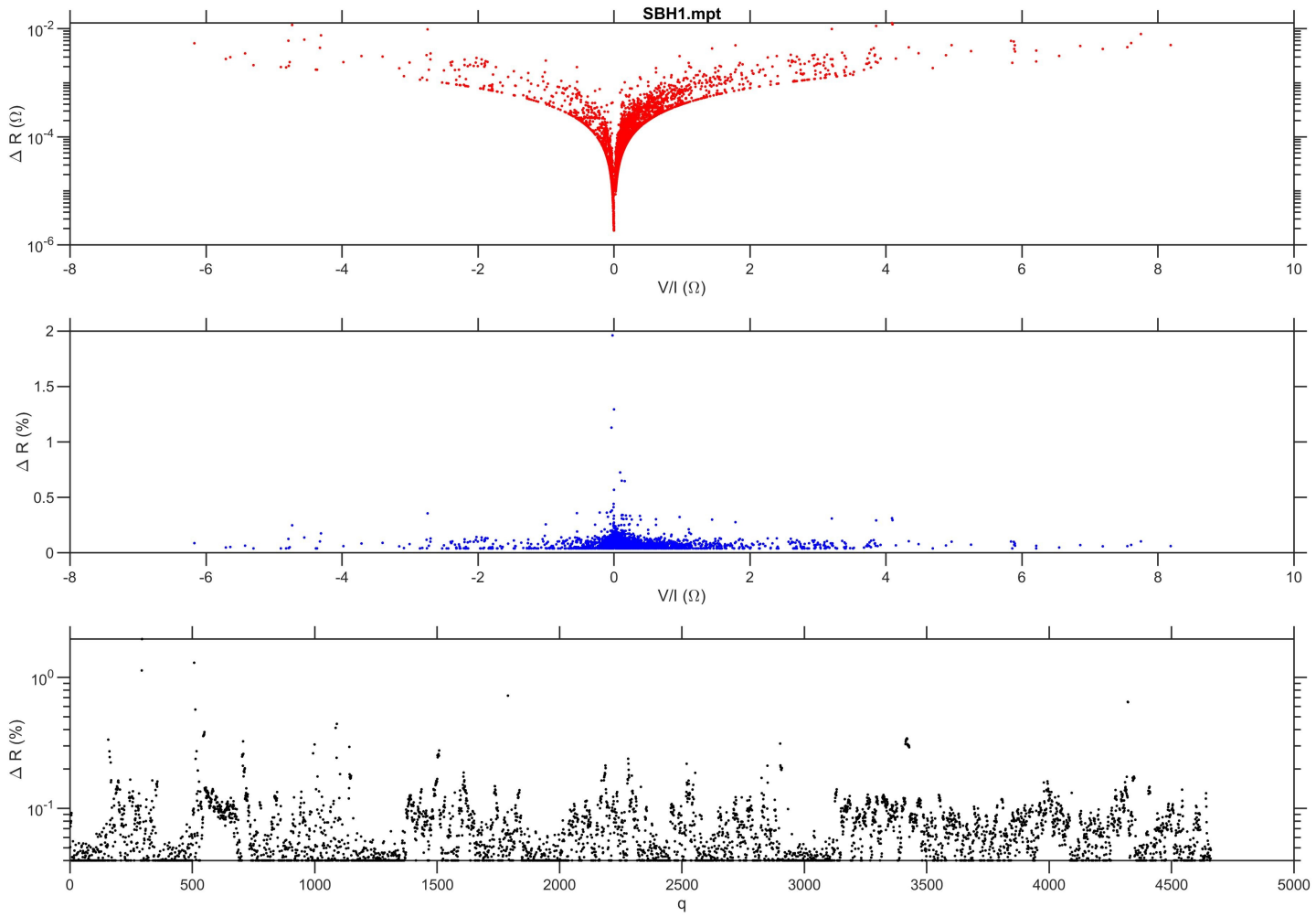

Figure C3. Transfer resistance measurement error as a function of transfer resistance, and for each quadrupole measurement *q*.

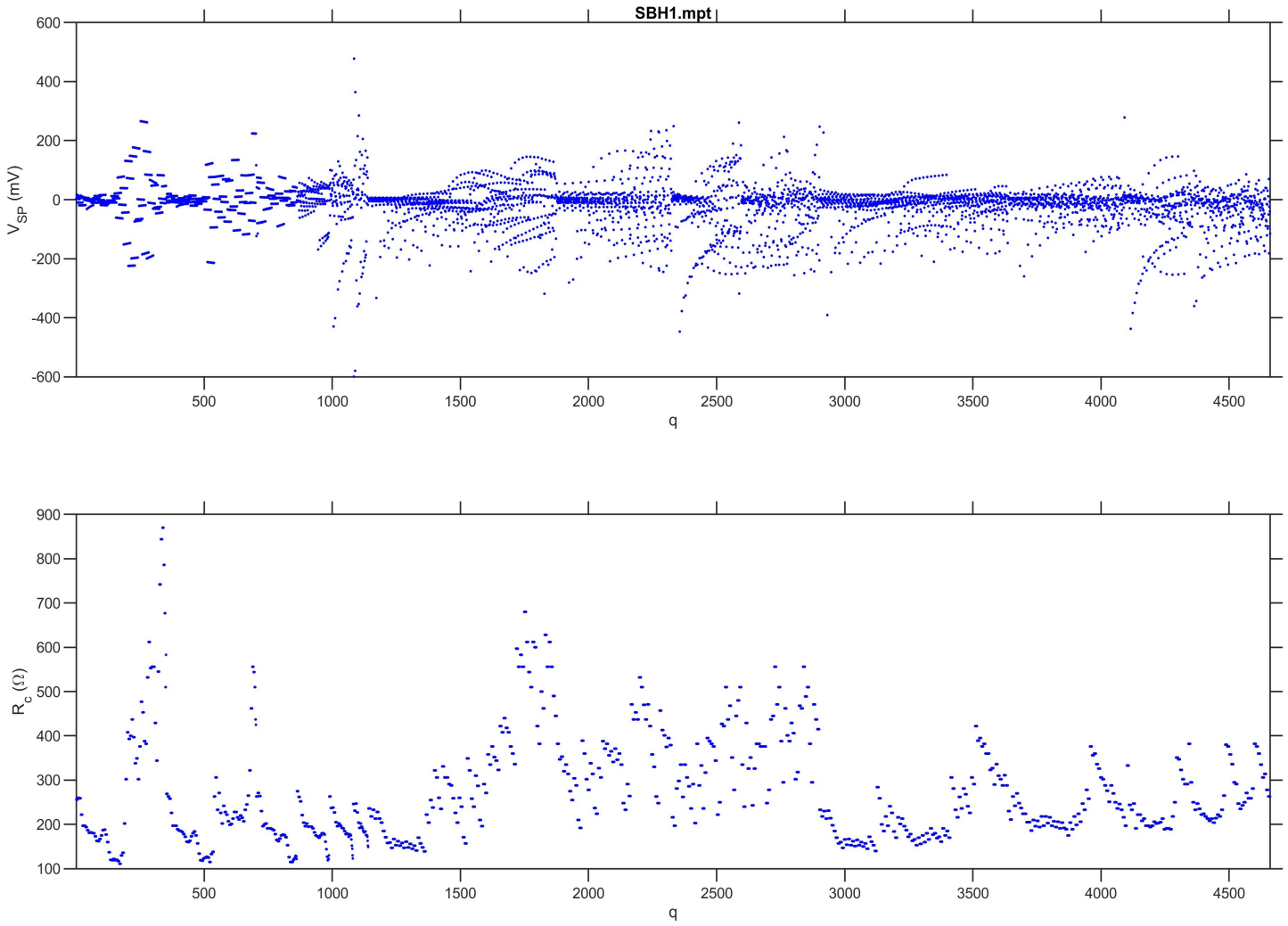

Figure C4. Spontaneous potential and contact resistance for each quadrupole measurement *q*.

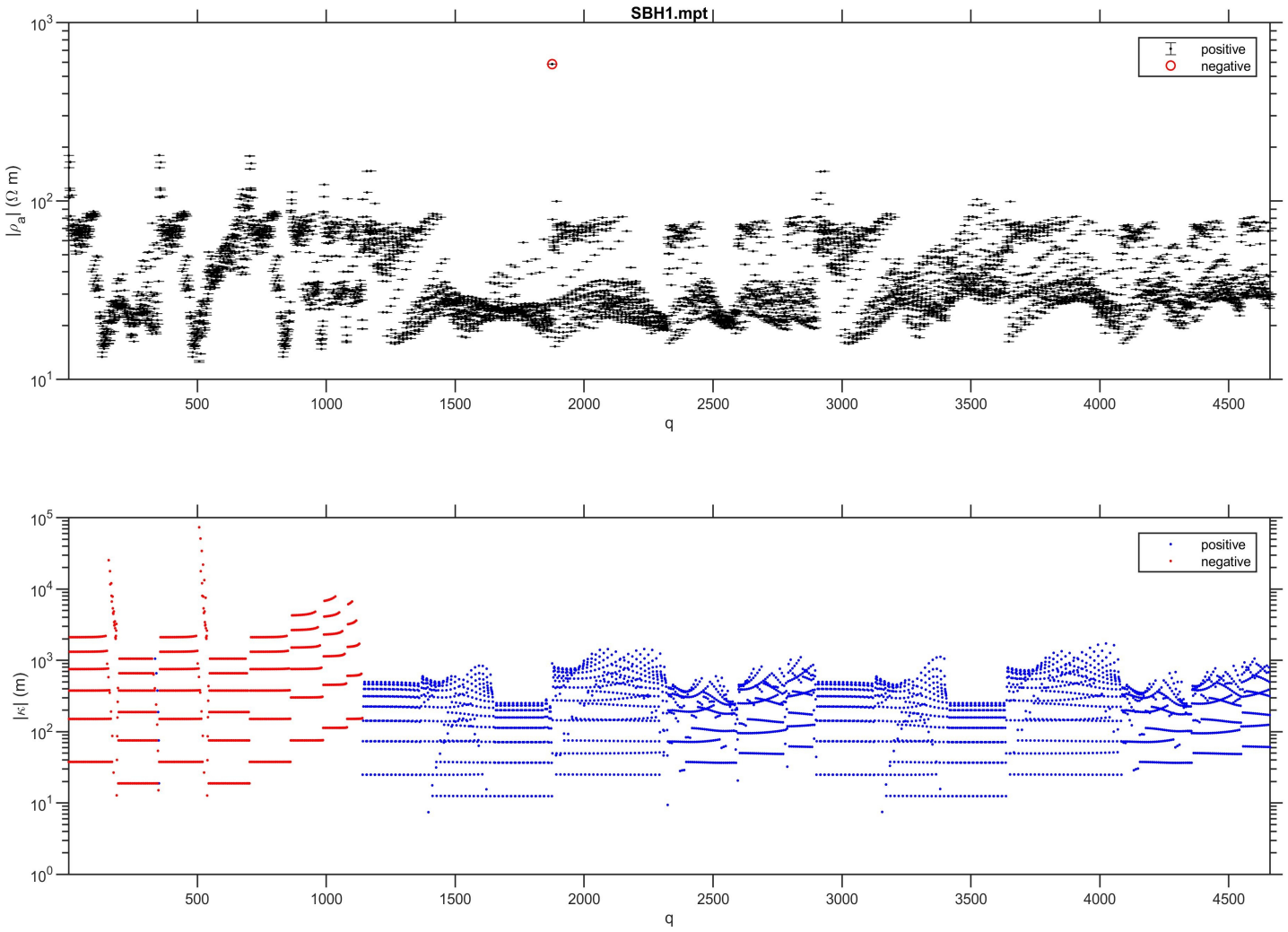

Figure C5. Apparent resistivity and geometric factor for each quadrupole measurement *q*. Negative values are depicted in red on the logarithmic scales.

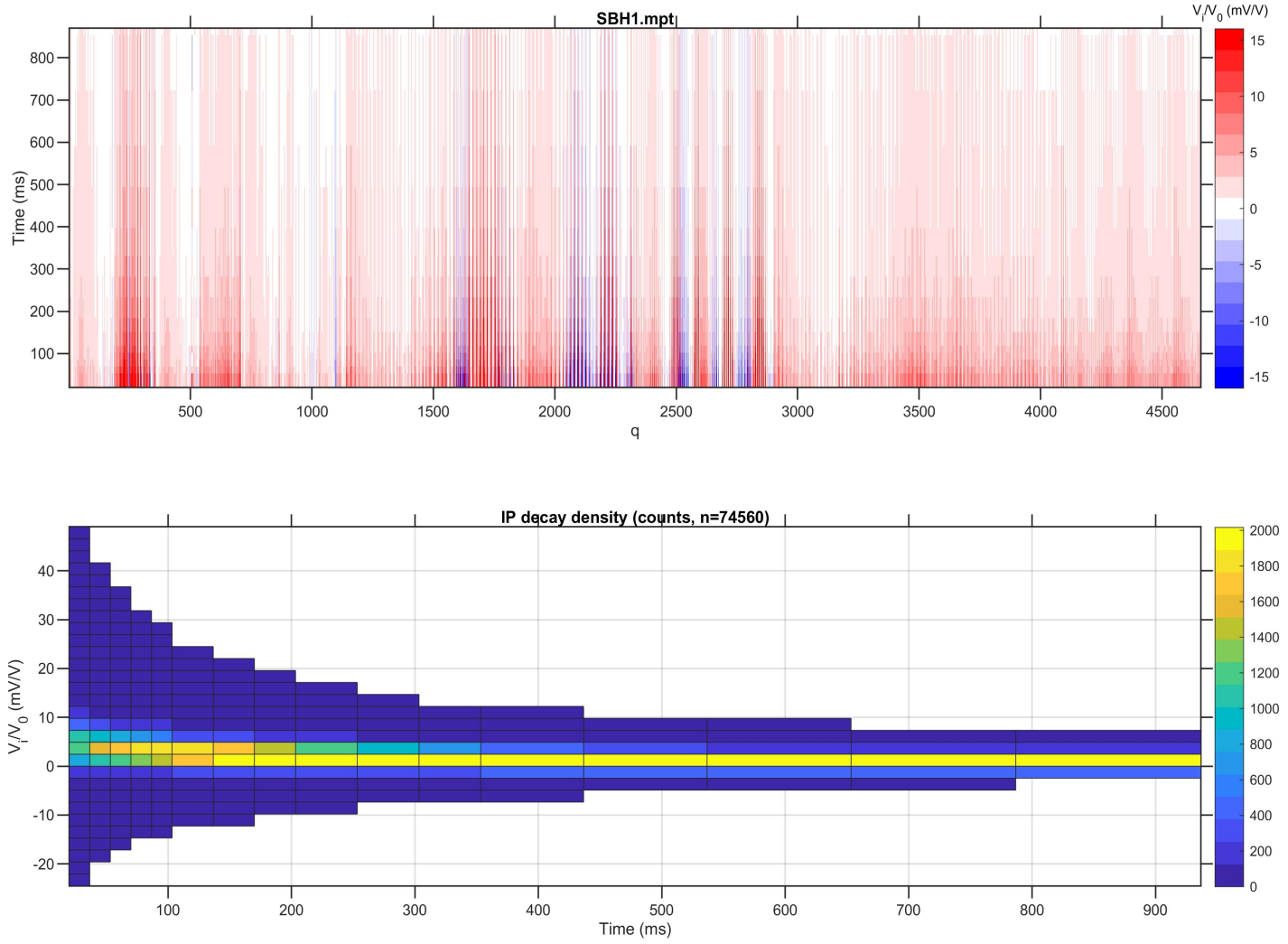

Figure C6. Voltage decays for each quadrupole measurement *q*, and decay distribution density as a function of time.

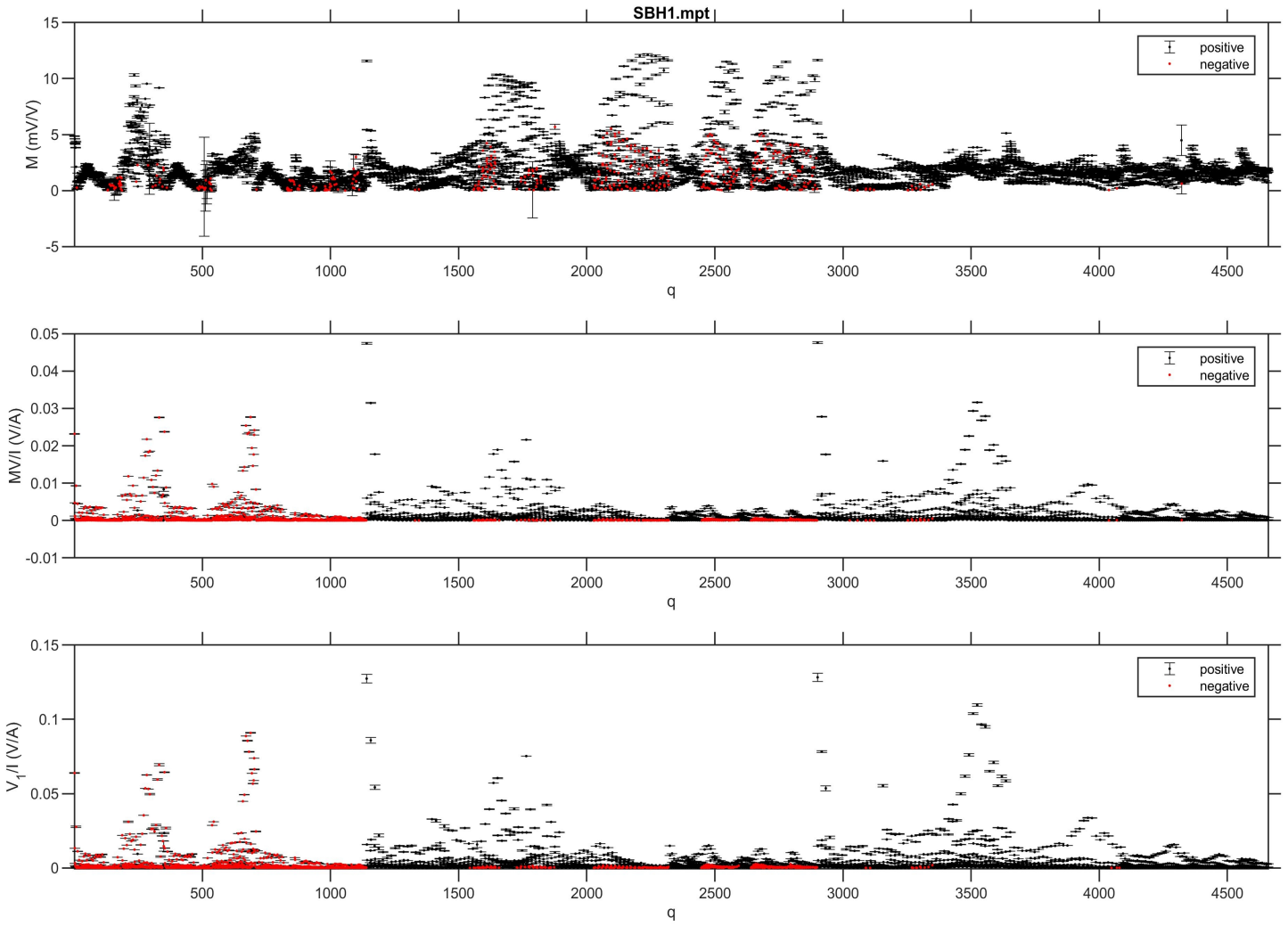

Figure C7. Chargeability and secondary voltage measured as the time-average voltage and the first window voltage (normalized by current) for each quadrupole measurement *q*. Negative values are depicted in red.

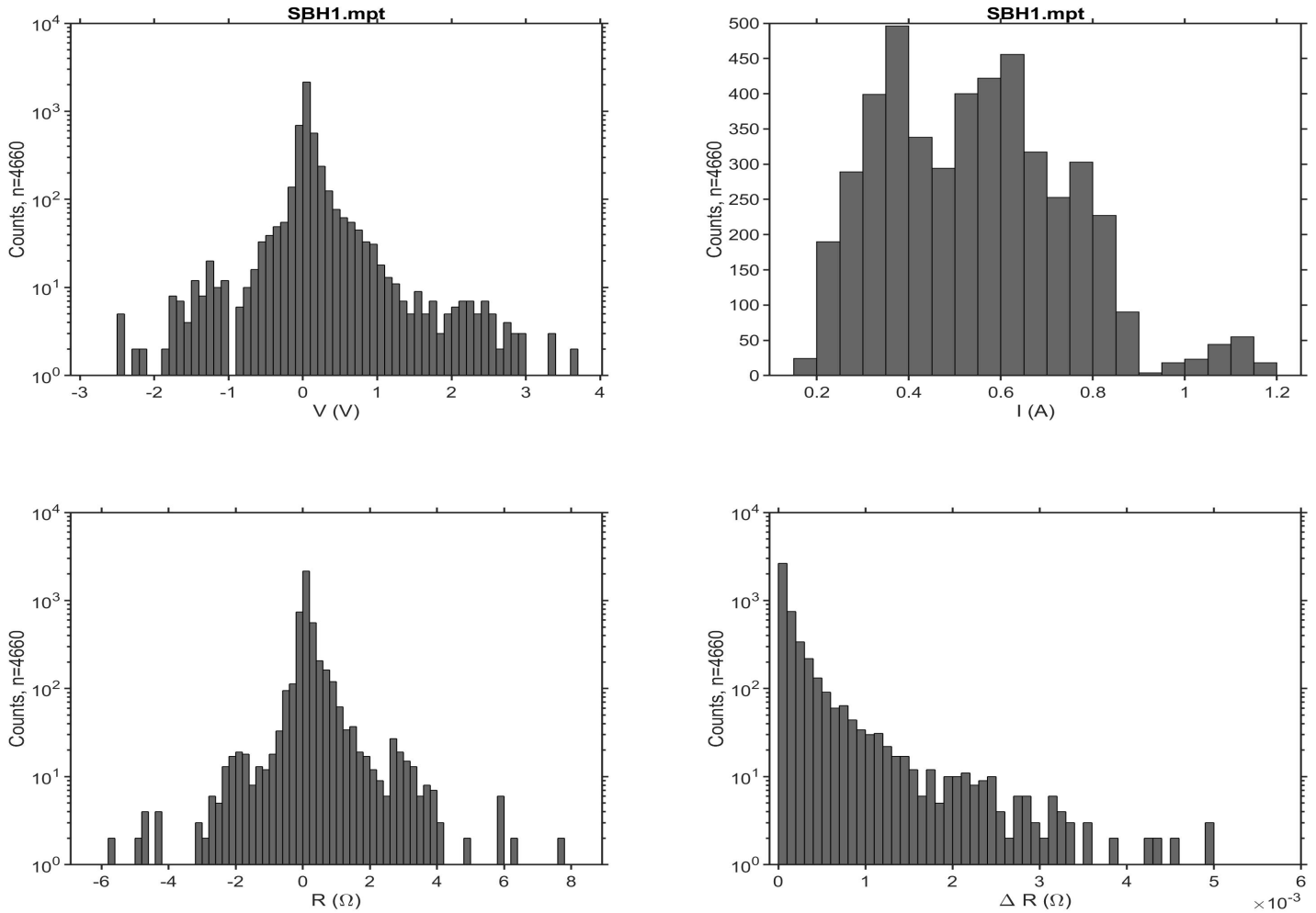

Figure C8. Distributions of voltage, current, and transfer resistance. Note the logarithmic scales required to depict outliers.

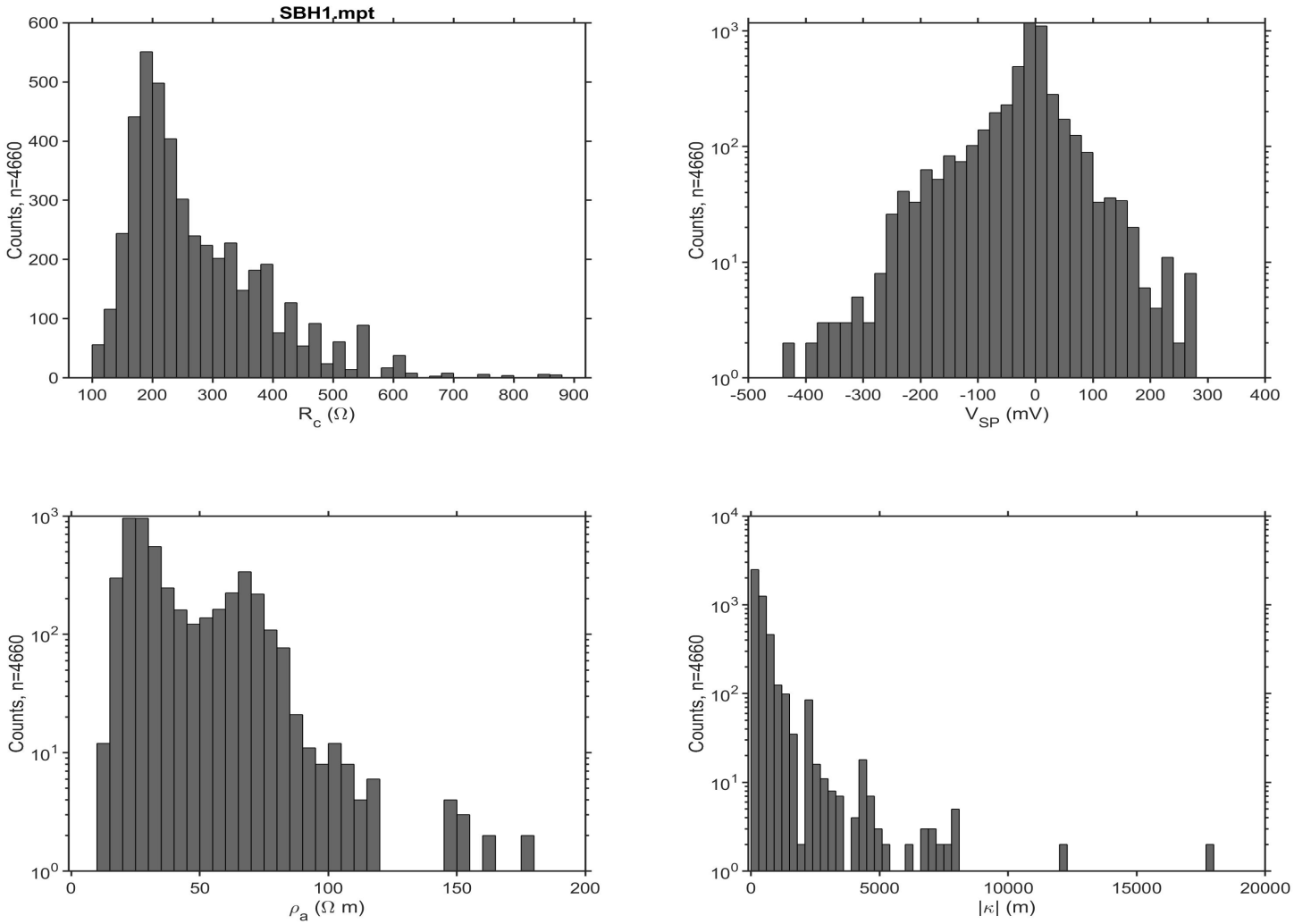

Figure C9. Distributions of contact resistance, spontaneous potential, apparent resistivity, and geometric factor. Note the logarithmic scales required to depict outliers.

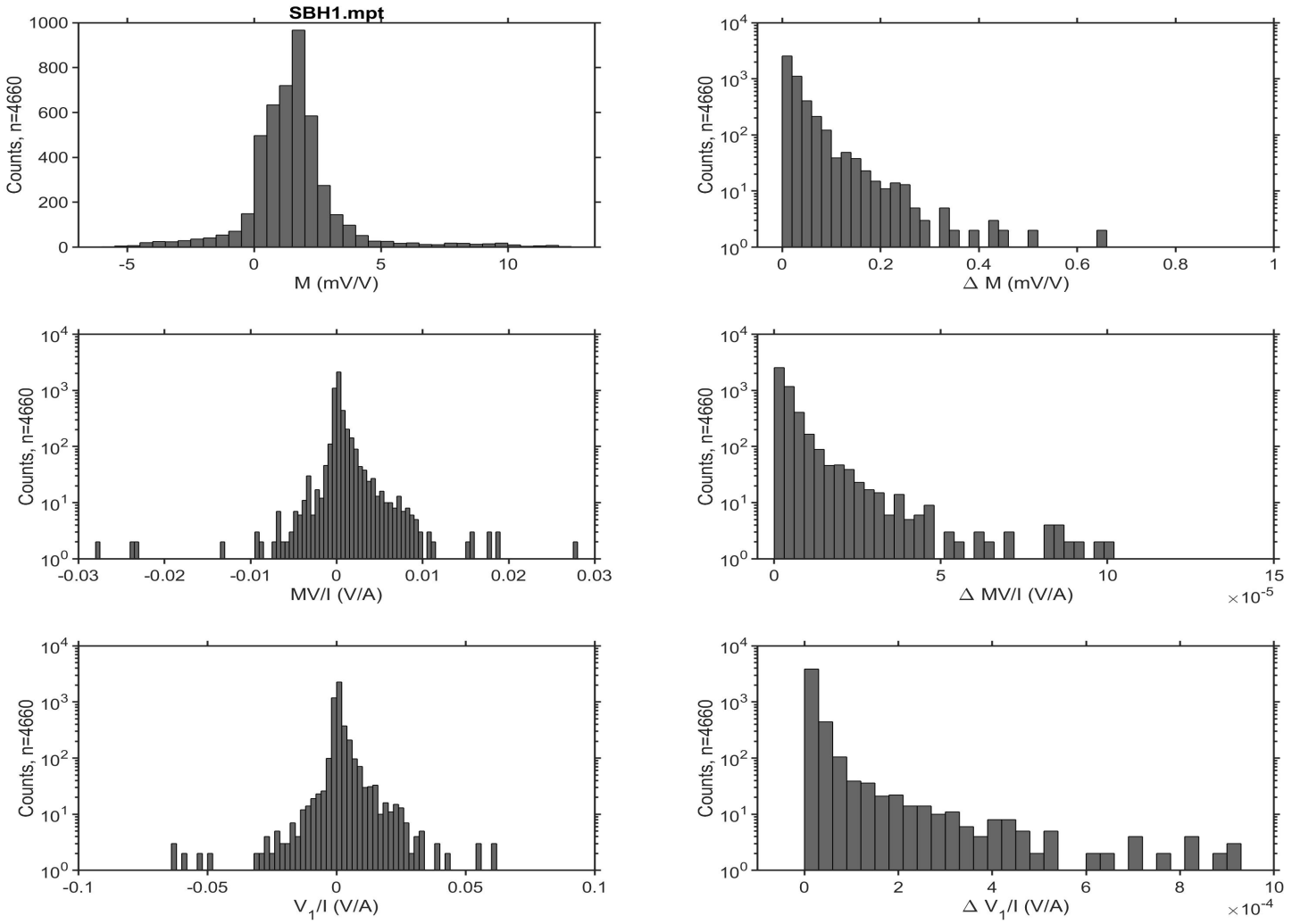

Figure C10. Distributions of chargeability, time-average voltage, and first window voltage. Note the logarithmic scales required to depict outliers.

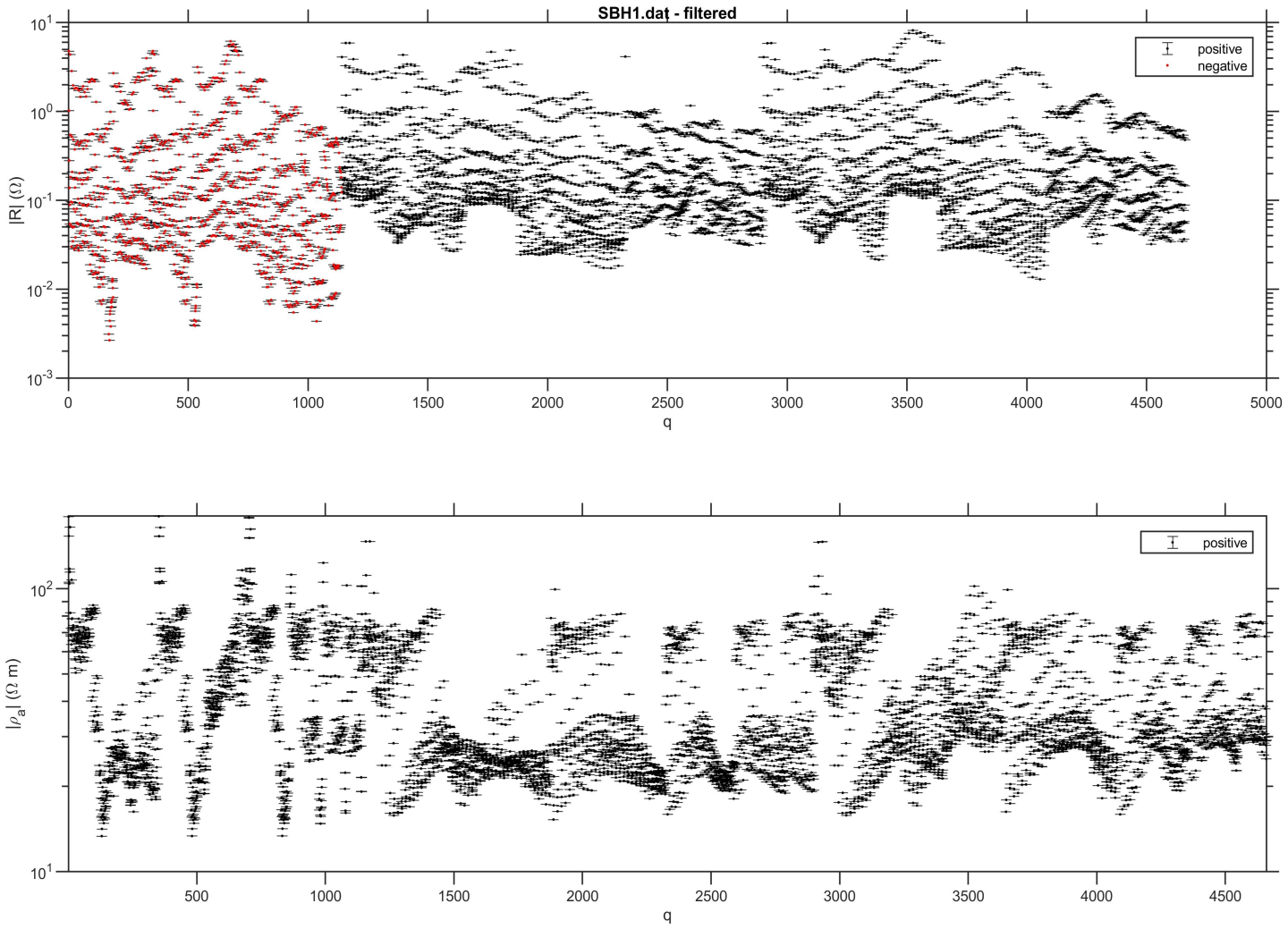

Figure C11. Filtered transfer resistance and apparent resistivity for each quadrupole measurement *q*. Negative values are depicted in red on the logarithmic scales.

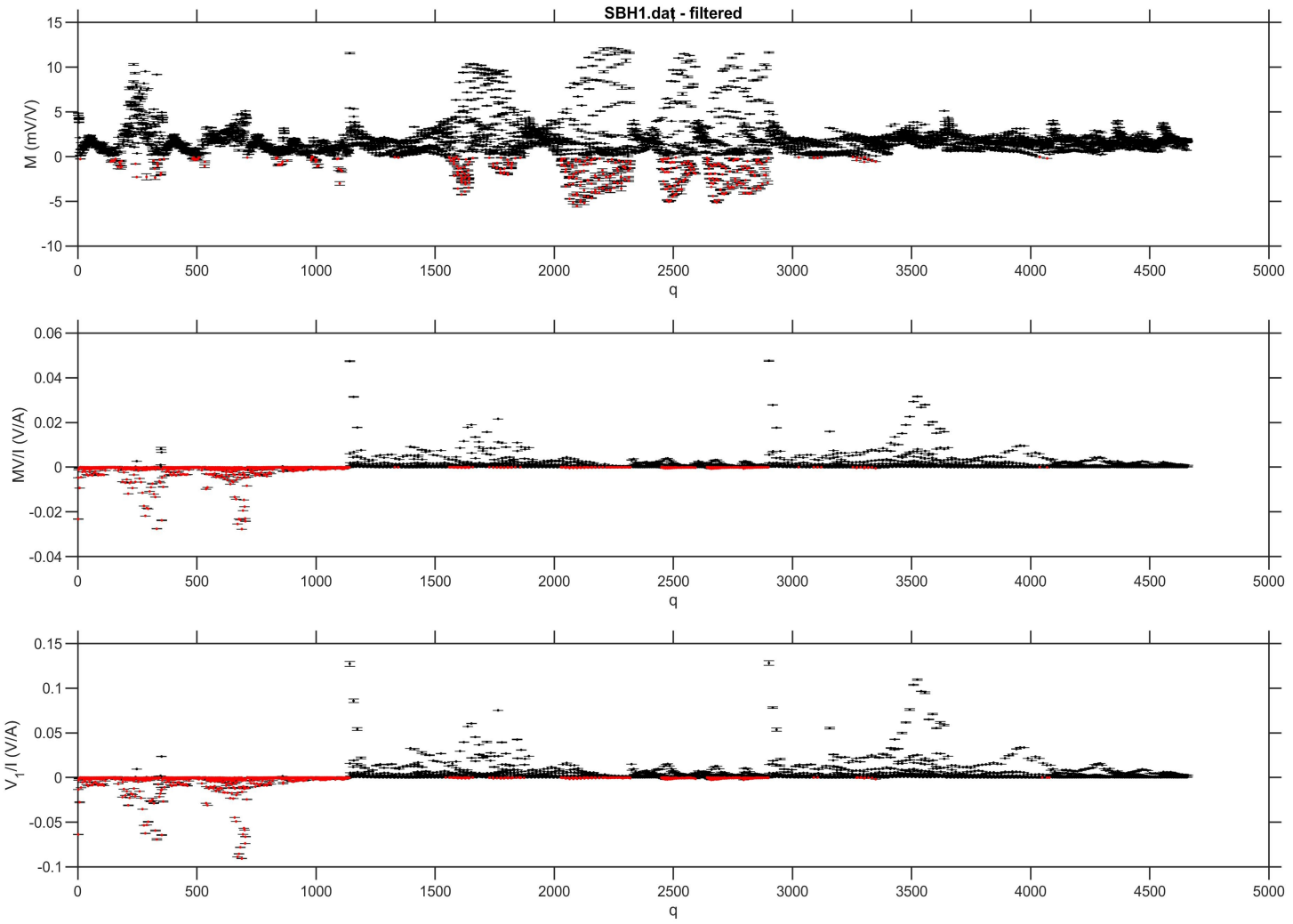

Figure C12. Filtered chargeability, time-average voltage, and first window voltage for each quadrupole measurement *q*. Negative values are depicted in red.

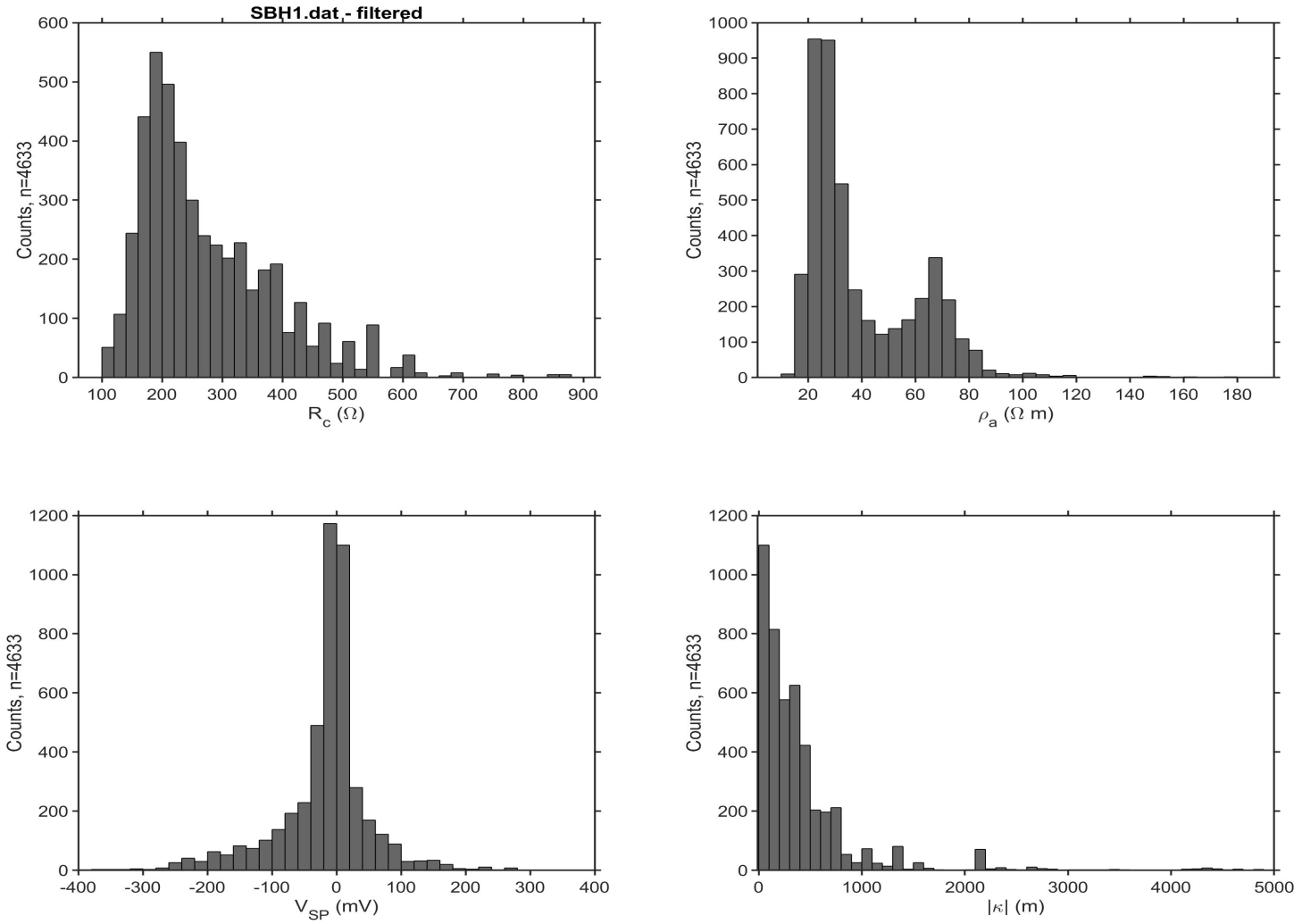

Figure C13. Filtered distributions of contact resistance, spontaneous potential, apparent resistivity, and geometric factor.

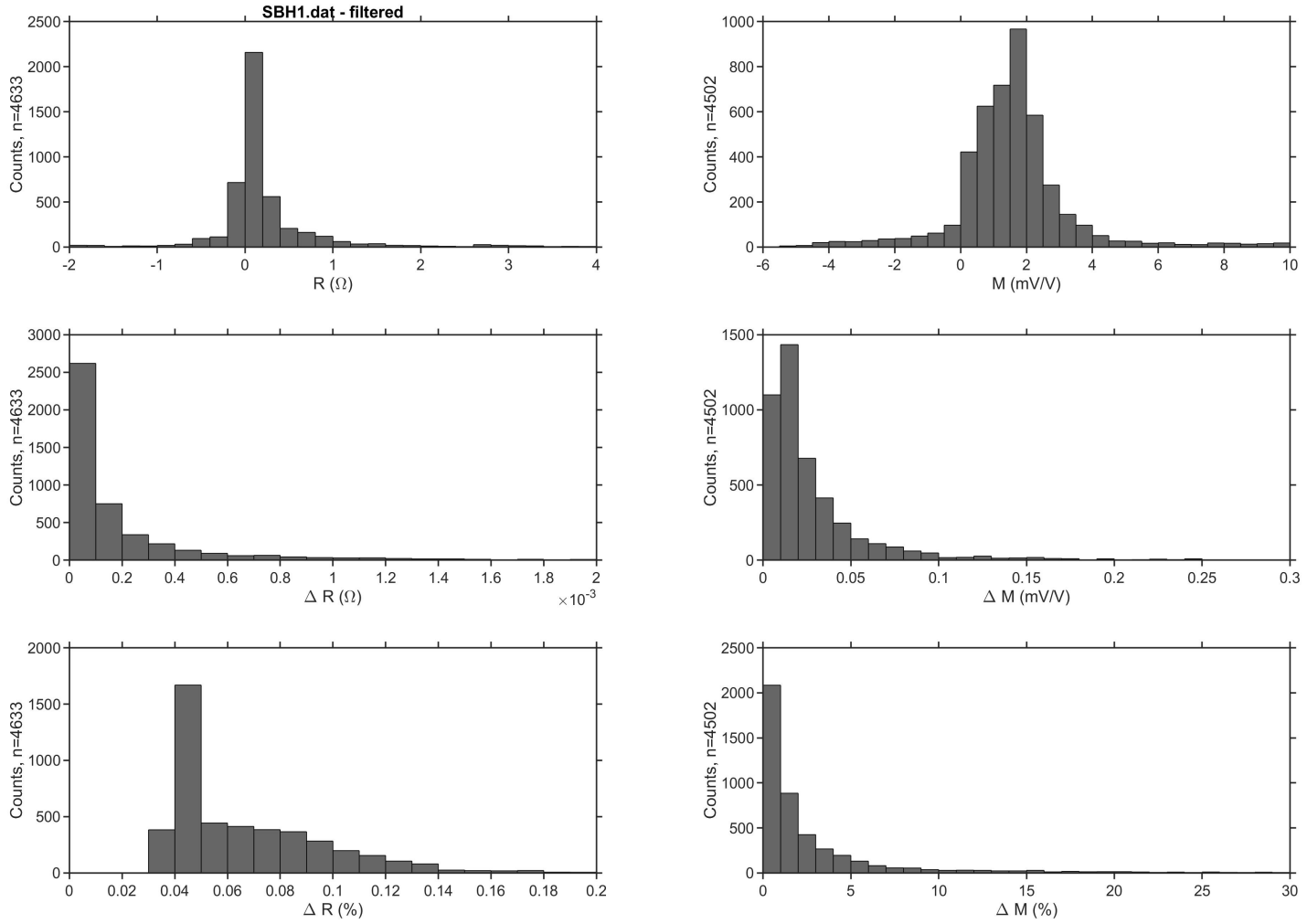

Figure C14. Filtered distributions of transfer resistance and chargeability.

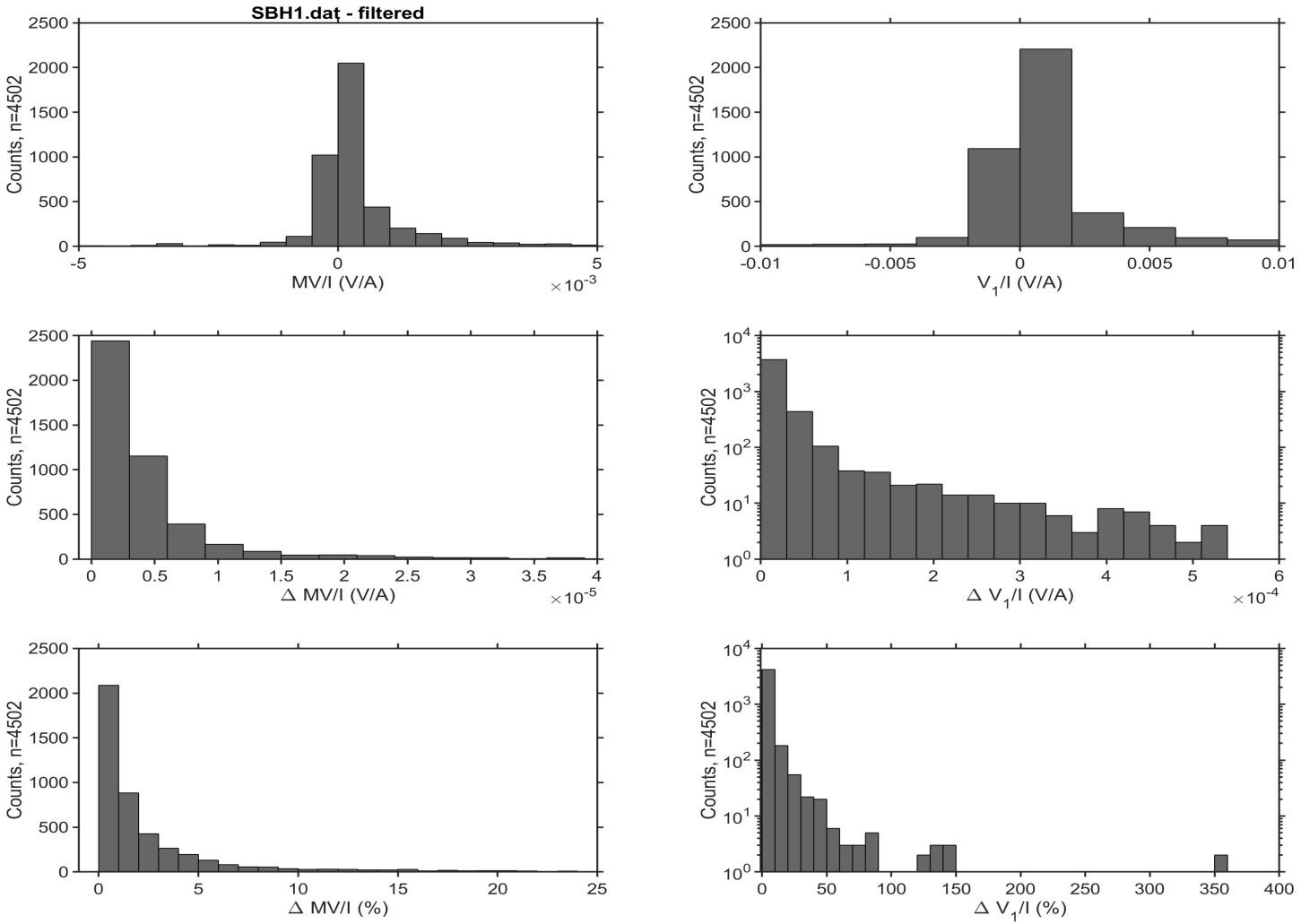

Figure C15. Filtered distributions of time-averaged decay voltage, and first window voltage. Note the logarithmic scales required to depict outliers for first window voltage, which is unstable even after filtering.

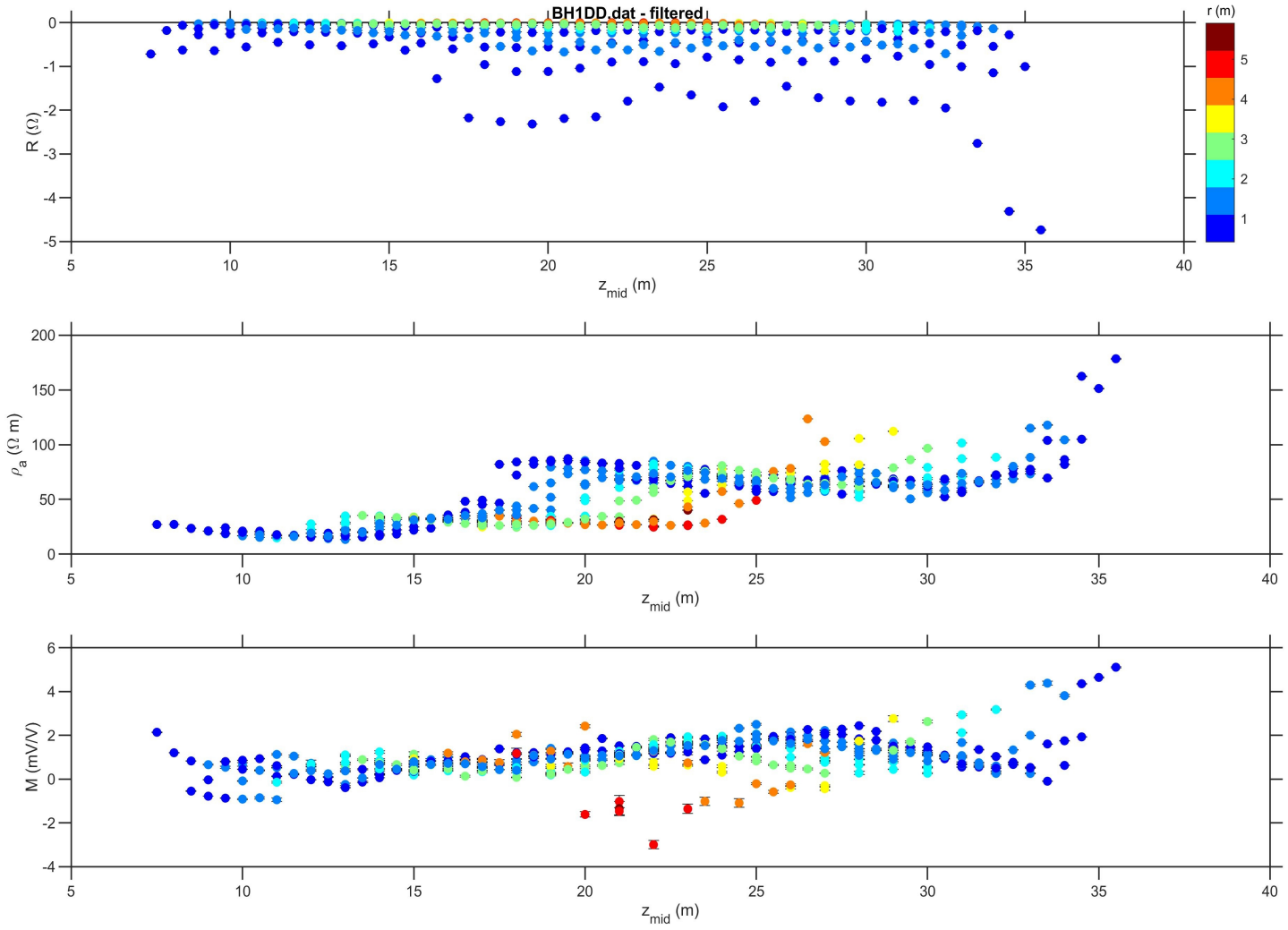

Figure C16. Filtered borehole dipole-dipole resistance, apparent resistivity, and apparent chargeability logs as a function of mid-point depth and approximate radius of investigation *r*.

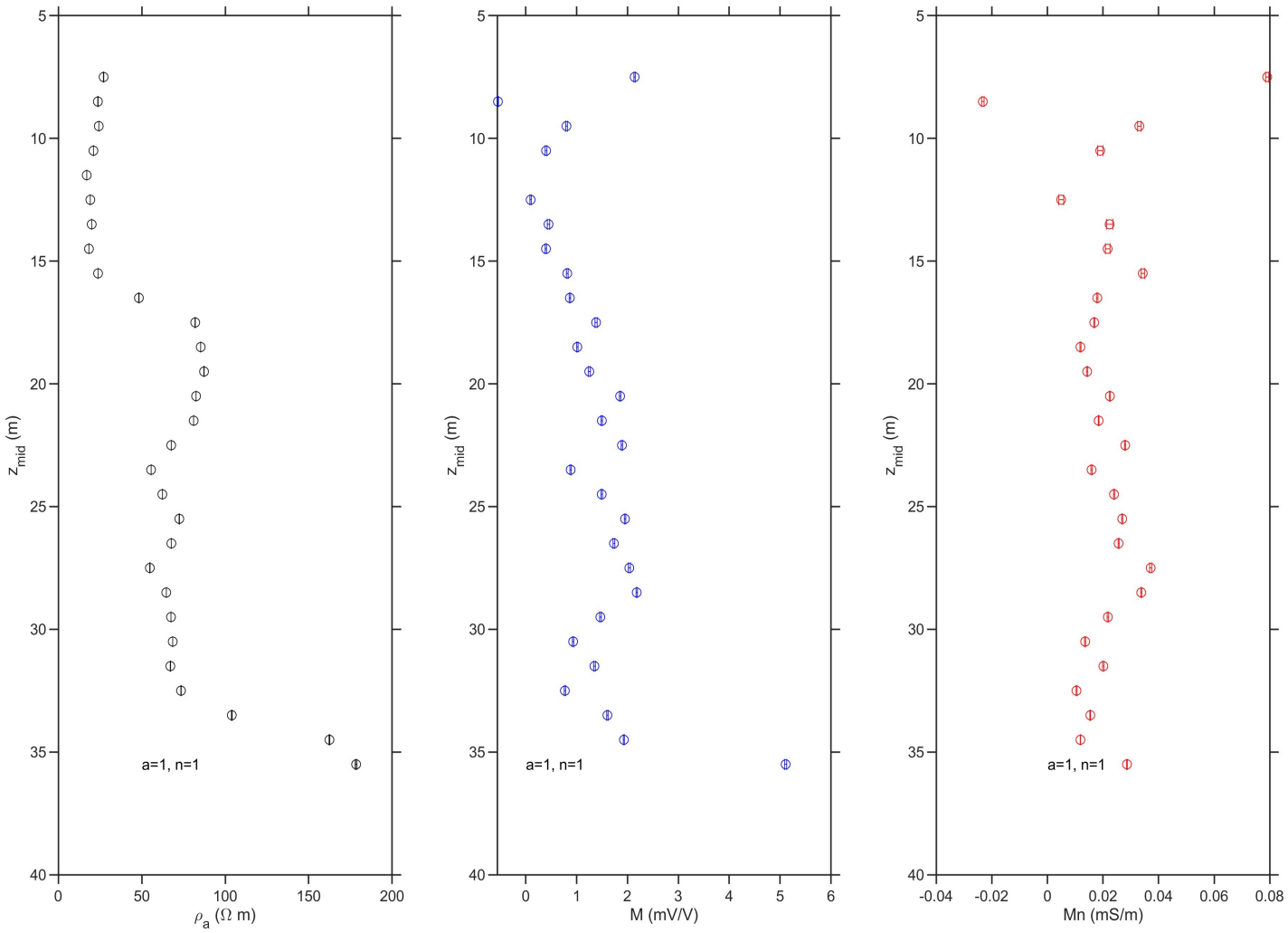

Figure C17. Filtered borehole dipole-dipole apparent resistivity, apparent chargeability, and normalized apparent chargeability logs as a function of mid-point depth for the minimum dipole length (a = 1, n = 1).